

3-14-2014

# Salient Feature Identification and Analysis using Kernel-Based Classification Techniques for Synthetic Aperture Radar Automatic Target Recognition

Matthew S. Flynn

Follow this and additional works at: <https://scholar.afit.edu/etd>

---

## Recommended Citation

Flynn, Matthew S., "Salient Feature Identification and Analysis using Kernel-Based Classification Techniques for Synthetic Aperture Radar Automatic Target Recognition" (2014). *Theses and Dissertations*. 600.  
<https://scholar.afit.edu/etd/600>

This Thesis is brought to you for free and open access by the Student Graduate Works at AFIT Scholar. It has been accepted for inclusion in Theses and Dissertations by an authorized administrator of AFIT Scholar. For more information, please contact [richard.mansfield@afit.edu](mailto:richard.mansfield@afit.edu).



**SALIENT FEATURE IDENTIFICATION AND ANALYSIS USING  
KERNEL-BASED CLASSIFICATION TECHNIQUES FOR SYNTHETIC  
APERTURE RADAR AUTOMATIC TARGET RECOGNITION**

**THESIS**

Matthew S. Flynn, Captain, USAF

AFIT-ENG-14-M-30

**DEPARTMENT OF THE AIR FORCE  
AIR UNIVERSITY**

***AIR FORCE INSTITUTE OF TECHNOLOGY***

**Wright-Patterson Air Force Base, Ohio**

Distribution Statement A: Approved for Public Release; Distribution Unlimited

The views expressed in this thesis are those of the author and do not reflect the official policy or position of the United States Air Force, the Department of Defense, or the United States Government.

This material is declared a work of the U.S. Government and is not subject to copyright protection in the United States.

AFIT-ENG-14-M-30

SALIENT FEATURE IDENTIFICATION AND ANALYSIS USING KERNEL-BASED  
CLASSIFICATION TECHNIQUES FOR SYNTHETIC APERTURE RADAR  
AUTOMATIC TARGET RECOGNITION

THESIS

Presented to the Faculty  
Department of Electrical and Computer Engineering  
Graduate School of Engineering and Management  
Air Force Institute of Technology  
Air University  
Air Education and Training Command  
in Partial Fulfillment of the Requirements for the  
Degree of Master of Science in Electrical Engineering

Matthew S. Flynn, B.S.E.E.

Captain, USAF

March 2014

Distribution Statement A: Approved for Public Release; Distribution Unlimited



**Abstract**

An investigation into feature saliency for application to synthetic aperture radar (SAR) automatic target recognition (ATR) is presented. Specifically, research is focused on improving the SAR binary classification performance aspect of ATR, or the ability to accurately determine the class of a SAR target. The key to improving ATR classification performance lies in characterizing the salient target features. Salient features may be loosely defined as the most consistently impactful parts of a SAR target contributing to effective SAR ATR classification. To better understand the notion of salience, an investigation is conducted into the nature of saliency as applied to Air Force Research Lab's (AFRL) civilian vehicle (CV) data domes simulated phase history data set. After separating vehicles into two SAR data classes, sedan and SUV, frequency and polarization features are extracted from SAR data and formed into either 1D high range resolution (HRR) or 2D spectrum parted linked image test (SPLIT) feature vectors. A series of experiments comparing vehicle classes are designed and conducted to focus specifically on the saliency effects of various SAR collection parameters including azimuth angle, aperture size, elevation angle, and bandwidth. The popular kernel-based Bayesian Relevance Vector Machine (RVM) classifier is utilized for sparse identification of relevant vectors contributing most to the creation of a hyperplane decision boundary. Analysis of experimental results ultimately leads to recommendations of the salient feature vectors and SAR collection parameters which provide the most potential impact to improving vehicle classification. Demonstrating the proposed saliency characterization algorithm with simulated civilian vehicle data provides a road map for salient feature identification and analysis of other SAR data classes in future operational scenarios. ATR practitioners may use saliency results to focus more attention on the identified salient features of a target class, improving efficiency and effectiveness of SAR ATR.

*To my beautiful and supportive wife, thank you for taking this journey with me and always  
being there for me, especially during the stressful times.  
And to my parents, thank you for instilling in me the values and work-ethic that has made  
me the person I am today.*

## **Acknowledgments**

I would first like to thank my advisor, Dr. Julie Jackson, without whom this thesis would not have been possible. Her guidance and expertise throughout this long and arduous research process provided substantial benefits to the outcome of this project.

I would also like to thank Dr. Sean Gilmore, Signal Innovations Group, Inc., and Air Force Research Labs for their valuable advice and support of this thesis project.

This thesis research was sponsored by the Air Force Office of Scientific Research under lab task LRIR12RY19COR.

Matthew S. Flynn



## Table of Contents

	Page
Abstract . . . . .	iv
Dedication . . . . .	v
Acknowledgments . . . . .	vi
Table of Contents . . . . .	vii
List of Figures . . . . .	ix
List of Tables . . . . .	xiii
List of Acronyms . . . . .	xiv
I. Introduction . . . . .	1
1.1 SAR ATR Problem Overview . . . . .	1
1.2 Introduction to Salient Feature Analysis . . . . .	2
1.3 Thesis Goals . . . . .	6
1.4 Thesis Organization . . . . .	8
II. Background . . . . .	9
2.1 Feature Extraction . . . . .	9
2.2 Feature Classification . . . . .	11
2.2.1 Support Vector Machine (SVM) . . . . .	12
2.2.2 Relevance Vector Machine (RVM) . . . . .	16
2.3 Related Research . . . . .	17
2.3.1 SAR Backprojection . . . . .	17
2.3.2 Spectrum Parted Linked Image Test (SPLIT) Algorithm . . . . .	19
III. Methodology . . . . .	29
3.1 Salient Feature Identification Algorithm . . . . .	30
3.2 Salient Feature Experiments . . . . .	38

	Page
IV. Results and Analysis . . . . .	46
4.1 Salient Feature Experiments for HRR FVs . . . . .	46
4.1.1 Azimuth Angle Saliency Experiments for HRR FVs . . . . .	46
4.1.2 Aperture Size Saliency Experiments for HRR FVs . . . . .	59
4.1.3 Elevation Angle Saliency Experiments for HRR FVs . . . . .	71
4.1.4 Bandwidth Saliency Experiments for HRR FVs . . . . .	83
4.2 Salient Feature Experiments for SPLIT FVs . . . . .	96
4.2.1 Azimuth Angle Saliency Experiments for SPLIT FVs . . . . .	97
4.2.2 Aperture Size Saliency Experiments for SPLIT FVs . . . . .	106
4.2.3 Elevation Angle Saliency Experiments for SPLIT FVs . . . . .	112
4.2.4 Bandwidth Saliency Experiments for SPLIT FVs . . . . .	119
4.3 Salient Feature Representation . . . . .	125
V. Recommendations . . . . .	129
5.1 Azimuth Angle Recommendation . . . . .	129
5.2 Aperture Size Recommendation . . . . .	130
5.3 Elevation Angle Recommendation . . . . .	131
5.4 Bandwidth Recommendation . . . . .	131
5.5 Feature Vector Recommendation . . . . .	132
VI. Conclusions and Future Work . . . . .	133
6.1 Conclusions . . . . .	133
6.2 Future Work . . . . .	133
Bibliography . . . . .	135

## List of Figures

Figure	Page
1.1 AFRL CV data domes vehicles . . . . .	7
2.1 SPLIT feature space classification boundaries . . . . .	22
2.2 Traditional backprojection image of Nissan Maxima . . . . .	23
2.3 SPLIT image output for Nissan Maxima . . . . .	25
2.4 Traditional backprojection image of Toyota Tacoma . . . . .	26
2.5 SPLIT image output for Toyota Tacoma . . . . .	27
2.6 SPLIT canonical shape histogram for Nissan Maxima . . . . .	28
2.7 SPLIT canonical shape histogram for Toyota Tacoma . . . . .	28
3.1 Canonical shape target scene image . . . . .	32
3.2 HRR profiles for canonical shape target scene . . . . .	33
3.3 Extracted frequency response for canonical shape target scene . . . . .	34
3.4 Extracted Krogager polarization response for canonical shape target scene . . . . .	35
3.5 RVM classifier HRR feature vector weights example . . . . .	38
3.6 RVM feature space for sedan test example . . . . .	39
3.7 RVM feature space for SUV test example . . . . .	40
3.8 Azimuth angle, aperture size, and elevation angle parameter definitions . . . . .	41
4.1 Total extracted HRR FVs for azimuth angle experiments . . . . .	48
4.2 Total identified relevant HRR FVs for azimuth angle experiments . . . . .	49
4.3 Percent of relevant HRR FVs for azimuth angle experiments . . . . .	50
4.4 Probability of HRR FV error for azimuth angle experiments . . . . .	52
4.5 Azimuth angle HRR FV canonical shape histograms (Az 90°) . . . . .	55
4.6 Azimuth angle HRR FV canonical shape histograms (Az 180°) . . . . .	56
4.7 Azimuth angle HRR FV canonical shape histograms (Az 112.5°) . . . . .	57

Figure	Page
4.8 Azimuth angle HRR FV canonical shape histograms (Az 157.5°) . . . . .	58
4.9 Total extracted HRR FVs for aperture size experiments (Az 180°) . . . . .	60
4.10 Total identified relevant HRR FVs for aperture size experiments (Az 180°) . . . .	61
4.11 Percent of relevant HRR FVs for aperture size experiments (Az 180°) . . . . .	62
4.12 Probability of HRR FV error for aperture size experiments (Az 180°) . . . . .	63
4.13 Aperture size HRR FV canonical shape histograms (Ap size 3°, Az 180°) . . . .	65
4.14 Aperture size HRR FV canonical shape histograms (Ap size 10°, Az 180°) . . . .	66
4.15 Total extracted HRR FVs for aperture size experiments (Az 90°) . . . . .	67
4.16 Total identified relevant HRR FVs for aperture size experiments (Az 90°) . . . .	67
4.17 Percent of relevant HRR FVs for aperture size experiments (Az 90°) . . . . .	68
4.18 Probability of HRR FV error for aperture size experiments (Az 90°) . . . . .	68
4.19 Aperture size HRR FV canonical shape histograms (Ap size 3°, Az 90°) . . . .	69
4.20 Aperture size HRR FV canonical shape histograms (Ap size 10°, Az 90°) . . . .	70
4.21 Total extracted HRR FVs for elevation angle experiments (Az 180°) . . . . .	72
4.22 Total identified relevant HRR FVs for elevation angle experiments (Az 180°) . .	73
4.23 Percent of relevant HRR FVs for elevation angle experiments (Az 180°) . . . .	74
4.24 Probability of HRR FV error for elevation angle experiments (Az 180°) . . . .	75
4.25 Elevation angle HRR FV canonical shape histograms (El 30°, Az 180°) . . . .	77
4.26 Elevation angle HRR FV canonical shape histograms (El 50°, Az 180°) . . . .	78
4.27 Total extracted HRR FVs for elevation angle experiments (Az 90°) . . . . .	79
4.28 Total identified relevant HRR FVs for elevation angle experiments (Az 90°) . .	79
4.29 Percent of relevant HRR FVs for elevation angle experiments (Az 90°) . . . . .	80
4.30 Probability of HRR FV error for elevation angle experiments (Az 90°) . . . . .	80
4.31 Elevation angle HRR FV canonical shape histograms (El 30°, Az 90°) . . . . .	81
4.32 Elevation angle HRR FV canonical shape histograms (El 50°, Az 90°) . . . . .	82

Figure	Page
4.33 Total extracted HRR FVs for bandwidth experiments (Az 180°) . . . . .	84
4.34 Total identified relevant HRR FVs for bandwidth experiments (Az 180°) . . . . .	85
4.35 Percent of relevant HRR FVs for bandwidth experiments (Az 180°) . . . . .	86
4.36 Probability of HRR FV error for bandwidth experiments (Az 180°) . . . . .	87
4.37 Bandwidth HRR FV canonical shape histograms (BW 640 MHz, Az 180°) . . . . .	90
4.38 Bandwidth HRR FV canonical shape histograms (BW 3 GHz, Az 180°) . . . . .	91
4.39 Total extracted HRR FVs for bandwidth experiments (Az 90°) . . . . .	92
4.40 Total identified relevant HRR FVs for bandwidth experiments (Az 90°) . . . . .	92
4.41 Percent of relevant HRR FVs for bandwidth experiments (Az 90°) . . . . .	93
4.42 Probability of HRR FV error for bandwidth experiments (Az 90°) . . . . .	93
4.43 Bandwidth HRR FV canonical shape histograms (BW 640 MHz, Az 90°) . . . . .	94
4.44 Bandwidth HRR FV canonical shape histograms (BW 3 GHz, Az 90°) . . . . .	95
4.45 Total extracted SPLIT FVs for azimuth angle experiments . . . . .	99
4.46 Total identified relevant SPLIT FVs for azimuth angle experiments . . . . .	100
4.47 Percent of relevant SPLIT FVs for azimuth angle experiments . . . . .	101
4.48 Probability of SPLIT FV error for azimuth angle experiments . . . . .	102
4.49 Azimuth angle SPLIT FV canonical shape histograms (Az 90°) . . . . .	103
4.50 Azimuth angle SPLIT FV canonical shape histograms (Az 135°) . . . . .	104
4.51 Azimuth angle SPLIT FV canonical shape histograms (Az 180°) . . . . .	105
4.52 Total extracted SPLIT FVs for aperture size experiments (Az 90°) . . . . .	107
4.53 Total identified relevant SPLIT FVs for aperture size experiments (Az 90°) . . . . .	108
4.54 Percent of relevant SPLIT FVs for aperture size experiments (Az 90°) . . . . .	109
4.55 Probability of SPLIT FV error for aperture size experiments (Az 90°) . . . . .	109
4.56 Aperture size SPLIT FV canonical shape histograms (Ap size 60°, Az 90°) . . . . .	110
4.57 Aperture size SPLIT FV canonical shape histograms (Ap size 120°, Az 90°) . . . . .	111

Figure	Page
4.58 Total extracted SPLIT FVs for elevation angle experiments (Az 180°) . . . . .	113
4.59 Total identified relevant SPLIT FVs for elevation angle experiments (Az 180°) .	114
4.60 Percent of relevant SPLIT FVs for elevation angle experiments (Az 180°) . . .	115
4.61 Probability of SPLIT FV error for elevation angle experiments (Az 180°) . . . .	116
4.62 Elevation angle SPLIT FV canonical shape histograms (El 30°, Az 180°) . . . .	117
4.63 Elevation angle SPLIT FV canonical shape histograms (El 50°, Az 180°) . . . .	118
4.64 Total extracted SPLIT FVs for bandwidth experiments (Az 135°) . . . . .	120
4.65 Total identified relevant SPLIT FVs for bandwidth experiments (Az 135°) . . .	121
4.66 Percent of relevant SPLIT FVs for bandwidth experiments (Az 135°) . . . . .	122
4.67 Probability of SPLIT FV error for bandwidth experiments (Az 135°) . . . . .	122
4.68 Bandwidth SPLIT FV canonical shape histograms (BW 640 MHz, Az 135°) . .	123
4.69 Bandwidth SPLIT FV canonical shape histograms (BW 3 GHz, Az 135°) . . .	124
4.70 HRR FV location representation . . . . .	126
4.71 SPLIT FV location representation . . . . .	127

## List of Tables

Table	Page
1.1 AFRL CV data domes vehicles . . . . .	6
2.1 SPLIT frequency response for canonical shapes . . . . .	20
3.1 Canonical shape target scene parameters . . . . .	31
3.2 AFRL CV data domes RVM classification example results . . . . .	37
3.3 Training and testing data sets for all 24 experiments . . . . .	43
3.4 SAR collection parameters for HRR FV experiments . . . . .	44
3.5 SAR collection parameters for SPLIT FV experiments . . . . .	44
4.1 Azimuth angle experiment results for HRR FVs . . . . .	47
4.2 Aperture size experiment results for HRR feature vectors (Az 180°) . . . . .	59
4.3 Aperture size experiment results for HRR feature vectors (Az 90°) . . . . .	63
4.4 Elevation angle experiment results for HRR feature vectors (Az 180°) . . . . .	71
4.5 Elevation angle experiment results for HRR feature vectors (Az 90°) . . . . .	75
4.6 Bandwidth experiment results for HRR feature vectors (Az 180°) . . . . .	83
4.7 Bandwidth experiment results for HRR feature vectors (Az 90°) . . . . .	88
4.8 Azimuth angle experiment results for SPLIT feature vectors . . . . .	98
4.9 Aperture size experiment results for SPLIT feature vectors (Az 90°) . . . . .	106
4.10 Elevation angle experiment results for SPLIT feature vectors (Az 180°) . . . . .	112
4.11 Bandwidth experiment results for SPLIT feature vectors (Az 135°) . . . . .	119
5.1 Summary of Parameter Recommendations . . . . .	130

## List of Acronyms

Acronym	Definition
AFRL	Air Force Research Laboratory
ATR	automatic target recognition
AFW	average feature weight
BW	bandwidth
CV	civilian vehicle
FV	feature vector
HRR	high range resolution
KNN	$K^{th}$ Nearest Neighbor
LSS	Least Squares Solution
MFW	max feature weight
PCA	Principal Component Analysis
QP	quadratic programming
RBF	Radial Basis Function
RVM	Relevance Vector Machine
RV	relevant vector
SDMS	Sensor Data Management System
SPLIT	Spectrum Parted Linked Image Test
SVM	Support Vector Machine
SAR	synthetic aperture radar



SALIENT FEATURE IDENTIFICATION AND ANALYSIS USING KERNEL-BASED  
CLASSIFICATION TECHNIQUES FOR SYNTHETIC APERTURE RADAR  
AUTOMATIC TARGET RECOGNITION

**I. Introduction**

**1.1 SAR ATR Problem Overview**

Advances in optical technology have made it possible to acquire high-quality images of targets-of-interest from ranges beyond the earth's atmosphere [1]. The drawback to these optical advances is that both clear visibility and an adequate light source are required to collect recognizable image data. The answer to these drawbacks is synthetic aperture radar (SAR) imaging [2]. Electromagnetic waves transmitted by airborne radar are able to propagate to and from a target-of-interest regardless of the weather conditions or time of day, providing information about a target that is otherwise not achievable with an optical lens. Using the scattering responses, or phase history data, collected from the target, SAR images may be formed and analyzed for target identification. The quality of the SAR image depends on the amount of information collected from the target, both in angular extent and frequency content. SAR images will be more complete if phase history data encompasses a wide bandwidth and is collected from many aspect angles of the target, both in azimuth and elevation of the airborne radar in relation to the ground target. The azimuth coverage of the radar's flight path corresponds to the synthetic aperture of the radar, and the greater the aperture, the easier it will be to construct a recognizable image from phase history data. Limitations often cause phase history data to be collected sparsely in aperture, bandwidth, or both, however, making it difficult to construct a recognizable image from the incomplete phase histories.

Once phase history data for a specific target area is collected, SAR imaging algorithms such as backprojection or polar reformat are used to generate the SAR image [2, 3]. Analysts are trained to recognize specific targets-of-interest from sparse or incomplete SAR images for specific tasks such as international intelligence. This method of SAR image analysis is time consuming and subject to potential human error. To assist analysts in the understanding of incomplete SAR target information, advances in automatic target recognition (ATR) research have provided additional information regarding the physical characteristics of SAR targets through a variety of preprocessing and feature extraction and classification techniques on phase history data. This research continues the efforts toward the advancement of SAR ATR through an exploration and analysis of salient target features.

## **1.2 Introduction to Salient Feature Analysis**

Many advances in SAR ATR related fields have involved extracting particular features from the phase history data to reduce dimensionality of the data in order to classify specific portions of the target. Some techniques have involved extracting wavefronts [4] or point scatterers [5] from phase history data, while other methods extract features which represent 3D physically relevant canonical shapes [6, 7]. Three-dimensional parametric scattering centers are designed specifically to break down a target into its physical features for ease of identification and analysis.

One particular feature analysis technique, the SPLIT algorithm [8, 9], proposed by Fuller and discussed in Section 2.3.2, attempts to correctly classify canonical shapes within a SAR target image to aid in target analysis and identification. Regardless of the type of features which are classified, however, a common thread among feature analysis techniques is that in order to correctly classify a target or parts of a target, distinguishing features must be extracted from phase history data to reduce target ambiguity for identification.

The features to be extracted from phase history data for saliency research include frequency and polarization information corresponding to physical locations on the target.

Each set of extracted features at a specified location are concatenated into a feature vector (FV). Two types of FVs are considered for salient feature analysis. The first are extracted 1D high range resolution (HRR) profiles corresponding to azimuth angle and range. The HRR FVs utilized for saliency research are expressed as  $(\alpha, k_e, k_o, \phi, r)$ , where  $\alpha$  is the frequency parameter,  $k_e$  is the even-bounce polarization information,  $k_o$  is the odd-bounce polarization information,  $\phi$  is the azimuth angle with respect to the target, and  $r$  is the range with respect to the target scene center. Two-dimensional image FVs are also utilized for saliency analysis through implementation of the SPLIT algorithm. The 2D SPLIT FVs may be expressed as  $(\alpha, k_e, k_o, x, y)$ , where  $x$  and  $y$  correspond to the pixel locations within a 2D SAR image obtained through the backprojection imaging algorithm. Further details on the feature extraction process for saliency analysis as well as background information on the backprojection and SPLIT algorithms are provided in Chapter 2.

Each extracted FV maps to a specific location on the target, and the extracted frequency and polarization features provide additional information for distinguishing between data points. Identification decisions from an ATR perspective may then be made using classification techniques on the extracted FVs. Feature classification is widely used in the fields of pattern recognition and machine learning for a range of research including such topics as medical imaging [10] and handwriting recognition [11]. The type of feature classification used for SAR saliency analysis is an extension of the popular Support Vector Machine (SVM) [12] called the Relevance Vector Machine (RVM), originally developed by Tipping [13]. While the details of the RVM feature classification method are covered in more detail in Chapter 2, RVM is a supervised learning method that is kernel-driven to separate classes of data in high-dimensional feature spaces and sparsely identify those FVs which aid most in the creation of the decision boundary. Unlike other ATR classification algorithms, using the kernel-based Bayesian RVM classifier eliminates irrelevant feature data to reveal only the most impactful features among data classes.

Analysis of the identified relevant vectors will provide additional information about the most consistently significant features for each target which will allow SAR image analysts and ATR practitioners to focus more attention on the salient features of a particular target class.

The term “salient” was specifically chosen to describe our research objectives for several reasons. Saliency is not merely another term for “relevance” describing the outputs of the RVM feature classification method. Feature saliency carries a deeper meaning than adjectives such as important or relevant because an identified relevant feature in one example may be considered irrelevant in a similar example with slightly different parameter values. A salient feature must demonstrate a pattern of persistence through many experiments, making it difficult to define within research since not all salient features are identified in the same way. Others have defined saliency in the context of their own research based upon the methods chosen for identifying salient features [14]. We will incorporate several output metrics and analysis methods to best characterize the salient feature identification process discussed in Chapter 3. A formal definition of saliency will not be explicitly expressed prior to the start of our research. Instead, an investigation will be conducted into the nature of saliency by analyzing a variety of parameter effects and FVs on feature classification outputs. Observed patterns and results will ultimately contribute to recommendations regarding saliency within the context of our research. The identified salient features for the SAR civilian vehicle targets analyzed here may not translate to other target classes, but the methodology developed for characterizing saliency may be applied to future work so that salient features may be highlighted on any class of targets for improvement of ATR.

Two types of target sets are considered for salient feature analysis research. The first is target scenes consisting of only the 3D canonical shapes. Phase histories of synthetic radar scattering data are generated for scenes comprised of canonical scatterers at specified

parameters which include  $x$ ,  $y$ , and  $z$  location parameters, height  $H$ , length  $L$ , and radius  $r$  size parameters, and roll  $\tilde{\gamma}$ , pitch  $\tilde{\theta}$ , and yaw  $\tilde{\phi}$  orientation parameters. The azimuth, elevation, and aperture size angles corresponding to the radar flight path are specified in addition to radar bandwidth. Once phase history has been generated for a canonical shape scene, frequency and polarization parameters are extracted using the algorithms described in Section 2.1. Beginning saliency analysis research with the canonical scatterers allows for the calibration of the feature extraction algorithms to ensure accurate results. Since there are far fewer scatterers in the primitive scatterer scenes than in complex real-world targets, the features and locations for each scatterer may be more easily predicted to verify accurate extraction results. The second target sets used for saliency analysis are much more complex, and feature extraction and classification results may not be predicted as easily or accurately.

The second type of SAR targets considered for our research effort are civilian vehicles. Air Force Research Laboratory (AFRL)'s publicly available civilian vehicle (CV) data domes consist of fully polarimetric simulated phase history data for ten different models of civilian vehicles over  $0^\circ - 360^\circ$  in azimuth,  $30^\circ - 60^\circ$  in elevation, and a wide 5.35 GHz bandwidth [15]. All ten vehicles are listed in Table 1.1 along with the class of vehicle to which each has been assigned. In addition, all vehicles are illustrated in Figure 1.1. Feature vectors are extracted from the phase history for a single vehicle over a specified azimuth, elevation, aperture extent, and bandwidth for input into the RVM classifier according to the saliency analysis experiments described in Chapter 3. Relevant FVs are analyzed and compared between vehicles and across vehicle classes to determine the most impactful features.

Saliency analysis results may be used to create more efficient and effective target models that focus on the identified salient features of a target class and ignore those features that are irrelevant or redundant across all classes. Additionally, a methodology

Table 1.1: AFRL CV data domes vehicles with corresponding vehicle class assignment.

Vehicle Make and Model	Class
Toyota Camry	Sedan
Honda Civic	Sedan
Jeep Cherokee (1993)	SUV
Jeep Cherokee (1999)	SUV
Nissan Maxima	Sedan
Mazda MPV	SUV
Mitsubishi	Sedan
Nissan Sentra	Sedan
Toyota Avalon	Sedan
Toyota Tacoma	SUV

is developed for distinguishing identifiable features between target classes, leading to a more accurate ATR process. The results of this research effort may directly benefit the Air Force operationally through optimization of flight paths based on known salient features of a particular target-of-interest.

### 1.3 Thesis Goals

While a significant amount of work has been accomplished in the field of SAR ATR, it is a complex problem that is nowhere near solved. We will focus on a piece of this problem, specifically the comparison of two classes of SAR phase history data for improvement of binary classification accuracy and identification of distinguishable class features. Distinctive class features separate one SAR target from another and ultimately lead to accurate target identification. Analysis will follow distinctive feature patterns for

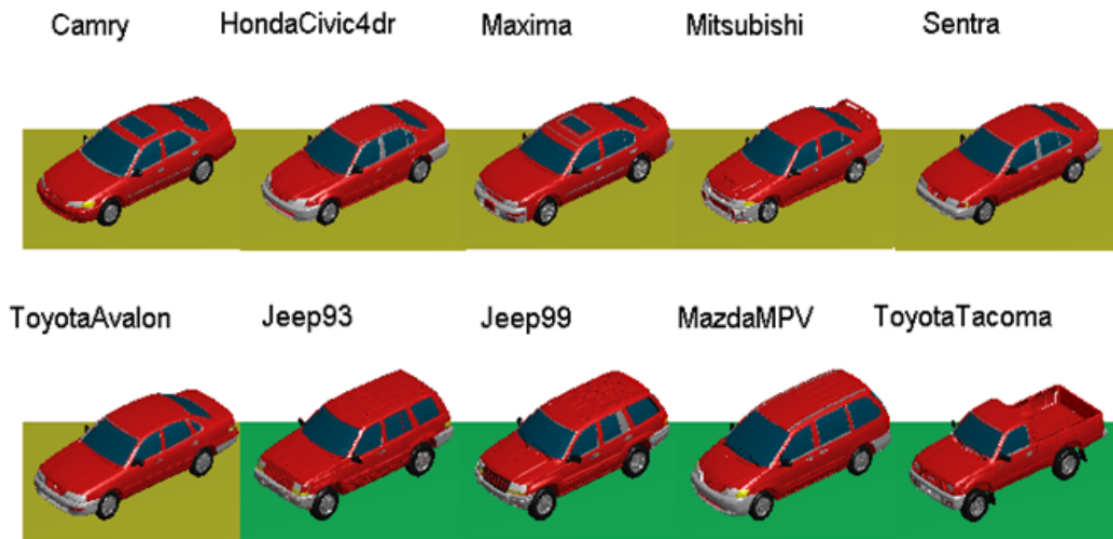


Figure 1.1: All AFRL CV data domes vehicles separated into sedan class, shown with yellow background, and SUV class, shown with green background [15].

an investigation into the nature of saliency. The contributions and goals of our saliency research are as follows.

1. Investigate the nature of saliency by developing a methodology for improving the SAR binary classification performance aspect of ATR.
2. Demonstrate the saliency characterization process by conducting experiments to fully investigate the AFRL CV data domes SAR phase history data set separated into sedan and SUV classes.
3. Provide recommendations of the most effective SAR collection parameter values for improving binary classification performance of civilian vehicles by investigating the saliency effects of azimuth angle, aperture size, elevation angle, and bandwidth.

4. Provide recommendations of the most effective type of extracted feature vector for improving binary classification performance of civilian vehicles by investigating the saliency effects of 1D HRR feature vectors and 2D SPLIT feature vectors.

#### **1.4 Thesis Organization**

This thesis is organized in the following manner. Chapter 2 provides a background of the topics and algorithms which support our saliency research. Fields include feature extraction techniques such as the Krogager polarization decomposition [16] and feature classification algorithms such as the SVM and RVM. Additional related research which applies to the saliency investigation is also presented in Chapter 2. In Chapter 3, a methodology is developed for determining the salient features of a particular target class. In addition, an outline of feature saliency experiments is presented to compare sedan and SUV civilian vehicle target classes over azimuth, elevation, aperture extent, and bandwidth. Chapter 4 details the results and analysis of the saliency experiments which reveal the most impactful features and SAR collection parameters for effective target class identification between sedan and SUV civilian vehicles. A summary of the overall recommendations for the parameters and FVs tested with regards to ATR applicability is presented in Chapter 5. Finally, Chapter 6 provides final conclusions and potential future work in the fields of salient feature analysis and SAR ATR classification.



## II. Background

Prior to exploring salient feature analysis, background information must be discussed for topics used extensively throughout saliency research. Two primary research fields include feature extraction and feature classification, with an emphasis on the popular kernel-based vector machine methods of classification. Feature extraction theory will include frequency and polarization decomposition methods, presented from [16–18], while foundational material presented for feature classification, SVM, and RVM can be found in [12, 13, 19–21].

### 2.1 Feature Extraction

The basic goal of feature extraction is to reduce the ambiguity of a data set by drawing distinctive information from the data so that the resulting set is more easily separable into identifiable classes. If successful, feature extraction may provide useful information about the data not otherwise known from the original data set. Feature extraction techniques are especially useful for extremely large real-world SAR phase history data collections because they may be used to provide valuable information about unknown targets. Some of the features that may be extracted from SAR data include frequency parameters, polarization parameters, and location parameters which include range and angle to the target for 1D HRR profiles and  $x$  and  $y$  pixel coordinates for 2D SAR imagery.

Within the context of HRR feature vector extraction, the frequency parameter  $\alpha$  is extracted from phase history data using an approach known as the Matrix Pencil Method [17, 18]. This parameterization method provides several benefits which include a low sensitivity to noise and a decreased computational complexity by avoiding a multi-dimensional optimization process [6, 22]. For SPLIT feature vectors, the frequency

parameter is extracted using an iterative curve fitting algorithm which is further described in Section 2.3.2.

Frequency parameters alone may not provide enough information to resolve and classify targets for salient feature identification. To further reduce target ambiguity within the ATR process, polarization features are extracted using the Krogager basis decomposition [16] for both HRR and SPLIT feature vectors. The Krogager decomposition method extracts fully-polarmetric target information corresponding to even, odd, and helical bounce features from the SAR data. The  $2 \times 2$  complex radar data scattering matrix, or Sinclair matrix, may be represented as

$$S = \begin{bmatrix} S_{hh} & S_{vh} \\ S_{hv} & S_{vv} \end{bmatrix},$$

where  $S$  is broken down into its horizontal and vertical transmit and receive orientations with  $S_{hv} = S_{vh}$  for mono-static radar. The fully-polarmetric data may then be translated to circular polarizations [23]

$$S_{rr} = jS_{hv} + \frac{1}{2}(S_{hh} - S_{vv}), \quad (2.1)$$

$$S_{ll} = jS_{hv} - \frac{1}{2}(S_{hh} - S_{vv}), \quad (2.2)$$

$$S_{rl} = \frac{1}{2}(S_{hh} + S_{vv}). \quad (2.3)$$

It follows that the polarization target features may be extracted for each feature vector using the Krogager decomposition as [23]

$$K_e = \min(|S_{ll}|, |S_{rr}|), \quad (2.4)$$

$$K_o = |S_{rl}|, \quad (2.5)$$

$$K_h = \text{abs}(|S_{rr}| - |S_{ll}|), \quad (2.6)$$

where  $K_e$  represents the even bounce scattering component,  $K_o$  the odd, and  $K_h$  the helical received radar scattering component. The final normalized Krogager decomposition

coefficients may then be expressed by [23] as

$$\kappa_o = \frac{K_o}{\sqrt{|K_o|^2 + |K_e|^2 + |K_h|^2}}, \quad (2.7)$$

$$\kappa_e = \frac{K_e}{\sqrt{|K_o|^2 + |K_e|^2 + |K_h|^2}}, \quad (2.8)$$

$$\kappa_h = \frac{K_h}{\sqrt{|K_o|^2 + |K_e|^2 + |K_h|^2}}. \quad (2.9)$$

By implementing the Krogager decomposition process outlined above, the original  $2 \times 2$  scattering matrix is transformed into three polarization feature coefficient components which provide further insight into the physical features of the desired target.

An HRR feature vector is formed for every returned radar pulse by concatenating the extracted frequency and polarization features with each corresponding azimuth and range bin expressed as  $(\alpha, k_e, k_o, \phi, r)$ . Similarly, 2D image feature vectors are created through the SPLIT algorithm using the extracted frequency and polarization features with the  $x$  and  $y$  pixel coordinates within a 2D SAR image, expressed as  $(\alpha, k_e, k_o, x, y)$ . Forming these 1D and 2D image feature vectors through feature extraction techniques accomplishes the first major step in saliency analysis and leads to the feature classification step of the ATR process.

## 2.2 Feature Classification

Classification is a common practice used in the statistical machine learning and pattern recognition communities. Many classification algorithms, including those used in our saliency research, utilize a binary classification process in which test data is input into the desired classifier to determine which of the two training classes each input test data sample belongs. Feature classification is a form of supervised learning, meaning the algorithm is first trained to establish a decision rule before test data is applied. There are many traditional classifier algorithms such as Least Squares Solution (LSS) [24],  $K^{th}$  Nearest Neighbor (KNN) [25], and Principal Component Analysis (PCA) [26].

While traditional classifiers each provide their own advantages, our saliency research utilizes kernel-driven classification, specifically the RVM, based on the adaptability and compressibility advantages described in Section 2.2.1 and Section 2.2.2.

### ***2.2.1 Support Vector Machine (SVM).***

SVM is a kernel-based, supervised learning classifier introduced by Vapnik and coworkers [12]. SVM is a classification algorithm able to create a decision boundary on large complex data sets efficiently, making it an appealing choice for research involving computationally complex SAR phase history data. Two distinct sets of SAR data may often contain a significant amount of overlapping data points, making it challenging to determine a clear decision boundary. The non-linear SVM classifier operates by transforming the two data sets to high-dimensional feature spaces through the use of an appropriate choice of kernel function, increasing separation between the training data in feature space so that a hyperplane decision boundary may be created. The increased separation among training data allows test data samples to be classified more accurately in the transformed feature space. The compressibility of SVM stems from its ability to assign weights to data samples such that a small fraction of the original data is able to effectively describe the entire data set, while the remainder of the original data points are deemed irrelevant and assigned zero weight. The weights are assigned in the feature space via the chosen kernel with the ultimate goal of maximizing the classification margin, or the distance from the hyperplane decision boundary to the nearest training data points on either side [19]. The data points which contribute most to maximizing the decision boundary margin are assigned the highest weights and identified as the support vectors.

It is the support vectors, or the more sparse relevant vectors as discussed in Section 2.2.2, that are deemed most impactful to the classification process and are therefore analyzed as potential salient features. Once identified, the salient features may then be used

to highlight the most consistently significant portions of a SAR target for more effective modeling, simulation, and ultimately identification.

Consider training data points  $\mathbf{x} = [x_1, x_2, \dots, x_L]$ , each belonging to one of two classes of data,  $y_i = -1$  or  $+1$ . As Fletcher describes in [27], a general hyperplane may be defined as [12, 27]

$$\mathbf{w} \cdot \mathbf{x} + b = 0, \quad (2.10)$$

where  $\mathbf{w}$  is a vector normal to the optimal hyperplane, and  $\frac{b}{\|\mathbf{w}\|}$  is the perpendicular distance from the hyperplane to the origin. Some binary classification problems, such as those investigated in our SAR saliency research, do not have linearly separable classes. These types of nonlinear classification problems require the use of the kernel trick [19] to transform class data to higher dimensional feature spaces,  $\mathbf{x} \Rightarrow \phi(\mathbf{x})$ , for separation. For any two training data points  $x_i$  and  $x_j$ , the kernel function  $K$  must satisfy the inner product condition  $K(x_i, x_j) = \langle \phi(x_i), \phi(x_j) \rangle$ , but the specific kernel function implemented may transform training data into the feature space  $\mathbf{x} \Rightarrow \phi(\mathbf{x})$  without ever calculating the feature space  $\phi$  directly. Since many data sets demonstrate a normal distribution, the most commonly used kernel for SVM is the Gaussian Radial Basis Function (RBF) [14, 28]

$$K(x_i, x_j) = \exp\left(-\frac{\|x_i - x_j\|^2}{\sigma^2}\right), \quad (2.11)$$

where  $\sigma$  is the sensitivity parameter of the kernel. In order to determine the optimal hyperplane decision boundary required to implement the SVM,  $\mathbf{w}$  and  $b$  must be found to satisfy the conditions on each of the two classes [12, 27]

$$\phi(\mathbf{x}_i) \cdot \mathbf{w} + b \geq +1 \quad \text{for } y_i = +1, \quad (2.12)$$

$$\phi(\mathbf{x}_i) \cdot \mathbf{w} + b \leq -1 \quad \text{for } y_i = -1, \quad (2.13)$$

where  $\phi(\mathbf{x}_i)$  represents the training points in transformed feature space via the RBF kernel in Equation (2.11). Support vectors are defined as those training points which lie closest to

the decision hyperplane in the kernel transformed feature space. Consider that the support vectors lie on two additional hyperplanes  $D_1$  and  $D_2$  which correspond to distances  $d_1$  and  $d_2$ , respectively, from the decision hyperplane. The goal of the SVM is to design the optimal hyperplane such that the distances  $d_1$  and  $d_2$  to the nearest support vectors is maximized, which will occur when  $M = d_1 = d_2$ , where  $M$  is known as the SVM's margin. The margin may be calculated as  $M = \frac{1}{\|\mathbf{w}\|}$ , and maximizing  $M$  with the constraints in Equation (2.12) and Equation (2.13) is equivalent to minimizing  $\|\mathbf{w}\|$  as [12, 27]

$$\min \|\mathbf{w}\| \quad \text{subject to } y_i(\phi(\mathbf{x}_i) \cdot \mathbf{w} + b) - 1 \geq 0 \quad \forall_i. \quad (2.14)$$

Optimizing Equation (2.14) requires the introduction of Lagrange multipliers in the form of feature vector weights  $\gamma_i$  [12, 27],

$$L_P = \frac{1}{2} \|\mathbf{w}\|^2 - \sum_{i=1}^L \gamma_i y_i (\phi(\mathbf{x}_i) \cdot \mathbf{w} + b) + \sum_{i=1}^L \gamma_i, \quad (2.15)$$

where  $\gamma_i \geq 0 \quad \forall_i$  and  $L_P$  is the primary Lagrangian form. The objective is to minimize Equation (2.15) with respect to  $\mathbf{w}$  and  $b$  and maximize it with respect to  $\gamma$ . To accomplish this task, we first differentiate  $L_P$  with respect to  $\mathbf{w}$  and  $b$  and set the resultant derivatives to zero [12, 27]

$$\frac{\delta L_P}{\delta \mathbf{w}} = \mathbf{w} - \sum_{i=1}^L \gamma_i y_i \phi(\mathbf{x}_i) = 0, \quad (2.16)$$

$$\frac{\delta L_P}{\delta b} = \sum_{i=1}^L \gamma_i y_i = 0. \quad (2.17)$$

Now substituting Equation (2.16) and Equation (2.17) into Equation (2.15), we get the dual form of  $L_P$  [12, 27]

$$L_D = \sum_{i=1}^L \gamma_i - \frac{1}{2} \sum_{i,j} \gamma_i \gamma_j y_i y_j \phi(\mathbf{x}_i) \phi(\mathbf{x}_j) \quad \text{subject to } \gamma_i \geq 0 \quad \forall_i, \quad \sum_{i=1}^L \gamma_i y_i = 0. \quad (2.18)$$

The Lagrangian dual objective function  $L_D$  is particularly important for non-linear binary classification, as it requires only the dot product of each training vector  $\mathbf{x}_i$  for transformation

to the feature space using the kernel trick [19]. Defining an input matrix  $H_{ij} = y_i y_j \phi(\mathbf{x}_i) \cdot \phi(\mathbf{x}_j)$ , the Lagrangian dual objective function simplifies [12, 27]

$$L_D = \sum_{i=1}^L \gamma_i - \frac{1}{2} \boldsymbol{\gamma}^T \mathbf{H} \boldsymbol{\gamma} \quad \text{subject to } \gamma_i \geq 0 \forall_i, \sum_{i=1}^L \gamma_i y_i = 0. \quad (2.19)$$

As  $L_D$  is dependent on  $\boldsymbol{\gamma}$ , it must be maximized [12, 27],

$$\max_{\boldsymbol{\gamma}} \left[ \sum_{i=1}^L \gamma_i - \frac{1}{2} \boldsymbol{\gamma}^T \mathbf{H} \boldsymbol{\gamma} \right] \quad \text{subject to } \gamma_i \geq 0 \forall_i \text{ and } \sum_{i=1}^L \gamma_i y_i = 0. \quad (2.20)$$

Solving for  $\boldsymbol{\gamma}$  in Equation (2.20), a convex quadratic optimization problem, requires the use of a quadratic programming (QP) solver. Once feature weights vector  $\boldsymbol{\gamma}$  is determined, it may be used to find  $\mathbf{w}$  from Equation (2.16). All that remains is determining  $b$  to finalize the creation of our hyperplane decision boundary. We know from the constraint on Equation (2.14) that any support vectors must satisfy [12, 27]

$$y_s(\phi(\mathbf{x}_s) \cdot \mathbf{w} + b) = 1, \quad (2.21)$$

where  $\mathbf{x}_s$  is a support vector and  $y_s$  describes the class to which it belongs. Substituting in Equation (2.16), we see that [12, 27]

$$y_s \left( \sum_{m \in S} \gamma_m y_m \phi(\mathbf{x}_m) \cdot \phi(\mathbf{x}_s) + b \right) = 1, \quad (2.22)$$

where  $S$  is the set of all support vectors, determined by finding all feature weights  $\gamma_i > 0$ . From the class definitions in Equation (2.12) and Equation (2.13), we know that  $y_s^2 = 1$ , so we multiply both sides of Equation (2.22) by  $y_s$  and solve for  $b$  as [12, 27]

$$b = y_s - \sum_{m \in S} \gamma_m y_m \phi(\mathbf{x}_m) \cdot \phi(\mathbf{x}_s). \quad (2.23)$$

Having found the set of support vectors  $\mathbf{x}_s$  where the weights  $\gamma > 0$ , and the two components needed to define the optimal separating hyperplane in feature space,  $\mathbf{w}$  and  $b$ , we have designed a fully functioning SVM classifier. New test data points  $\mathbf{x}'$  may now be classified into their appropriate class  $y'$  as [12, 27]

$$y' = \text{sgn}(\mathbf{w} \cdot \phi(\mathbf{x}') + b). \quad (2.24)$$

Following the process described above, the SVM will create an optimal classification boundary by maximizing the margin between two training data classes based upon the weights given to the most significant data points, or support vectors. While the SVM provides a level of compressibility by seeking to identify only those data points that are most impactful to the decision boundary and ignoring all those with little contribution to the classification process, extremely large training data sets, such as SAR phase history data, may still provide a large number of support vectors. In addition, if the two target classes being trained for classification are very similar, such as two different sedan class civilian vehicles, creating the optimal decision boundary with the SVM may require a large number of support vectors. Incorporating a Bayesian approach to the SVM is a method, discussed further in Section 2.2.2, which aims to achieve a sparse solution while still accurately representing and separating the classification training data.

### 2.2.2 *Relevance Vector Machine (RVM).*

The RVM, introduced by Tipping [13], provides a Bayesian interpretation to the SVM, resulting in creation of the optimal hyperplane decision boundary in kernel space through a sparser set of support vectors referred to as relevant vectors. The RVM follows the same functional form as the SVM process described in Section 2.2.1 but with an imposed sparseness. The sparseness of the RVM classification model is achieved by introducing a bias over the feature weights  $\gamma$  in the form of a prior probability [13, 14, 20]

$$p(\gamma_i|\vartheta_i) = N(0|\vartheta_i), \quad (2.25)$$

where  $\vartheta$  is the variance of each feature weight  $\gamma_i$ , and the Gaussian prior has a zero mean to encourage additional zero-weighted feature vectors forcing sparseness. The sparseness prior is balanced by a posterior probability which aims to create a model which accurately fits the training data  $\mathbf{x}$ . Similar to the SVM, we aim to determine parameters  $\mathbf{w}$  and  $b$  for defining the hyperplane decision boundary and weights  $\gamma_i$  for identification of the set of relevant vectors most impactful to classification decisions. Therefore, the posterior



probability may be represented as [13, 20]

$$p(\gamma_i, \mathbf{w}, b|\mathbf{x}) = p(\gamma_i|\mathbf{x}, \mathbf{w}, b)p(\mathbf{w}, b|\mathbf{x}). \quad (2.26)$$

Implementing these two probability constraints into the framework of the SVM provides a method which aims to accurately represent the training sets with only the most significant feature vectors, or relevant vectors, contributing to decision boundary creation.

The improvement in sparsity of identified relevant vectors which best model the overall training data sets achieved by the RVM makes it an excellent choice for feature saliency analysis. The sparse number of relevant vectors highlighted during the classification process will provide insight into those portions of a target or target class which are most important to SAR target identification. In addition, the probability of error metric output by the RVM will provide a level of confidence in the classification result which also contributes to determining the most salient target features. The feature saliency experiments designed in Chapter 3 are conducted with an RVM classifier. Various SAR collection parameters are adjusted throughout the experiments in hopes of determining those features and collection parameters contributing most to accurate saliency results.

## 2.3 Related Research

### 2.3.1 SAR Backprojection.

Once the RVM classifier identifies the feature vectors most relevant to the classification decision boundary, the relevant feature vectors may be translated to physical target locations to aid in the ATR process. One method that may be used to translate extracted feature vectors into physical target space is SAR imaging. Backprojection is a common type of SAR imaging technique that maps individual projections onto a spatial grid and integrates over the aperture angles to produce an image from phase history data [2]. Backprojection may be used for 1D, 2D, and 3D imaging. In 1D, each transmitted and received radar pulse forms a HRR profile which provides the magnitudes of reflections from the

target scene at all ranges for a specific azimuth and elevation angle. As the radar continues to move over the aperture extent, additional HRR profiles are collected in phase history. The combinations of these HRR projections represent the overall measured reflectivity of the target scene,  $g(s, \phi)$ , and can be expressed using the Radon transform [2]

$$g(s, \phi) = \int_{-\infty}^{\infty} f(s \cos \phi - u \sin \phi, s \sin \phi + u \cos \phi) du, \quad (2.27)$$

$$-\infty < s < \infty, 0 \leq \theta \leq \pi,$$

where  $s$  represents range,  $u$  represents cross-range,  $\phi$  represents azimuth angle, and  $f(s, \phi)$  represents the actual target scene being imaged. Considering that, for 2D SAR imaging,  $g(s, \phi)$  is collected in phase history and the target scene  $f(x, y)$  is desired, the inverse radon transform, or the backprojection operation, is more appropriate for forming a SAR image of the target scene [2]

$$f(x, y) = \int_0^{\pi} \int_{-\infty}^{\infty} (|\xi| G(\xi, \phi) e^{j2\pi\xi(x \cos \phi + y \sin \phi)} d\xi) d\phi, \quad (2.28)$$

where  $\xi$  is spatial frequency and  $G(\xi, \phi)$  is the Fourier transform of the projections  $g(s, \phi)$ . In Equation (2.28), the integral on  $\xi$  filters and convolves each projection, then the integral on  $\phi$  sums the values over all projections to form the image through backprojection. Windowing functions in both frequency and azimuth may also be used to form the 2D image from a desired amount of collected phase history using backprojection [2]

$$f(x, y) = \int_0^{\pi} \int_{-\infty}^{\infty} (|H_{\xi}(\xi - \xi_c)| G(\xi, \phi) e^{j2\pi H_{\xi}(\xi - \xi_c)(x \cos H_{\phi}(\phi - \phi_c) + y \sin H_{\phi}(\phi - \phi_c))} d\xi) d\phi, \quad (2.29)$$

where  $H_{\xi}(\xi - \xi_c)$  is the band-limited window in frequency with center frequency  $\xi_c$  and  $H_{\phi}(\phi - \phi_c)$  is the aperture-limited window in azimuth with center azimuth  $\phi_c$ .

Given ample bandwidth in frequency, aperture extent in azimuth, and sufficient sampling to avoid the effects of aliasing [2, 3], backprojection is an effective SAR imaging technique capable of forming recognizable images of SAR targets. If a target scene is comprised of many targets within close proximity or multiple targets with only minor differences, however, even quality backprojection images may not provide enough

information to identify or distinguish between the targets-of-interest. These types of problems have provided motivation for research in various fields such as feature extraction and feature classification with application to SAR ATR.

### ***2.3.2 SPLIT Algorithm.***

The primary objective of the SPLIT algorithm is to classify canonical shape features corresponding to specific pixels within a 2D SAR image. In order to accurately assess each pixel for potential feature extraction and classification, several steps must first be accomplished. First, subimages are generated from raw phase history data using domain decomposition backprojection. Domain decomposition imaging reduces computational complexity in image formation by first creating coarse resolution subimages through sub-banding in frequency ( $H_\xi(\xi - \xi_c)$ ) and sub-aperturing in azimuth ( $H_\phi(\phi - \phi_c)$ ) [8]. Then, interpolating each subimage to a finer resolution and summing across all subimages provides a computationally efficient approximation of the backprojected image generated with the full phase history. Another benefit of using domain decomposition imaging is that peaks may be analyzed for persistence across subimages. Once all subimages are generated, a peak detection algorithm identifies subimage peaks at specific pixels within each subimage. If a peak is identified at the same pixel location across all subimages at a particular sub-aperture, that peak pixel demonstrates a slowly varying amplitude across frequency. Such pixels are identified as potential canonical scatterers and analyzed for feature extraction.

In order to correctly classify the canonical shapes within the image, distinguishing features between the shapes must be extracted from phase history data to reduce target ambiguity. One feature that may be extracted is the frequency parameter due to the varying responses received from the canonical shapes as shown in Table 2.1 [8]. The theoretical amplitude response from which the frequency response may be parameterized for the

Table 2.1: SPLIT frequency response for 3D canonical shapes [8]

3D Canonical	$\alpha$
<i>trihedral, dihedral</i> <sub>90</sub>	2
<i>cylinder</i> <sub>90</sub> , <i>tophat</i>	1
<i>sphere, plate, edge/wire</i> <sub>90</sub> , <i>dihedral</i> <sub>0</sub>	0
<i>cylinder</i> <sub>0</sub>	-1
<i>edge/wire</i> <sub>0</sub>	-2

canonical scatterers is [8]

$$S_f(f|A, \alpha) = A(jf)^{\frac{\alpha}{2}}, \quad (2.30)$$

where  $S_f$  is the amplitude function,  $f$  is the frequency of the incident electromagnetic field,  $A$  is the complex-valued amplitude based on the size of the canonical scatterer, and  $\alpha$  is the frequency response for a specific canonical shape that is extracted as the estimated frequency parameter  $\alpha'$ . SPLIT extracts the frequency parameter using an iterative curve fitting algorithm. A normalized frequency vector  $\mathbf{f}(\alpha')$  is first defined which represents the normalized values to which the frequency parameter  $\alpha'$  is estimated to best fit [8],

$$\mathbf{f}(\alpha') = \frac{[(f_{c1})^{\alpha'+2}, (f_{c2})^{\alpha'+2}, \dots, (f_{cl})^{\alpha'+2}]^T}{(f_c)^{\alpha'+2}}, \quad (2.31)$$

where  $f_{c1}, f_{c2}, \dots, f_{cl}$  is the center frequency for each subband and  $f_c$  is the center frequency over the entire bandwidth. An initial estimate of  $\alpha'$  may be extracted using the relationship between two subimage pixel intensities  $k_I$  at subimage pixel coordinates  $(m, n)$  and their corresponding subband center frequencies  $f_{cl}$  [8]

$$\frac{|k_1(m, n)|^2}{|k_I(m, n)|^2} \approx \left( \frac{f_{cl}}{f_c} \right)^{\alpha'+2}. \quad (2.32)$$

Solving for  $\alpha'$ , the first approximation of the frequency parameter may be extracted as [8]

$$\alpha' = \frac{\log\left(\frac{|k_1(m,n)|^2}{|k_j(m,n)|^2}\right)}{\log\left(\frac{f_{c1}}{f_{cl}}\right)} - 2. \quad (2.33)$$

The frequency extraction algorithm then continues to iteratively update  $\alpha'$  using a gradient descent technique until the adjustment value  $\delta_k$  falls below 0.01, at which point the value of  $\alpha'$  for the  $k^{th}$  iteration is set as the extracted frequency parameter for that particular peak pixel. Table 2.1 describes the expected SPLIT frequency response for the canonical shapes between  $[-2, 2]$ , so any extracted  $\alpha'$  values well outside of that range are not considered to be attributed canonical shape pixels. SPLIT sets a limit of  $[-6, 6]$  for the initial  $\alpha'$  estimate and  $[-4, 4]$  for the final extracted value of  $\alpha'$ . Although the acceptable final extraction range of  $[-4, 4]$  is outside of the ideal canonical shape frequency response range of  $[-2, 2]$ , extracted frequency parameters slightly greater than +2 or slightly less than -2 are still considered since such pixels also depend on extracted polarization parameters for accurate canonical shape classification. Using this method, the frequency parameter is only extracted from those pixels with stable subband image peaks that also demonstrate an extracted frequency value near the prescribed ranges of the canonical shape models.

To eliminate the remaining ambiguity of the frequency responses shown in Table 2.1, the SPLIT algorithm also extracts the polarization feature coefficients. Polarization features are extracted using the Krogager decomposition method described in Section 2.1 and utilized within saliency research [16].

The extracted frequency and polarization features are concatenated with their corresponding  $x$  and  $y$  pixel coordinates to form feature vectors. Once feature vectors have been extracted for all image peak pixels, SPLIT uses a Least Squares classifier [24] to ascribe pixels in a joint frequency-polarization feature space. The feature space is shown in Figure 2.1, broken down into canonical shape regions based on the ideal feature vector for each scatterer. Classification decisions are then made for each non-zero feature vector by calculating the Euclidean norm between an extracted feature vector and each of the

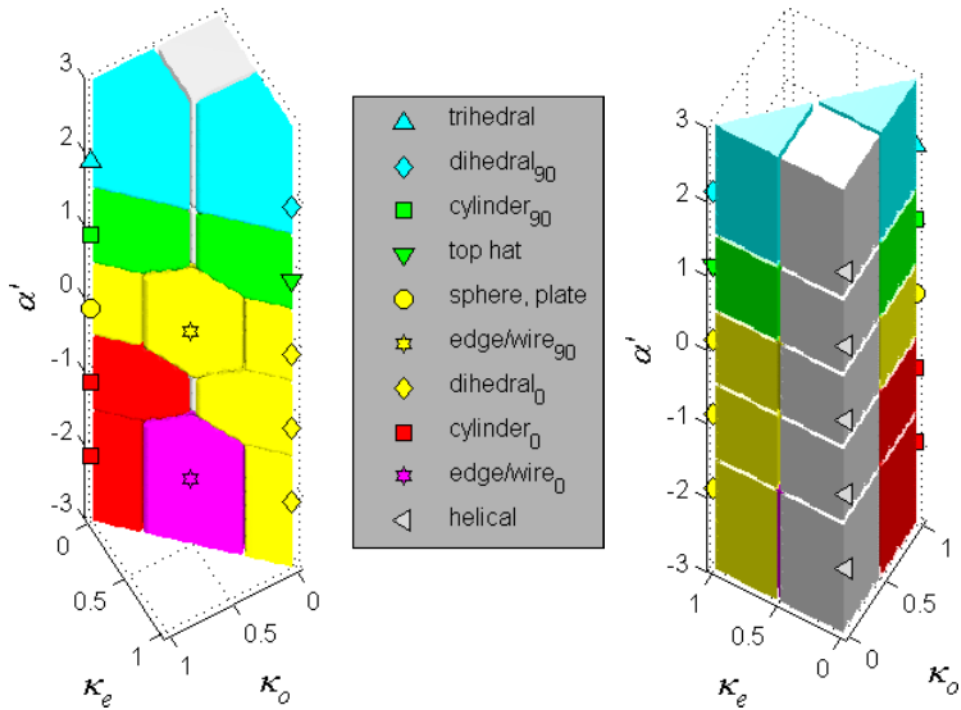


Figure 2.1: Least Squares classification decision boundaries for SPLIT in frequency polarization feature space [8].

ideal scatterer feature vectors. Each peak pixel is classified as the canonical scatterer with the minimum Euclidean distance calculation and mapped onto the 2D backprojection SAR image.

The advantages SPLIT can provide as a feature extraction technique may be demonstrated through a comparison of simulations. SAR images are produced from identical phase histories of civilian vehicles in AFRL's CV data domes using both traditional backprojection imaging and the integrated SPLIT algorithm. A 2D SAR amplitude-only image of a Nissan Maxima using backprojection is shown in Figure 2.2. All 360° of azimuth coverage are imaged with 10° subapertures. In addition, the full 5.35 GHz bandwidth was included to provide the best possible range resolution, and sampling

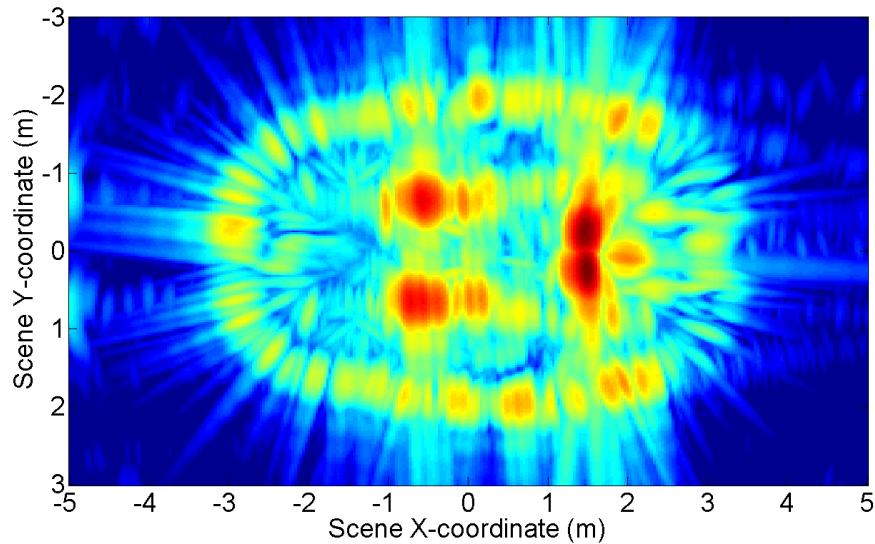


Figure 2.2: Traditional backprojection image of the Nissan Maxima,  $0^\circ - 360^\circ$  azimuth, VV polarization,  $40^\circ$  elevation, 5.35 GHz bandwidth.

was fine enough to avoid the effects of aliasing within the scene extent. The resultant image provides an amplitude at each pixel on the 2D grid corresponding to the amount of energy received by the radar at each point. Some useful target information can be drawn from the backprojected image. The general shape of the car can be identified by the outside ring in Figure 2.2 since the top edge of the car will return to the radar closest in range. The bright spots inside the outer ring identify the sides and back end of the Maxima, with the three highest-energy returns corresponding to the flat specular vehicle surfaces which create a double-bounce dihedral with the ground plane at more distant ranges.

While a wide-aperture, large bandwidth, finely sampled backprojected SAR image like Figure 2.2 can provide some useful target identification information, 2D pixel amplitudes alone may not provide enough information to distinguish between highly-similar target classes such as civilian vehicles. By accomplishing feature extraction and classification techniques, a second SAR image of the Nissan Maxima is produced

using the SPLIT algorithm, shown in Figure 2.3. Similar to Figure 2.2, the outside ring in the image identifies the roof line of the vehicle, and the brightest returns toward the center of the image correspond to the sides and back end of the Maxima. SPLIT provides additional distinguishing target information in Figure 2.3 based on the extracted frequency and polarization features. Extracting polarization coefficients using the Krogager decomposition provides even, odd, and helical bounce information about the target. In Figure 2.3, the red color on the outside ring confirms that the roof line of the vehicle reflected directly back to the radar with a single bounce, while the green color on the inside demonstrates that the transmitted radar waves bounced twice before returning to the radar. Combining the polarization features with the extracted frequency parameter and applying the classification algorithm to each of the peak pixels, distributed canonical scatterers are identified at the peak pixel locations as well. The curved roof line of the Maxima accurately identifies many horizontal cylinder scattering characteristics, while the front, sides and back of the vehicle demonstrate predominantly dihedral characteristics. As shown in the legend in Figure 2.3, SPLIT classifies nine different canonical shapes, with vertically oriented scatterers marked with a 90 subscript, and horizontally oriented scatters with a 0 subscript. The feature extraction techniques and classification of scattering behavior into physical target features accomplished by SPLIT provides excellent insight into the field of SAR binary target classification explored in our saliency research.

A second example of the SPLIT algorithm is accomplished to demonstrate feature extraction and classification results for a civilian vehicle with much different physical characteristics. A Toyota Tacoma pick-up truck is chosen, and the results are presented in Figure 2.4 and Figure 2.5. A clear difference in received energy compared to the Maxima can be seen in Figure 2.4 with large amplitude responses from the back half of the vehicle corresponding to the open cargo bed of the truck. In Figure 2.5, odd polarization response may be observed in the bed of the truck due to the trihedral triple-bounce presented by



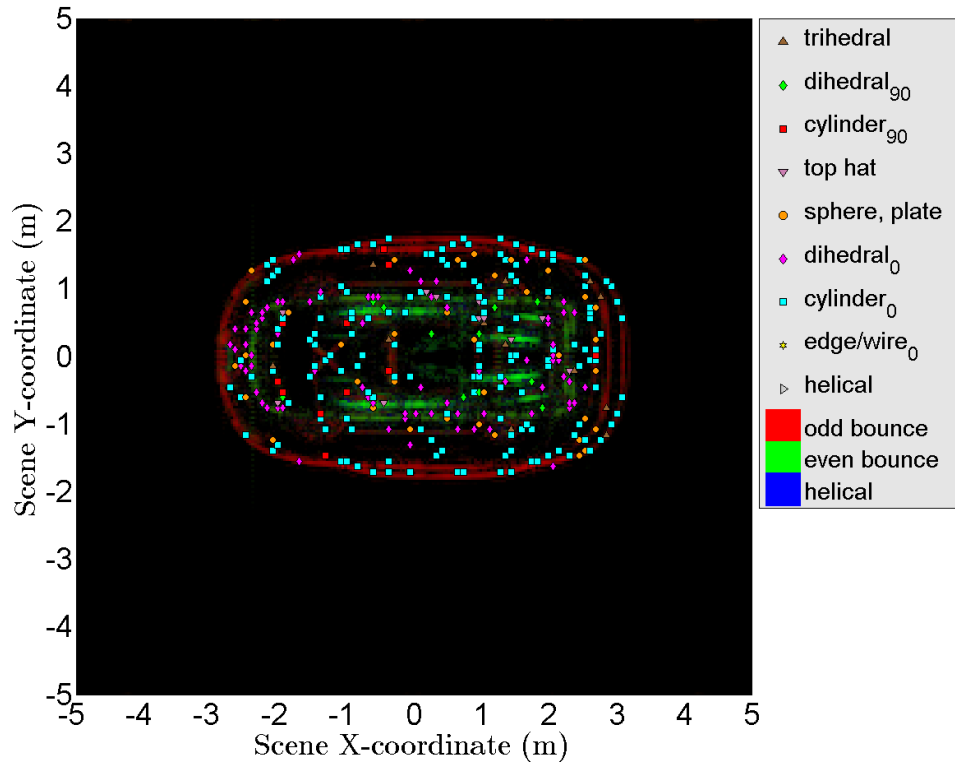


Figure 2.3: SPLIT image output result for Nissan Maxima,  $0^\circ - 360^\circ$  azimuth, VV Polarization,  $40^\circ$  elevation, 5.35 GHz bandwidth.

corner reflectors. Also of note in Figure 2.5 is the smaller roof line ring towards the center of the vehicle classified predominantly with horizontal cylinders. This small ring is distinctive of the pick-up truck due to the smaller roof line which, unlike other civilian vehicle classes, drops off into the cargo bed.

The results of the SPLIT algorithm may be used to directly aid in SAR ATR classification across similar target classes. Figure 2.6 and Figure 2.7 present one possible method for ATR classification analysis using SPLIT. Similar to results in [8], histograms are built from the Maxima and Tacoma results in Figure 2.3 and Figure 2.5. By comparing the total number of classifications for each canonical scatterer, conclusions may be drawn about a particular vehicle or vehicle class. For example, while many of the feature totals in

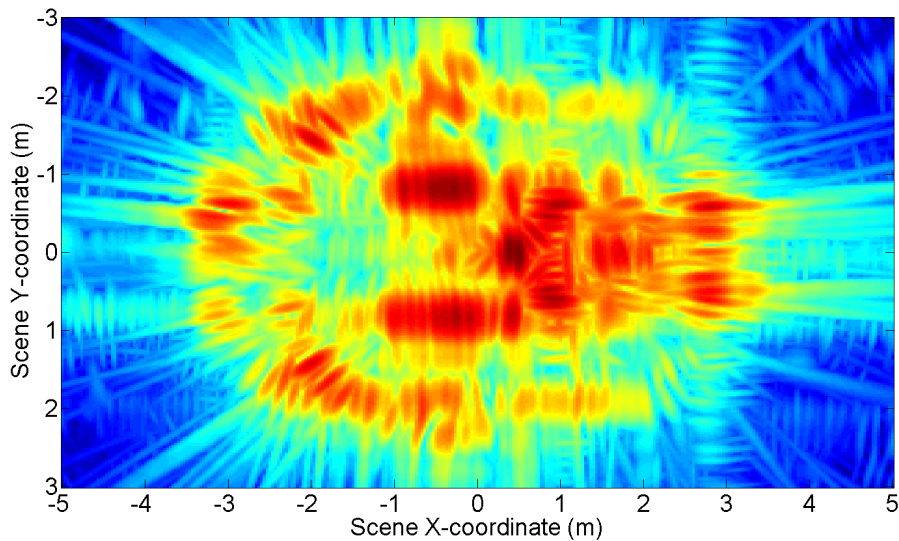


Figure 2.4: Traditional backprojection image of the Toyota Tacoma,  $0^{\circ} - 360^{\circ}$  azimuth, VV polarization,  $40^{\circ}$  elevation, 5.35 GHz bandwidth.

Figure 2.6 and Figure 2.7 are similar, Figure 2.6 demonstrates a higher number of horizontal edges and dihedrals (features 6 and 8) than Figure 2.7. Through analysis of many vehicles over various SAR collection parameters, trends in classified scatterer types for certain vehicles or over specific parameter values may be discovered to aid in ATR analysis. The saliency experiments in Chapter 3 and Chapter 4 adopt a variation of this analysis technique to highlight the most significant canonical scatterers contributing to sedan and SUV vehicle classification results.

The results of the SPLIT algorithm have proven to provide progress in the fields of SAR feature extraction and classification. One of the feature vector types implemented in our research uses the foundation laid by SPLIT to explore SAR binary vehicle classification with extracted SPLIT feature vectors. Both HRR and SPLIT feature vectors are extracted for the salient feature investigation. Vehicle class comparisons use the kernel-driven RVM

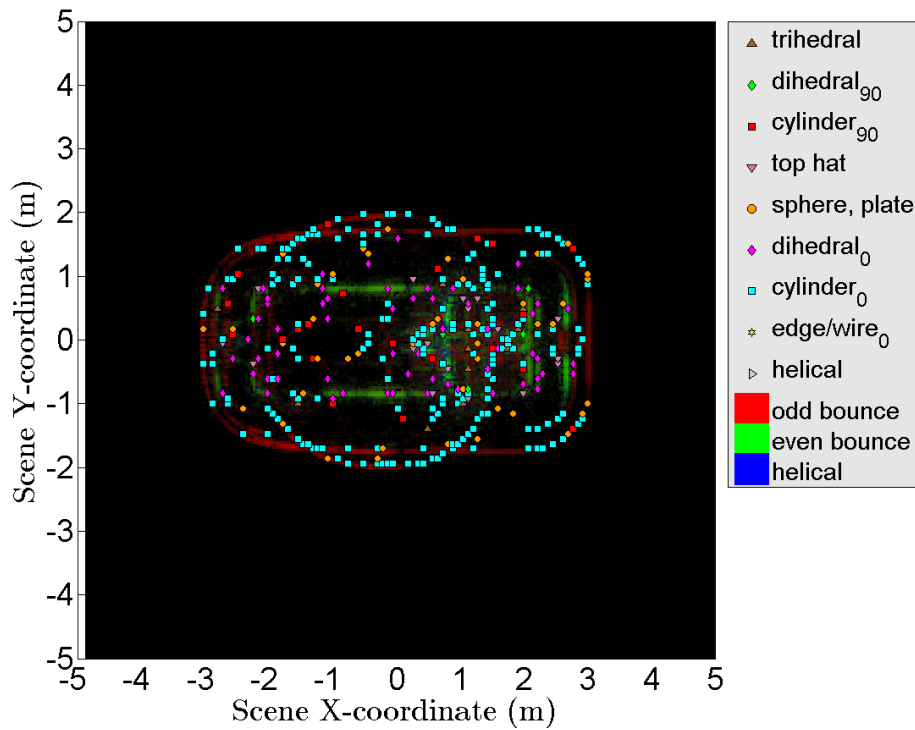


Figure 2.5: SPLIT image output result for Toyota Tacoma,  $0^\circ - 360^\circ$  azimuth, VV Polarization,  $40^\circ$  elevation, 5.35 GHz bandwidth.

classifier to reduce the complexity of phase history data by disregarding irrelevant or redundant feature vectors across data sets and highlighting only the most relevant feature vectors used for classification decisions. SAR binary vehicle classification is achieved through supervised machine learning so that the user may be alerted to the most relevant portions between two target classes. Determining the salient features across target classes and representing them in such a way to allow modeling, simulation, and ATR applications to focus on specific SAR collection parameters or target class features is the primary objective of the experiments and analysis which follow in Chapter 3 and Chapter 4.

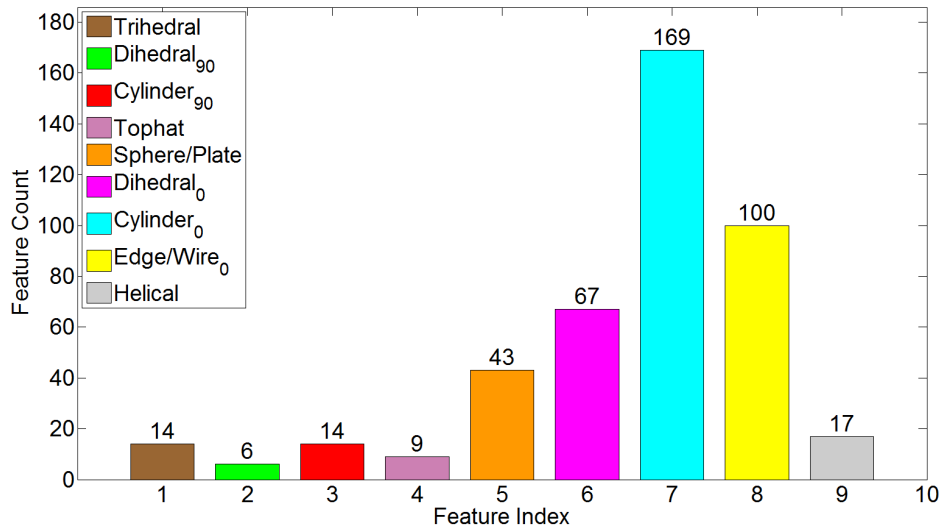


Figure 2.6: SPLIT canonical shape histogram for Nissan Maxima,  $0^\circ - 360^\circ$  azimuth, VV polarization,  $40^\circ$  elevation, 5.35 GHz bandwidth.

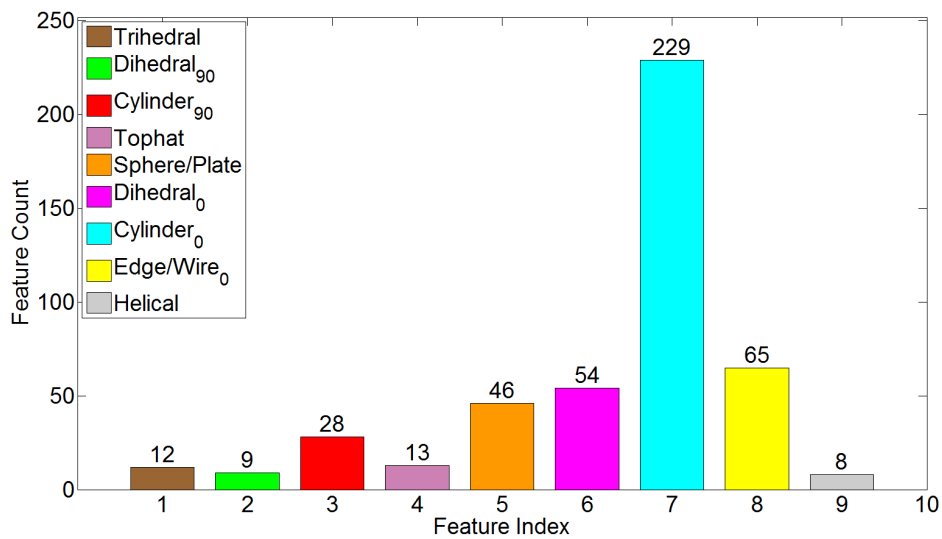


Figure 2.7: SPLIT canonical shape histogram for Toyota Tacoma,  $0^\circ - 360^\circ$  azimuth, VV polarization,  $40^\circ$  elevation, 5.35 GHz bandwidth.

### III. Methodology

The background material presented in Chapter 2 is now incorporated into the salient feature identification algorithm presented below. The algorithm aims to compare extracted target features to locate the feature vectors contributing most to decision boundary creation while making accurate classification decisions on input test data. Once salient feature vectors may be identified by implementing the algorithm presented in Section 3.1, a variety of experiments are presented in Section 3.2 to develop a methodology for locating the salient features and SAR collection parameters of a particular target or target class. A full analysis of salient feature experimental results is accomplished in Chapter 4. The feature vectors which demonstrate the best combination of kernel space separation and classification accuracy provide the greatest potential for effective SAR ATR, allowing ATR practitioners to focus primarily on the identified salient features and SAR collection parameters for improved performance of target classification results.

The salient feature identification algorithm is demonstrated using synthetically generated phase history data from both canonical shape scenes and AFRL's CV data domes. The publicly available CV data domes consist of fully polarimetric simulated phase history data for ten different models of civilian vehicles over  $0^\circ - 360^\circ$  in azimuth,  $30^\circ - 60^\circ$  in elevation, and a wide 5.35 GHz bandwidth [15]. The feature extraction process is demonstrated with canonical shape phase history data for simplicity, while the RVM classification process is illustrated with the more complex CV data domes.

The experiments detailed in Section 3.2 include two distinct classes of civilian vehicles for binary classification, the sedan class and the SUV class. The vehicles included for testing are presented in Table 1.1 along with the class of vehicle to which each belongs. In addition, Figure 1.1 illustrates the physical characteristics of the ten vehicles. All six of the sedan class vehicles share the same general physical characteristics which provides

advantages to classification accuracy due to the high level of similarity between training and testing target features. One of the SUV class vehicles, however, does not appear to belong with the other three vehicles in its class. It is by design that the Toyota Tacoma pick-up truck is used within the SUV class throughout our research to determine the negative effects on ATR classification results when training and testing target data sets contain significant differences in physical features.

It is important to take a moment to acknowledge those providing Matlab codes which are incorporated into the salient feature identification algorithm which follows. The HRR feature extraction code is provided by Dr. Sean Gilmore of Analytic Designs, Inc, and the SPLIT algorithm [8] code discussed in Section 2.3.2 is provided by Dr. Mike Saville of Wright State University. Lastly, the RVM classification code is provided by Signal Innovations Group, a company which has also conducted valuable research in the fields of salient feature analysis and SAR ATR [14]. These individuals play an integral role in the success of our research.

### **3.1 Salient Feature Identification Algorithm**

The salient feature identification algorithm involves several steps to highlight the most meaningful portions of an otherwise complex, ambiguous radar data set. First, SAR phase history data must be collected or synthetically generated over a target scene by specifying the radar flight path, radar parameters, and target scene reference point. Next, the phase history data is reformatted in preparation of the feature extraction process. Using the raw phase history data file, a structure is created which separates the data into three polarization channels:  $HH$ ,  $VV$ , and  $HV = VH$ . The corresponding azimuth angles, elevation angles, and frequency within each polarization channel are also stored within the data structure. The feature extraction process then extracts the frequency response and polarization coefficients according to the methods detailed in Section 2.1 and Section 2.3.2. Extracted features are concatenated into feature vectors for each target being analyzed.

Finally, training and test feature vectors are input into the RVM for classification decisions and identification of relevant vectors as described in Section 2.2.

The feature extraction step uses the methods detailed in Section 2.1 and Section 2.3.2 to extract the frequency response and polarization coefficient parameters from the complex phase history. To better illustrate the feature extraction process, an example is provided using simulated phase history data generated from a target scene containing three of the primitive canonical shapes from [7]. As proposed by Jackson [7], the majority of real-world targets may be broken down into these primitives, so beginning with a target scene consisting of only the 3D canonicals creates a reasonable progression in working up to complex targets such as civilian vehicles.

The target scene chosen for the feature extraction demonstration is shown in Figure 3.1. The three objects are the top-hat, sphere, and trihedral, or corner reflector, and all three objects are given different size parameters (height  $H$ , length  $L$ , and radius  $r$ ) and location parameters ( $X$ ,  $Y$ ,  $Z$ ), all in meters, while orientation parameters (roll  $\tilde{\gamma}$ , pitch  $\tilde{\theta}$ , and yaw  $\tilde{\phi}$ ), in units of degrees, are held constant. The parameters for all canonical shapes in the target scene are specified in Table 3.1.

Table 3.1: Canonical shape target scene parameters

	X(m)	Y(m)	Z(m)	L(m)	H(m)	r(m)	$\tilde{\gamma}^\circ$	$\tilde{\theta}^\circ$	$\tilde{\phi}^\circ$
Trihedral	-1	-1	0	0	0.12	0	0	0	0
Tophat	1	1	0	0	0.25	0.25	0	0	0
Sphere	0	0	0	0	0	0.25	0	0	0

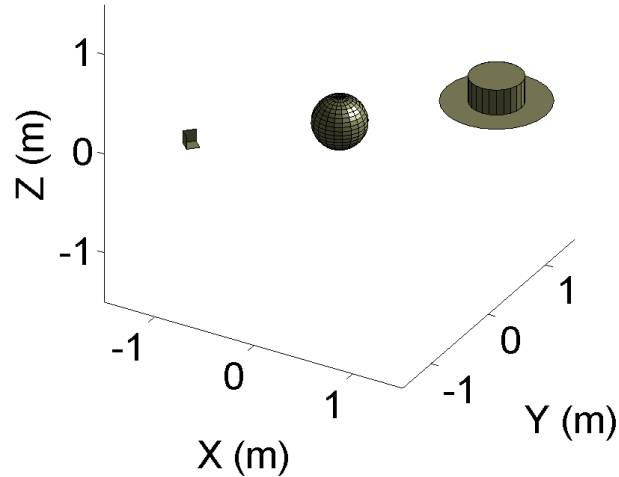


Figure 3.1: Canonical shape target scene image

The simulated radar flight path includes a full  $360^\circ$  of azimuth coverage at a constant elevation angle of  $40^\circ$  and a 2 GHz bandwidth. Generating the phase history data for this scenario produces the normalized return amplitudes illustrated as HRRs in Figure 3.2.

The radar is focused on the origin, so the strong sinusoidal response in Figure 3.2 corresponds to the top-hat which fluctuates in range to the radar depending on the location of the radar with respect to the origin. The lower amplitude response corresponds to the sphere, which remains at a constant range because it is located at the origin. While both the top-hat and sphere provide returns in phase history at all  $360^\circ$  of azimuth, the trihedral only provides returns to the receiver over a limited azimuth range when radar pulses are able to enter the corner reflector and are returned to the radar via a triple-bounce. Similar to the top-hat, the response from the trihedral also varies in range because it is not located at the radar's origin reference point.



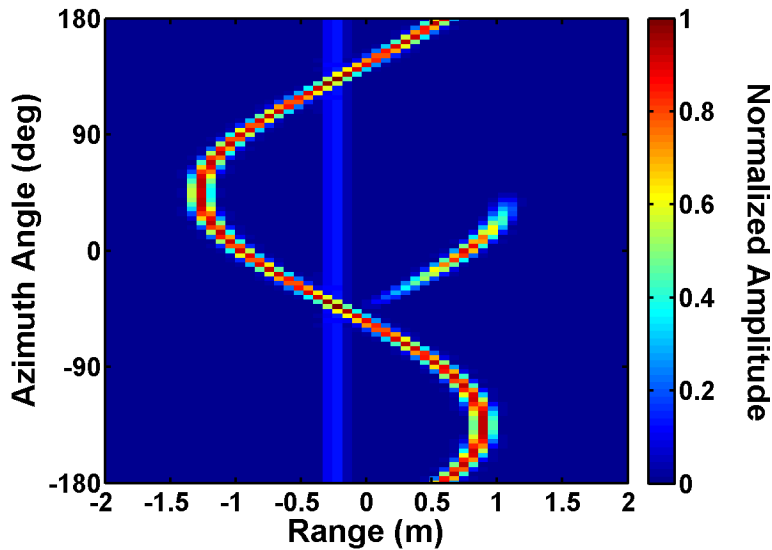


Figure 3.2: HRR profiles for canonical shape target scene,  $0^\circ - 360^\circ$  azimuth,  $40^\circ$  elevation, HH polarization channel, 2 GHz bandwidth. The top-hat is represented by the strong sinusoidal response, the trihedral is represented by the strong azimuth limited response, and the sphere is represented by the weak constant range response.

The frequency response parameter  $\alpha$  is extracted over the target scene and shown in Figure 3.3. As described in other feature extraction applications including [7] and [8], the 3D canonical shapes exhibit consistent frequency responses, which in this example include 1 for the trihedral, 0.5 for the top-hat, and 0 for the sphere. As shown in Table 2.1, the SPLIT algorithm uses comparable frequency responses multiplied by a factor of 2. The trihedral and top-hat shapes in the target scene may be clearly verified in Figure 3.3 for accurate frequency parameter extraction, while the sphere is somewhat overshadowed by the stronger returns from the other target scene shapes in keeping consistent with Figure 3.2.

Frequency response parameters alone may not provide enough information to resolve and classify targets for salient feature identification. To further reduce target ambiguity within the ATR process, polarization features are extracted using the Krogager basis

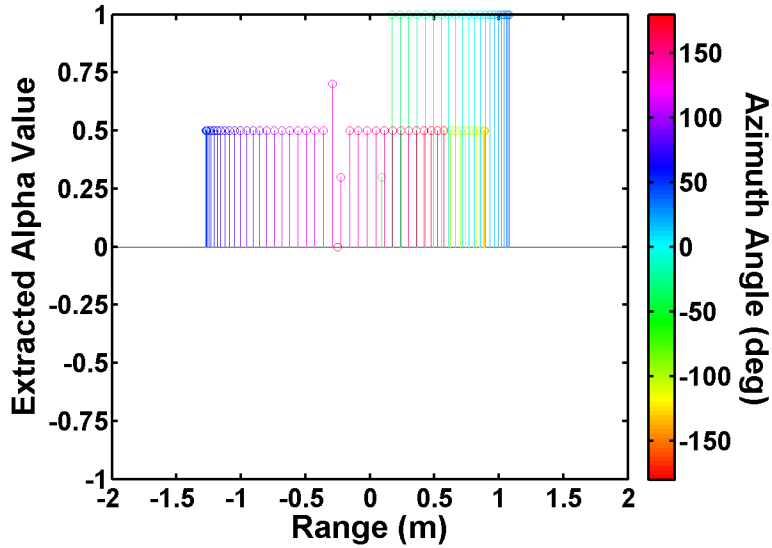


Figure 3.3: Extracted frequency response parameter  $\alpha$  for canonical shape target scene,  $0^\circ - 360^\circ$  azimuth,  $40^\circ$  elevation, VV polarization channel, 2 GHz BW.

decomposition [16]. The Krogager decomposition method extracts fully-polarimetric target information corresponding to even, odd, and helical bounce features from the SAR data. The extracted polarization response for the canonical shape scene example is shown in Figure 3.4. Observe in Figure 3.4 that the polarization features are accurately extracted as odd bounce for the sphere and trihedral and even bounce for the top-hat.

Extracting the frequency and polarization parameters as demonstrated in the canonical shape scene example provides a means to reduce ambiguity of the cumbersome SAR phase history data set. Using the extracted features to form feature vectors for RVM classification will serve to eliminate redundant and irrelevant phase history data, greatly improving computational efficiency while still ensuring the most accurate classification results. The first type of feature vectors are formed by concatenating the extracted frequency parameter  $\alpha$  with the corresponding Krogager polarization coefficients  $\kappa_e$  and  $\kappa_o$  for each received radar pulse at a particular azimuth  $\phi$  and range  $r$ . Together, these 1D HRR feature vectors,

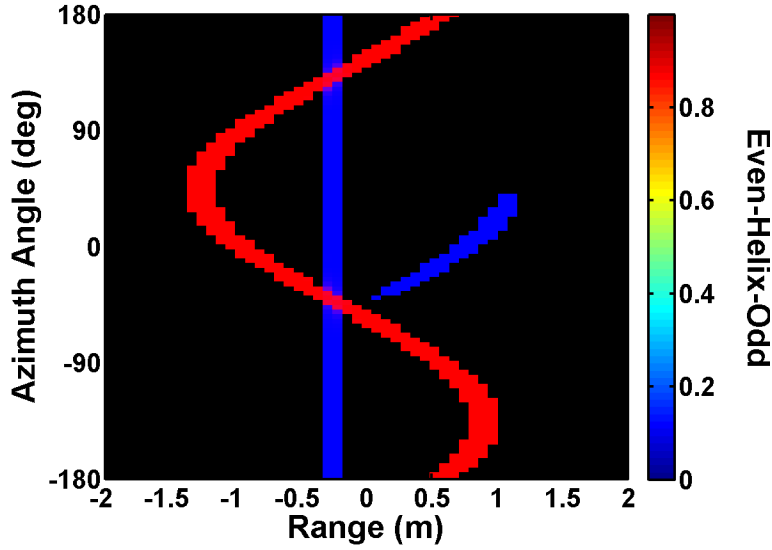


Figure 3.4: Extracted Krogager decomposition polarization response for canonical shape target scene,  $0^\circ - 360^\circ$  azimuth,  $40^\circ$  elevation, VV polarization channel, 2 GHz BW.

expressed as  $(\alpha, \kappa_e, \kappa_o, \phi, r)$ , comprise all received SAR feature data for a particular target scene. The second type of feature vectors are formed through implementation of the SPLIT algorithm [8]. SPLIT aims to increase confidence in pixel classification by instituting a more selective process of extracting features for only those SAR image pixels meeting all threshold conditions. These 2D SPLIT feature vectors may be expressed as  $(\alpha, \kappa_e, \kappa_o, x, y)$ . Creating the two types of feature vectors through feature extraction accomplishes the first major step in saliency characterization and leads to the classification step of the salient feature identification algorithm.

As discussed in Section 2.2.2, the kernel-based RVM provides a balanced approach to supervised learning by fitting the decision boundary to the training data to produce accurate classification decisions on test data through a sparse set of relevant vectors representative of the training data. Supervised machine learning begins by inputting the training data, in our case the extracted feature vectors, into the classifier. Appropriate choice of training

data for a particular test may have significant effects on classification performance, an issue further explored in Section 3.2. The RVM uses a Bayesian probability framework to compare the training data between the two classes using the specified kernel function. The kernel function transforms the training data to a higher dimensional kernel space to increase separability and fit a hyperplane decision boundary to the data by weighting each of the training feature vectors by their individual relevance to the classification process. The training feature vectors which do not contribute to the hyperplane boundary creation receive zero feature weight and are considered irrelevant. The remaining non-zero weighted feature vectors are the relevant vectors with the greatest impact on the supervised learning process.

Once the RVM has identified the sparse number of relevant vectors and is trained to achieve optimal classification results based on the input training data, test data is ready for feature classification. For the simulations conducted in our saliency research, in addition to highlighting the relevant vectors and their corresponding feature weights, the RVM identifies the probability of error in misclassifying test feature vectors. When incorporated into the test structure described in Section 3.2, all RVM outputs contribute to the saliency analysis for more effective ATR classification.

An example of the RVM classification process is provided to illustrate a comparison of sedan and SUV class vehicles. Specifically, the sedan class is trained with extracted feature vectors from the Civic, Maxima, Mitsubishi, Sentra, and Avalon and tested with the Camry. The SUV class uses the 93 Jeep, 99 Jeep, and Tacoma for training and the Mazda MPV for testing. Features are extracted for all vehicles at an azimuth of  $90^\circ$ , an elevation of  $40^\circ$ , an aperture size of  $\pm 2.5^\circ$ , and the full available bandwidth of 5.35 GHz. The RBF kernel is implemented as it is the most effective and commonly used kernel for ATR applications. Appropriate kernel choice is further discussed in Section 3.2. Table 3.2 specifies all input and output parameters for the RVM classification example, to include the

total number of relevant vectors identified and the max feature weight (MFW) and average feature weight (AFW) for both the sedan and SUV classes. Figure 3.5 illustrates the output feature vector weights for each class. In addition, Figure 3.6 and Figure 3.7 show all training and test feature vectors plotted in a 3D frequency-polarization feature space with the relevant vectors highlighted for both the sedan and SUV test cases, respectively. The identified relevant vectors represent the most impactful features of each target class for this particular test scenario and thus require the most attention for SAR ATR applications.

Table 3.2: AFRL CV data domes RVM classification example test results with extracted HRR feature vectors.

Sedan Train	SUV Train	Sedan Test	SUV Test	Kernel/BW	Ap. Size/Az/El
Civ/Max/Mits/Sen/Av	J93/J99/Tac	Camry	Mazda MPV	RBF/5.35GHz	$\pm 2.5^\circ/90^\circ/40^\circ$
# Train/Test	# RVs Sedan/SUV	% RV Sedan/SUV	MFW Sedan/SUV	AFW Sedan/SUV	$P_e$ Sedan/SUV
6149/1906	69/66	1.12/1.07	228.24/207.61	76.52/74.33	2.38/12.78

Several observations may be made in reference to the RVM classification example. The RVM assigned weights rank the relevance of each input feature vector for this particular test example, but the weight values do not translate for comparison to any future test cases. A feature vector with a weight of 200 in one test does not necessarily have equal classification relevance to a 200-weighted feature vector from a different test. For example, a very obscure physical target feature difference between two highly similar vehicles may be assigned a very large weight because it is the only identifiable feature between the two targets, while an easily distinguishable feature between two very dissimilar vehicles may be assigned a very low weight because it did not contribute to the decision boundary creation as much as other features. Therefore, feature vector weights including MFW and

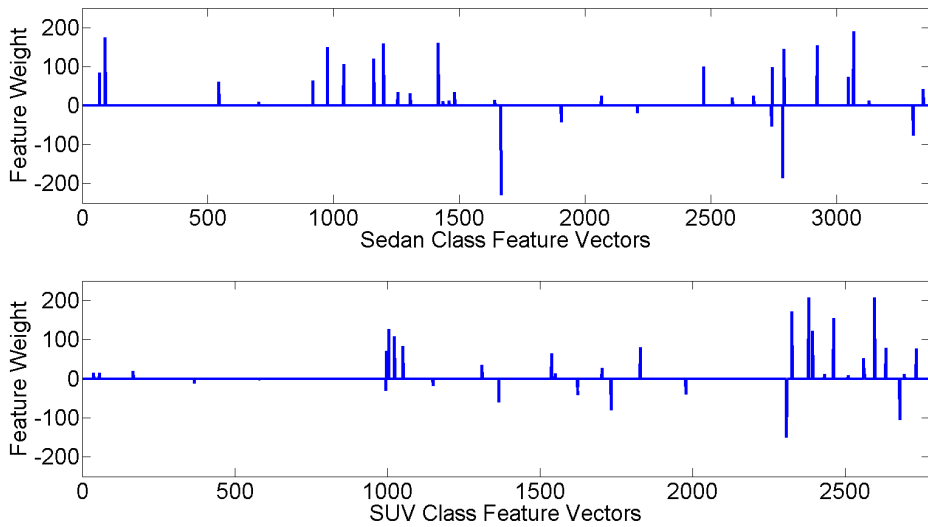


Figure 3.5: Example of RVM classifier HRR feature vector weights.

AFW determined by the RVM are not compared between test cases for contribution to the saliency investigation process. Additionally, while a single feature vector may carry a very high weight within one example, identifying that feature vector as relevant to classification, that same feature vector may carry a zero weight in many other examples. In such a case, the feature vector that is highly relevant to one specific classification test may not be considered salient across its target class.

### 3.2 Salient Feature Experiments

Feature saliency experiments are organized to highlight the most impactful features contributing to SAR ATR classification when comparing both physically similar and dissimilar target classes. A variety of feature classifications are conducted on extracted feature vectors from the sedan and SUV class vehicles listed in Table 1.1 by observing various parameter effects on feature saliency. Analysis of results reveal the feature vectors and SAR collection parameters that require the most attention from modelers and mission planners in real-world operational scenarios.

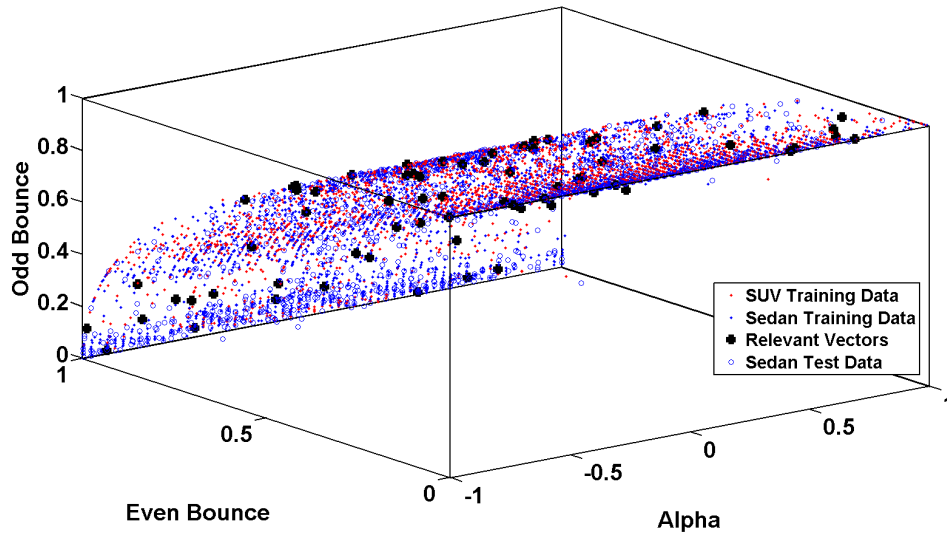


Figure 3.6: Frequency-polarization feature space illustration for an RVM example sedan class test vehicle with identified relevant HRR feature vectors highlighted as large black dots. Probability of RVM classification error for this sedan class test is 2.38%.

The inputs required for the experiments include both training and test SAR phase history data for each of the two classes being compared, the sedan class and the SUV class. In addition, the azimuth angle, aperture size, elevation angle, and bandwidth parameter settings of the extracted feature data sets must be recorded for analysis. The kernel chosen for the RVM classifier is another input that affects saliency results and must therefore be controlled.

Saliency results are determined within the experiments using a combination of several output metrics. The total amount of both extracted training and testing feature vectors classified are recorded along with a metric describing the percentage of training feature vectors identified as relevant. The total number of relevant vectors from each class are output, including the MFWs and AFWs for each set of relevant feature vectors. As previously discussed, the probability of error also plays an important role in determining

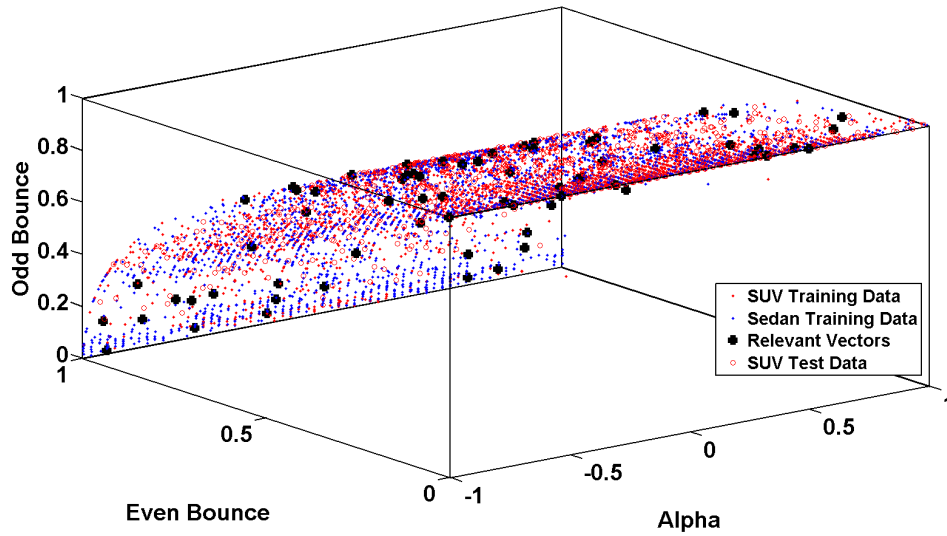


Figure 3.7: Frequency-polarization feature space illustration for an RVM example SUV class test vehicle with identified relevant HRR feature vectors highlighted as large black dots. Probability of RVM classification error for this SUV class test is 12.78%.

saliency for ATR because it highlights the accuracy of the RVM classifier for input test data.

The experiments discussed in detail below include comparisons in azimuth angle, aperture size, elevation angle, and bandwidth. The results are analyzed in Chapter 4 and presented as a guide to determining feature saliency for improved SAR binary classification performance. While our research investigates saliency using civilian vehicle SAR target data, the methodology developed for determining salient features may be applied to any class of SAR target data. For example, identifying the most impactful features for identification of various foreign aircraft or tanks may be of interest for future operational war time scenarios.

The radar's point of reference in all CV data domes experiments is the center of the vehicle in the ground plane and all angles, to include azimuth, elevation, and aperture



extent, are derived from that reference point. To illustrate the angular parameters being investigated for saliency, the left image in Figure 3.8 defines the azimuth angles and aperture size using a top-down view of a facet model of the Toyota Camry facing toward the right side of the page. The side view of the Camry seen in the right image of Figure 3.8 illustrates the elevation angle used within the experiments.

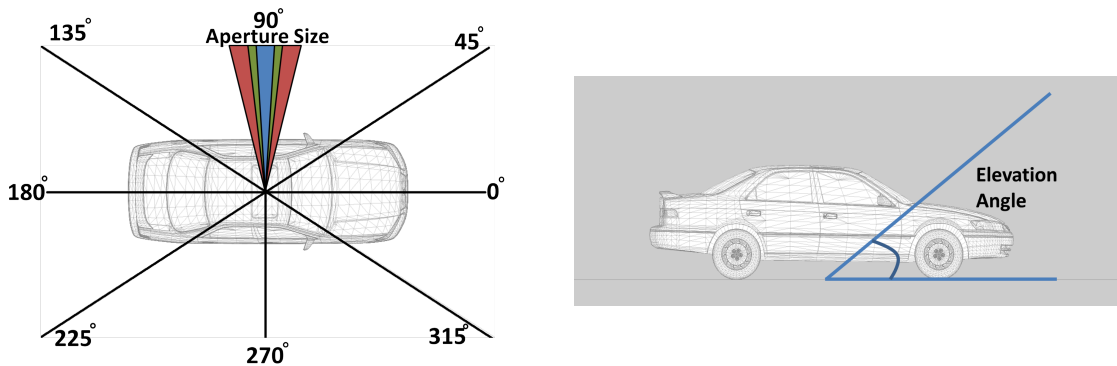


Figure 3.8: Parameter definitions for azimuth angle and aperture size (left image) and elevation angle (right image).

As previously mentioned, the choice of training data for the RVM classification process is important in achieving consistently accurate relevant feature vector results. The comparison between the two training classes establishes the classification decision boundary and lays the foundation for test data classifications. Therefore, there are several implications regarding test and training data relationships that must be considered for effective experimental design.

Consider first the relationship between the two sets of input training data. Since the two training data sets are compared for creation of the classification decision boundary, it is imperative that each set of training data represent its particular class as closely as possible in a general sense without over-fitting the training data to a specific portion of the class. For example, while the Toyota Camry is a sedan-class vehicle, training the sedan class with

only the Camry would create a decision boundary based on the physical characteristics of the Camry alone which may not adequately represent other sedan class vehicles. A balance must be achieved by training the sedan class to represent the “average” sedan. The best “average” sedan would include all available sedan class vehicles except for the sedan being tested. Likewise, the “average” SUV should include all available SUV class vehicles besides the SUV test vehicle. The test vehicle for each class must not be included in the training data set as it would over-fit the training data to the vehicles being tested and bias the classification test results.

The relationship between the training and test data sets is also important to effectively characterizing salience. Even if the RVM is well-trained to make accurate decisions between sedan and SUV class vehicles, test data sets must belong within the sedan and SUV classes as well or classification results may suffer. For example, if the RVM creates a hyperplane decision boundary in kernel-space with a large classification margin to make highly-accurate decisions between sedans and SUVs, classification results will still be poor if a tank is input for testing as it does not represent either of the classes the RVM was well-trained to model.

Taking into account the implications between training and testing data relationships, experiments using the 10 available CV data domes vehicles are shown in Table 3.3. The 24 experiments include all combinations of individual vehicle tests between the sedan and SUV classes with training data encompassing all remaining vehicles within each class. The 24 experiment set forms the foundation from which SAR collection parameters are adjusted for salient feature testing. The four SAR collection parameters investigated for salience are azimuth angle, elevation angle, aperture size, and bandwidth. The specific parameter values extracted for each set of experiments are shown in Table 3.4 for HRR feature vectors and Table 3.5 for SPLIT feature vectors.

Table 3.3: Training and testing vehicles defined for each of the 24 experiments.

Test #	Sedan Class Train	Sedan Class Test	SUV Class Train	SUV Class Test
Test 1	Civ/Max/Mits/Sen/Av	Camry	J99/Tac/MPV	Jeep93
Test 2	Civ/Max/Mits/Sen/Av	Camry	Tac/MPV/J93	Jeep99
Test 3	Civ/Max/Mits/Sen/Av	Camry	MPV/J93/J99	Tacoma
Test 4	Civ/Max/Mits/Sen/Av	Camry	J93/J99/Tac	MazdaMPV
Test 5	Max/Mits/Sen/Av/Cam	Civic	J99/Tac/MPV	Jeep93
Test 6	Max/Mits/Sen/Av/Cam	Civic	Tac/MPV/J93	Jeep99
Test 7	Max/Mits/Sen/Av/Cam	Civic	MPV/J93/J99	Tacoma
Test 8	Max/Mits/Sen/Av/Cam	Civic	J93/J99/Tac	MazdaMPV
Test 9	Mits/Sen/Av/Cam/Civ	Maxima	J99/Tac/MPV	Jeep93
Test 10	Mits/Sen/Av/Cam/Civ	Maxima	Tac/MPV/J93	Jeep99
Test 11	Mits/Sen/Av/Cam/Civ	Maxima	MPV/J93/J99	Tacoma
Test 12	Mits/Sen/Av/Cam/Civ	Maxima	J93/J99/Tac	MazdaMPV
Test 13	Sen/Av/Cam/Civ/Max	Mitsubishi	J99/Tac/MPV	Jeep93
Test 14	Sen/Av/Cam/Civ/Max	Mitsubishi	Tac/MPV/J93	Jeep99
Test 15	Sen/Av/Cam/Civ/Max	Mitsubishi	MPV/J93/J99	Tacoma
Test 16	Sen/Av/Cam/Civ/Max	Mitsubishi	J93/J99/Tac	MazdaMPV
Test 17	Av/Cam/Civ/Max/Mits	Sentra	J99/Tac/MPV	Jeep93
Test 18	Av/Cam/Civ/Max/Mits	Sentra	Tac/MPV/J93	Jeep99
Test 19	Av/Cam/Civ/Max/Mits	Sentra	MPV/J93/J99	Tacoma
Test 20	Av/Cam/Civ/Max/Mits	Sentra	J93/J99/Tac	MazdaMPV
Test 21	Cam/Civ/Max/Mits/Sen	Avalon	J99/Tac/MPV	Jeep93
Test 22	Cam/Civ/Max/Mits/Sen	Avalon	Tac/MPV/J93	Jeep99
Test 23	Cam/Civ/Max/Mits/Sen	Avalon	MPV/J93/J99	Tacoma
Test 24	Cam/Civ/Max/Mits/Sen	Avalon	J93/J99/Tac	MazdaMPV

All other parameters are held constant throughout the experiments, including the RBF kernel. One of the benefits of RVM classification is the ability to tailor classification testing based on the choice of kernel. The best kernel is one that accurately models both the

training and test data distributions being classified. A variety of existing kernels may be used or a kernel may be designed to fit the specific classifications being accomplished. Within our research, several kernels were implemented in initial testing, including the poly kernel, cross correlation, inner product, and RBF. As expected, the most effective kernel for classification testing was the RBF. The RBF kernel is best used for Gaussian-based data classifications, and the majority of data sets used for supervised learning fall into this category. In addition, the RBF kernel is the most widely used kernel for ATR applications involving kernel-based classifications. Considering the favorable initial test results and overwhelming acceptance within the ATR community, the RBF kernel is used exclusively throughout our salient feature research.

Table 3.4: SAR collection parameters for HRR feature vector experiments

Test Set	Azimuth(s)	Elevation(s)	Aperture Size(s)	BW(s) (GHz)	Kernel
Az Tests	0°, 23°, 45°, 67°, 90°, 112°, 135°, 157°, 180°, 270°	40°	±2.5°	5.35	RBF
El Tests	90°, 180°	30°, 40°, 50°	±2.5°	5.35	RBF
Ap Size Tests	90°, 180°	40°	±1.5°, ±2.5°, ±5°	5.35	RBF
BW Tests	90°, 180°	40°	±2.5°	0.64, 3.0, 5.35	RBF

Table 3.5: SAR collection parameters for SPLIT feature vector experiments

Test Set	Azimuth(s)	Elevation(s)	Aperture Size(s)	BW(s) (GHz)	Kernel
Az Tests	0°, 45°, 90°, 135°, 180°	40°	±45°	5.35	RBF
El Tests	45°	30°, 40°, 50°	±45°	5.35	RBF
Ap Size Tests	90°	40°	±30°, ±45°, ±60°	5.35	RBF
BW Tests	135°	40°	±45°	0.64, 3.0, 5.35	RBF

Salient feature experiment results and analysis for extracted HRR feature vectors are included in Section 4.1.1 through Section 4.1.4. The salient feature experiment results and analysis for extracted SPLIT feature vectors may be found in Section 4.2.1 through Section 4.2.4. Unless otherwise noted, all tables containing experimental results are presented as the combined means of all 24 individual tests. In many cases, reducing an entire set of experiments to the mean outputs allows for easier comparison of general test results across a specific test parameter or class for clearer saliency recommendations. The figures which accompany each set of experiments illustrate both individual test results as well as overall means. The ultimate goal of the saliency experiments is to identify and provide recommendations as to the specific feature vectors and SAR collection parameters which provide the most impact to the SAR ATR classification process so that modelers and ATR practitioners may save time and resources by focusing more attention on the salient aspects of a SAR target.

## IV. Results and Analysis

### 4.1 Salient Feature Experiments for HRR Feature Vectors

The first type of feature vector explored in our saliency investigation is the HRR feature vector. As discussed in Section 2.1, the extracted 1D HRR feature vector may be expressed as  $(\alpha, k_e, k_o, \phi, r)$ . Saliency experiment results using the HRR feature vector are included in Section 4.1.1, Section 4.1.2, Section 4.1.3, and Section 4.1.4 below, followed by experimental results using the extracted SPLIT feature vector.

#### *4.1.1 Azimuth Angle Saliency Experiments for HRR Feature Vectors.*

The first set of HRR experiments into target class saliency investigate the effects of azimuth angle. Besides azimuth angle, all other SAR collection parameters are held constant to ensure that any improvements or degradations in classification performance may be attributed solely to radar azimuth. Therefore, all SAR target feature vectors are extracted at  $40^\circ$  elevation with an aperture size of  $5^\circ$  total, or  $\pm 2.5^\circ$  to either side of the center azimuth, and the full 5.35 GHz of available bandwidth (BW). Additionally, the RBF kernel is implemented for all RVM classifications.

Ten different azimuth angles are tested for saliency, beginning with the front of the vehicles ( $0^\circ$ ) and testing through the rear of the vehicles ( $180^\circ$ ) in  $22.5^\circ$  increments to fully characterize azimuth saliency on one half of each vehicle. Since vehicles are symmetric, it is only necessary to test azimuth angles between  $0^\circ$  and  $180^\circ$ , but one additional azimuth angle is tested on the opposite half of the vehicles at  $270^\circ$ . This tenth and final azimuth angle is included in testing to compare with the results from its counterpart ( $90^\circ$ ) to ensure consistency within saliency results. The results in Table 4.1 highlight the performance of the sedan class vehicles compared with the SUV class vehicles at the specified azimuths. Each azimuth result in Table 4.1 represents the mean results of all 24 experiments illustrated in Table 3.3.

Table 4.1: Mean results for azimuth angle experiments 1 – 24 at 40° elevation,  $\pm 2.5^\circ$  aperture size, and 5.35 GHz bandwidth.

Az	# Train/Test	# RVs	% RV	MFW	AFW	$P_e$ %
		Sedan/SUV	Sedan/SUV	Sedan/SUV	Sedan/SUV	Sedan/SUV
0°	8416/2093	83.00/83.13	0.98/0.99	293.56/262.95	61.68/57.87	8.78/30.95
22.5°	12491/3265	98.08/98.04	0.78/0.78	253.92/238.87	58.23/55.61	9.14/21.43
45°	16215/3937	86.96/86.92	0.54/0.54	177.63/184.06	37.03/37.17	6.56/19.61
67.5°	12338/3039	74.79/75.12	0.60/0.61	242.06/225.79	55.04/52.91	3.20/35.50
90°	6413/1642	61.79/60.79	0.96/0.94	409.87/430.98	84.82/83.83	4.42/31.24
112.5°	15269/3868	64.41/63.79	0.42/0.41	160.11/152.50	34.18/42.59	2.29/18.17
135°	19022/4553	81.58/78.87	0.43/0.41	139.08/125.28	32.90/30.54	0.79/49.11
157.5°	16595/4145	81.62/79.20	0.49/0.47	127.39/120.15	28.80/26.64	2.76/30.41
180°	8511/2063	75.45/75.41	0.88/0.88	143.94/129.40	36.09/34.46	4.86/38.08
270°	6304/1612	61.62/61.95	0.97/0.98	591.14/590.01	98.14/97.62	4.40/29.15

To better illustrate the findings summarized in Table 4.1, Figure 4.1 through Figure 4.4 highlight the results for each of the 24 individual azimuth saliency experiments along with the mean for each set of experiments. In addition to comparing the ten azimuth angles under investigation, each figure separates the results of the sedan and SUV vehicles at each azimuth for ease of class comparison.

Figure 4.1 illustrates the total number of HRR feature vectors incorporated for training and testing within the RVM at each azimuth angle. The large differences between the number of training and testing HRRs corresponds to the number of vehicles being trained versus tested for each experiment. As shown in Table 3.3, five sedans and three SUVs are used for training each experiment, while only one sedan and one SUV are used for testing. Therefore, each set of training HRR feature vectors is approximately four times larger than its corresponding set of test feature vectors. When comparing across azimuth

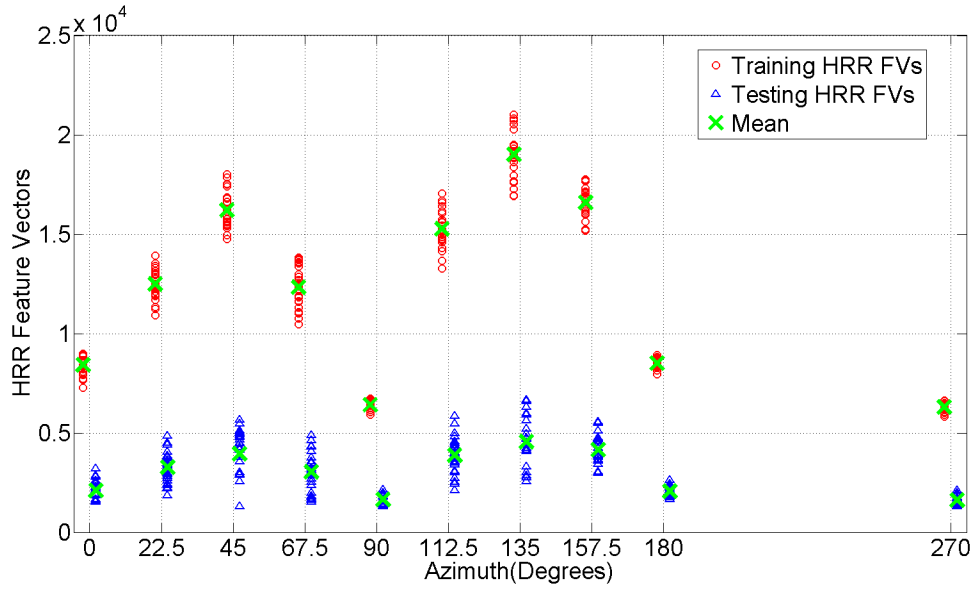


Figure 4.1: Total extracted train and test HRR feature vectors for azimuth angle experiments.

angles, notice that the canted vehicle azimuths(22.5°, 45°, 67.5°, 112.5°, 135° and 157.5°) produce significantly more training and test feature vectors over the same aperture size as the specular azimuths(0°, 90°, 180° and 270°). The largest amount of training and testing data for the front and rear of the vehicles correspond to the vehicle corners at 45° and 135° azimuths. The increase in SAR data at the corner azimuths may be attributed to the physical characteristics of the targets. At an elevation of 40°, the airborne radar radiates a larger amount of the vehicle surface that is directly returned to the receiver at the angled azimuths than it does at the flat surface azimuths. While more computationally expensive, the additional target feature vectors may provide benefits to ATR since more feature data at the canted azimuths creates an increased opportunity to characterize salience.

The total number of relevant vector (RV)s identified by the RVM at each azimuth are shown in Figure 4.2. Observe that while Figure 4.1 demonstrates fairly large differences in



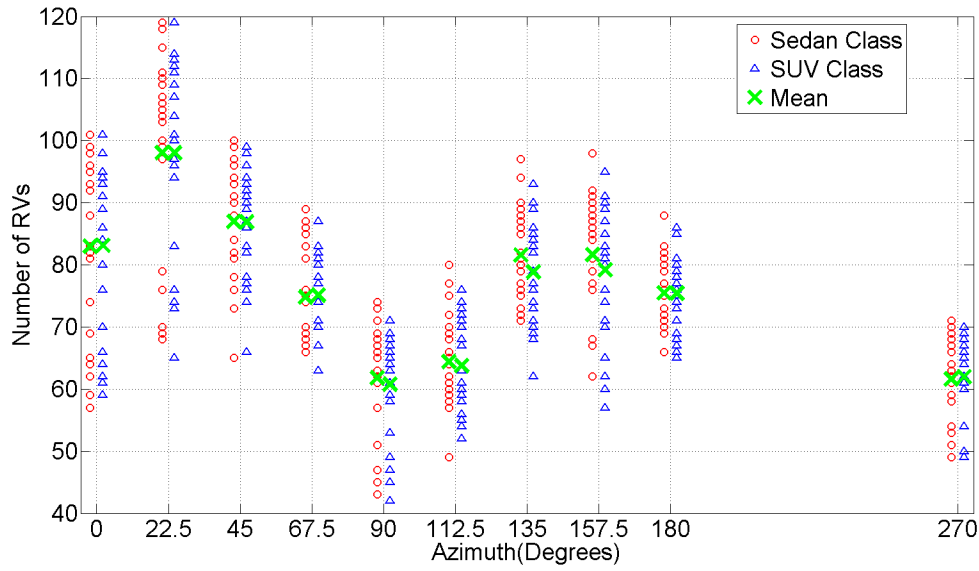


Figure 4.2: Total identified relevant HRR feature vectors for azimuth angle experiments.

the amount of training and test data at each azimuth, many of the azimuth angles found similar relevant feature vector counts. The proficiency with which RVs are identified may be further explored in Figure 4.3. It is clear in Figure 4.3 that the specular vehicle surfaces contain the highest ratio of RVs to total training HRR feature vectors, identifying approximately 1% of training data as relevant to classification decisions. Alternatively, the canted azimuths demonstrate the lowest ratio of RVs to training data, with the rear vehicle canted azimuths ( $112.5^\circ$ ,  $135^\circ$  and  $157.5^\circ$ ) all averaging less than 0.5% of relevant training feature vectors. As Tipping [13] suggests with the creation of the RVM [13], a sparse solution is desirable to separate the two classes as efficiently as possible. The three rear canted azimuths demonstrate the sparsest RVM training solution. While the four specular azimuths produce a higher percentage of RVs due to the limited amount of training feature vectors, the rear specular azimuth ( $180^\circ$ ) proves slightly more compressible in creating the decision boundary between the sedan and SUV classes. The initial azimuth test results

therefore indicate an area of interest in regards to saliency at the rear vehicle azimuths, especially the rear canted azimuth angles.

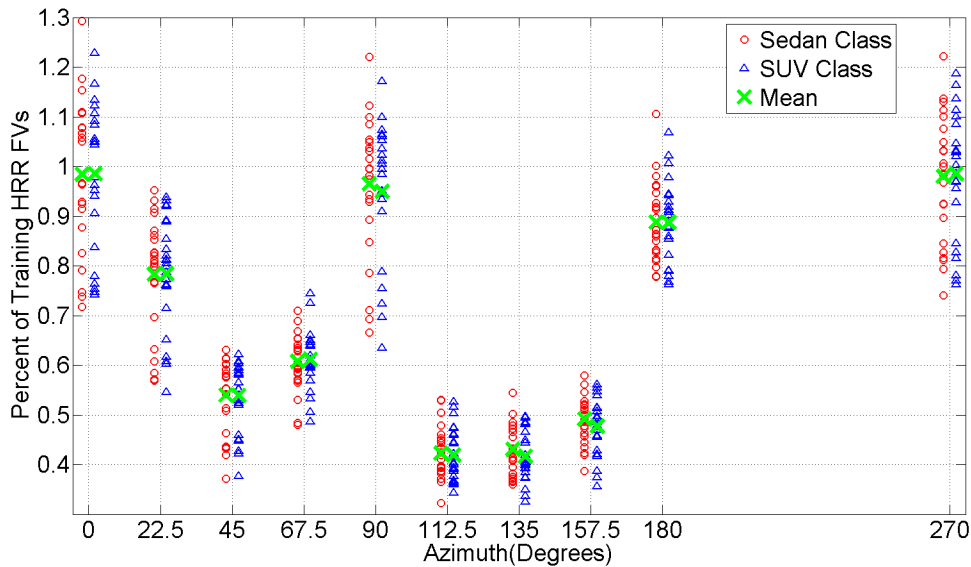


Figure 4.3: Percent of training HRR feature vectors deemed relevant for azimuth angle experiments.

The next factor in determining azimuth saliency for ATR classification involves examining probability of test classification error. Probability of error values for HRR feature vectors across all tested azimuths are shown in Figure 4.4. Error calculations are separated by individually training each class with the appropriate sedan and SUV vehicles but only testing with either one sedan or one SUV test vehicle at a time to determine individual class accuracy. As shown in Figure 4.4, the  $P_e$  results are quite different between the two classes across varying azimuth. In particular, the sedan class performed well in most experiments while the SUV class demonstrated many poor classification test results. Several factors may explain the inconsistencies in error calculations. The sedan class of the CV domes data set contains six total vehicles, while the SUV class contains only four.

The mismatch forces the sedan class to be trained with five vehicles in each test, while the SUV class is trained with only three. The additional training data in the sedan class helps characterize the class more robustly prior to classification testing. In addition, the six sedan class vehicles are more similar in terms of physical features than the four SUV class vehicles. While the SUV class does contain two different models of Jeep, it also contains a Mazda MPV, which may be considered more of a mini-van than an SUV, and a Toyota Tacoma, which is an open bed pick-up truck. Therefore, the initial azimuth RVM classification test results are not discouraging, but encouraging, because they expose the aforementioned inconsistencies within the class data.

First analyzing the sedan class results in Figure 4.4, observe that the front vehicle azimuths from  $0^\circ - 90^\circ$  demonstrate a higher average classification test error than the rear vehicle azimuths from  $90^\circ - 180^\circ$ . The favorable rear aspect  $P_e$  results are consistent with the initial sparse RV training results found at the rear canted azimuths, adding to the case of saliency for the rear azimuths. The SUV results are much more sporadic, with several SUV class tests demonstrating a classification error of greater than 50%. Upon further investigation, the majority of the results with greater than 50% error came from experiments with the Tacoma pick-up truck as the test vehicle. Even if the SUV class is well trained with three similar SUV class vehicles, when classification decisions are made with a vehicle as physically dissimilar as a truck, classification test errors will be high as demonstrated here. The poor SUV classification results tend to be slightly worse for the rear vehicle azimuths compared to the front. The results may be attributed to the fact that the most significant physical differences between the SUV vehicles are found from azimuths  $90^\circ - 180^\circ$  (i.e. the open bed of the Tacoma).

Considering all factors, notice that one azimuth outperformed all others in HRR classification tests. Azimuth  $112.5^\circ$  demonstrated the lowest average  $P_e$  for SUV tests and one of the lowest  $P_e$  averages for sedan tests. Azimuth  $112.5^\circ$  also belongs to the rear

canted azimuth group previously deemed an area of interest in terms of saliency due to the sparse identification of RVs. Initial investigation into the nature of saliency with extracted HRR feature vectors has therefore highlighted  $112.5^\circ$  as the most desired azimuth tested, followed by  $157.5^\circ$  as the second most desired azimuth. Also note that very similar  $P_e$  results for both SUV and sedan testing were found at  $90^\circ$  and  $270^\circ$  azimuths, providing verification of consistency within the salient feature identification algorithm at the two corresponding azimuths.

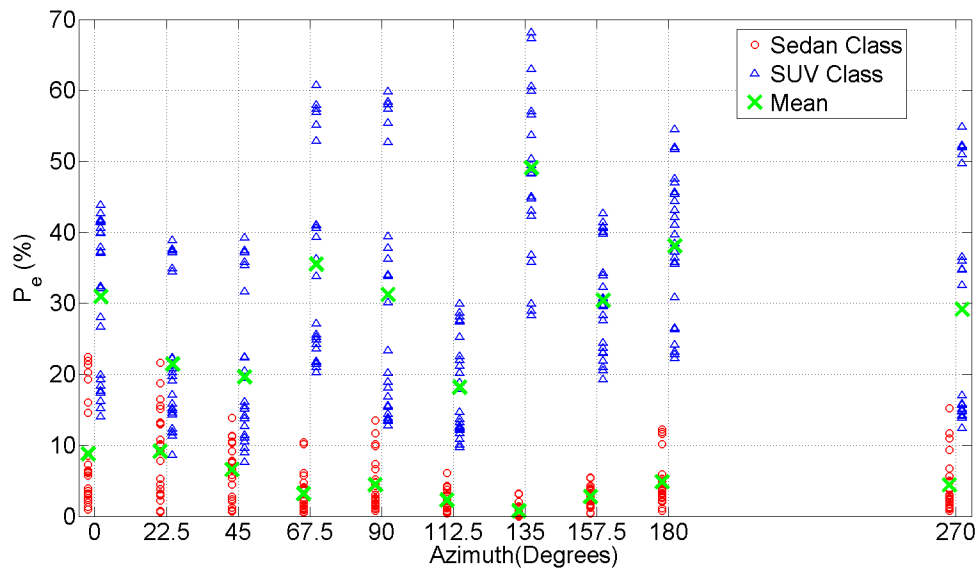


Figure 4.4: Probability of RVM classification error for extracted HRR feature vectors as seen throughout azimuth angle experiments.

Even with the identification of azimuth angles contributing most to effective SAR binary classification, additional ATR aid may be provided by highlighting physical features on the vehicle surfaces which are consistently relevant to classification decisions at the desired azimuths. One method to highlight the physical features is adopted from the SPLIT algorithm [8] and involves tracing the extracted frequency and polarization features to the

canonical shape with the most similar ideal features. The primary difference from an ATR stand point is that while SPLIT classifies image pixels deemed as peaks for a single vehicle, we are classifying first HRR feature vectors, followed later by SPLIT feature vectors, that are deemed most relevant to the separation of the two vehicle classes. In doing so, the physical features identified most often are considered the salient target features that have the greatest impact to target class identification of the sedan and SUV vehicles at the specified parameters and should therefore be given the most attention for SAR ATR applications.

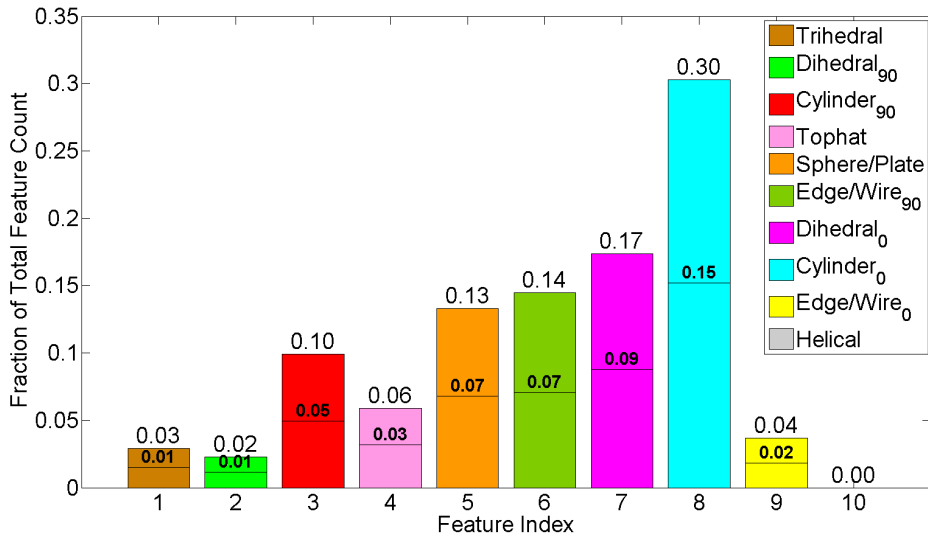
Several example histograms are provided below that identify the most common canonical shapes corresponding to the RVs provided by the RVM at the specified azimuths. In each example, all extracted feature vectors are classified in one histogram, and only the relevant feature vectors are shown in a second histogram. Including a second plot illustrating all extracted feature vectors for the specified parameters allows for analysis of which canonical features were emphasized and which were deemphasized by the RVM classifier. Additionally, a dividing line included in each feature bar distinguishes the class origin of feature vectors, with sedan features below the line and SUV features above the line.

In Figure 4.5a for  $90^\circ$  azimuth, horizontal cylinders parallel with the ground plane are the most common RV highlighted, followed by horizontal dihedrals with the folded edge parallel to the ground plane. The result makes intuitive sense since a large amount of radiated energy at the  $90^\circ$  specular azimuth is returned from the roof line of the vehicles as well as the double-bounce reflection between the side of the vehicles and the ground plane. It is therefore important for ATR effectiveness that the roof line of the vehicles at  $90^\circ$  be properly modeled for improved separation and class identification. Horizontal cylinders and horizontal dihedrals are also the two most common shapes across all extracted HRR feature vectors in Figure 4.5b. While the RVM increased dependence on horizontal

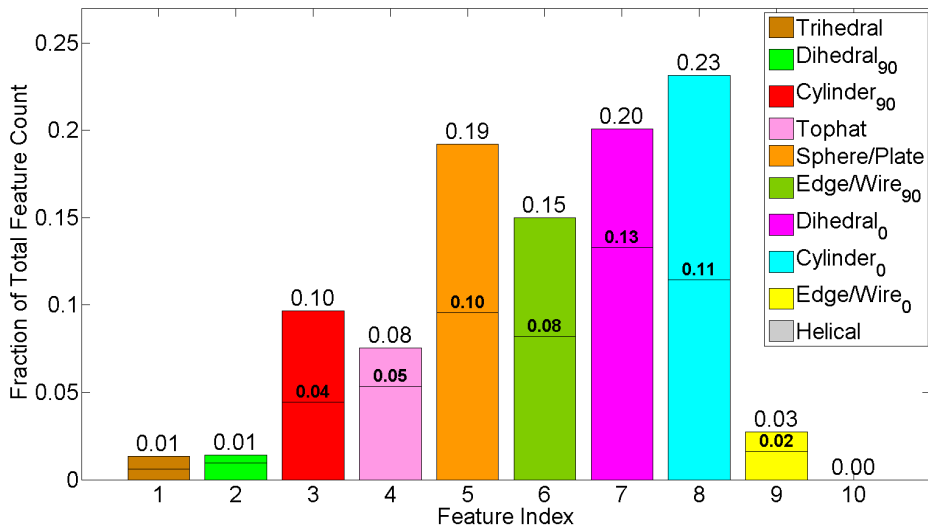
cylinders, other canonicals such as horizontal dihedrals and sphere/plate features were deemphasized within the classification process.

Histogram results for another specular azimuth,  $180^\circ$ , are shown in Figure 4.6. Similar relevant canonical shape results are demonstrated, with two notable exceptions. First, there is a significant increase in vertical cylinders perpendicular to the ground plane being identified as relevant. The result requires that any side-to-side curved surface features from the rear aspect of the vehicles be paid close attention for improved classification performance. Second, RVM results at  $180^\circ$  azimuth demonstrate a large amount of trihedral features as relevant to vehicle classification decisions. Some of the most common shapes across all extracted feature vectors are devalued, while some less common features, such as trihedrals, are given increased significance by the RVM. The trihedral features toward the rear aspect of the vehicles may be found in small crevices, most notably in the corner reflections returned from the bed of the Tacoma pick-up truck.

Focusing now on the azimuths identified as desired to target class identification, RV shape classification histograms are shown for  $112.5^\circ$  and  $157.5^\circ$  in Figure 4.7 and Figure 4.8, respectively. At both azimuths, the three most relevant canonical shapes for target class identification are horizontal cylinders, horizontal dihedrals, and vertical edges/wires. The sharp increase in edge/wire classifications may be attributed to the fact that at the canted azimuths, less radiated energy is directly returned to the radar from large flat vehicle surfaces and much of the energy that is received is derived from more obscure vehicle features with leading edges such as door handles, gas doors, and wheel wells. Sharper focus on the smaller, more unique features of the sedan and SUV class vehicles at the desired rear canted azimuths, specifically  $112.5^\circ$  and  $157.5^\circ$ , provides the most potential for effective SAR binary classification performance with extracted HRR feature vectors.

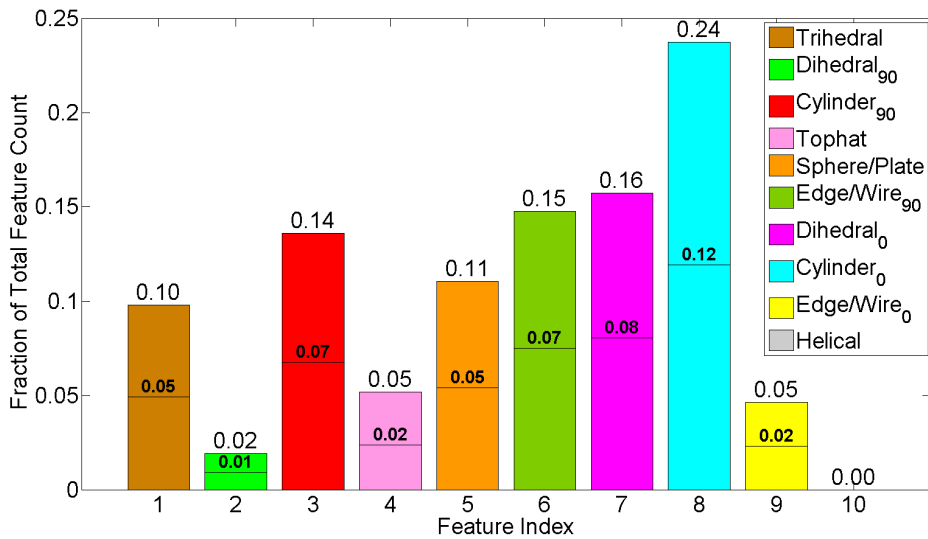


(a) Identified Relevant HRR Feature Vectors Only

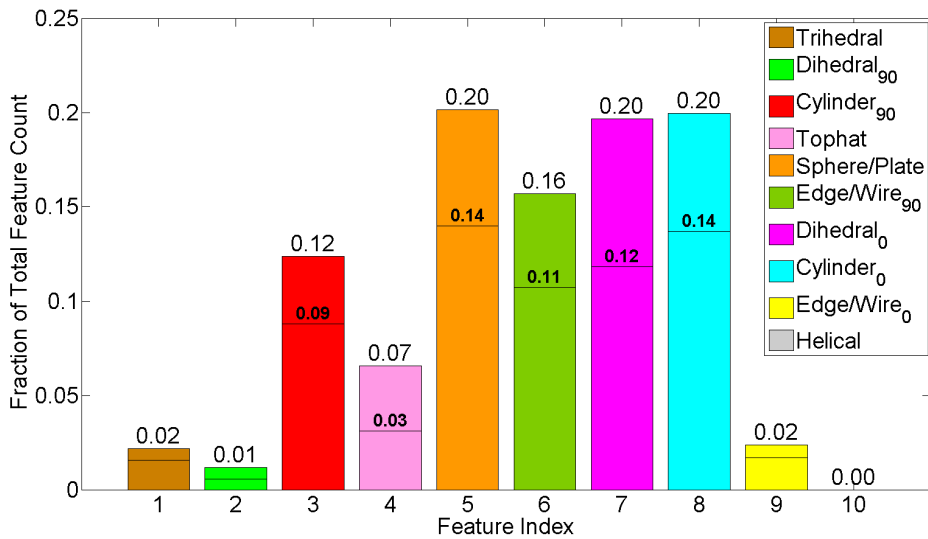


(b) All Extracted HRR Feature Vectors

Figure 4.5: Azimuth angle experiment histograms for HRR FVs ( $Az\ 90^\circ$ ). The dividing line illustrated on each canonical feature bar separates FVs according to class origin with sedan FVs below the line and SUV FVs above the line. The value over each dividing line indicates the fraction of only sedan FVs, and the value at the top of each feature bar indicates the fraction of all FVs classified as the specified canonical shape.



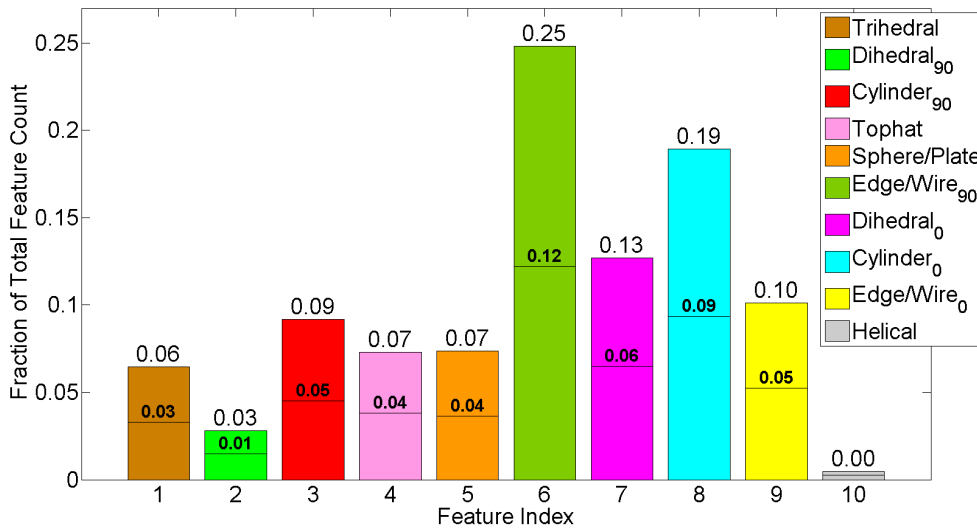
(a) Identified Relevant HRR Feature Vectors Only



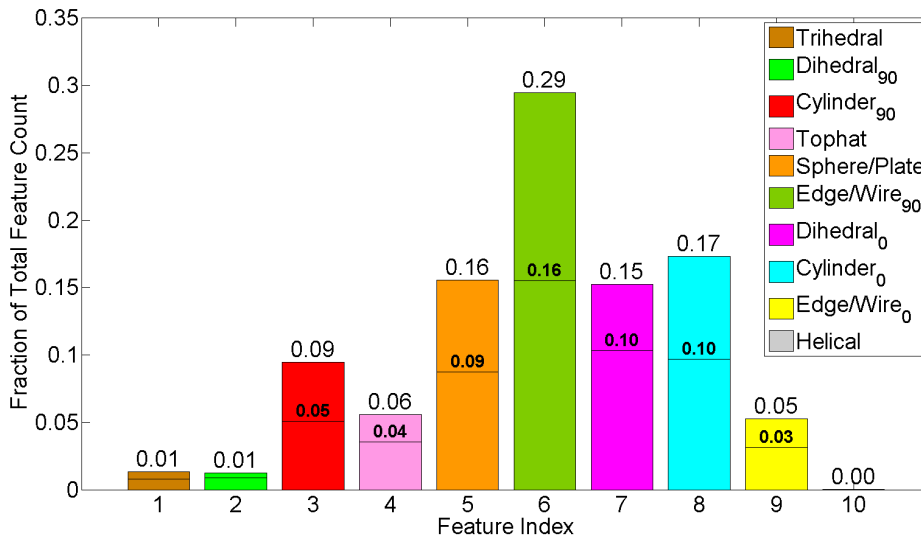
(b) All Extracted HRR Feature Vectors

Figure 4.6: Azimuth angle experiment histograms for HRR FVs (Az 180°). The dividing line illustrated on each canonical feature bar separates FVs according to class origin with sedan FVs below the line and SUV FVs above the line. The value over each dividing line indicates the fraction of only sedan FVs, and the value at the top of each feature bar indicates the fraction of all FVs classified as the specified canonical shape.



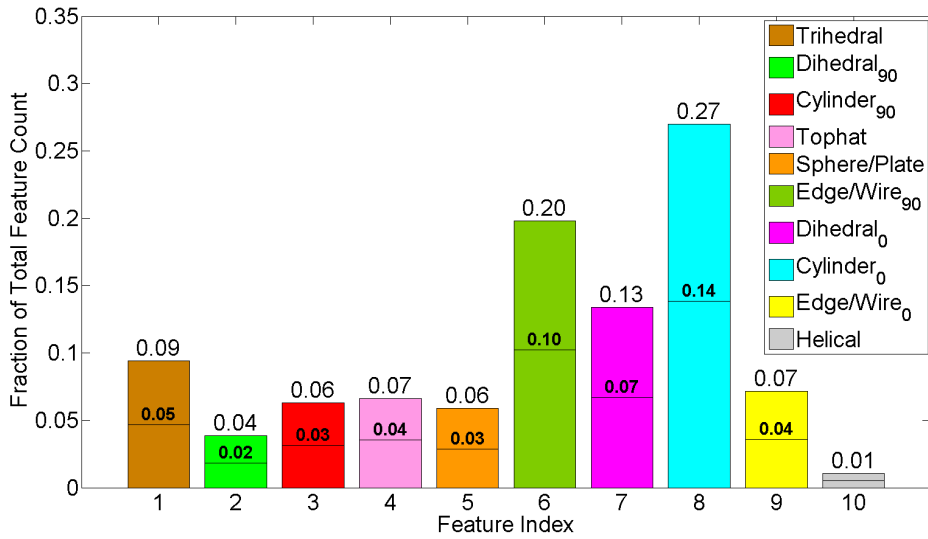


(a) Identified Relevant HRR Feature Vectors Only

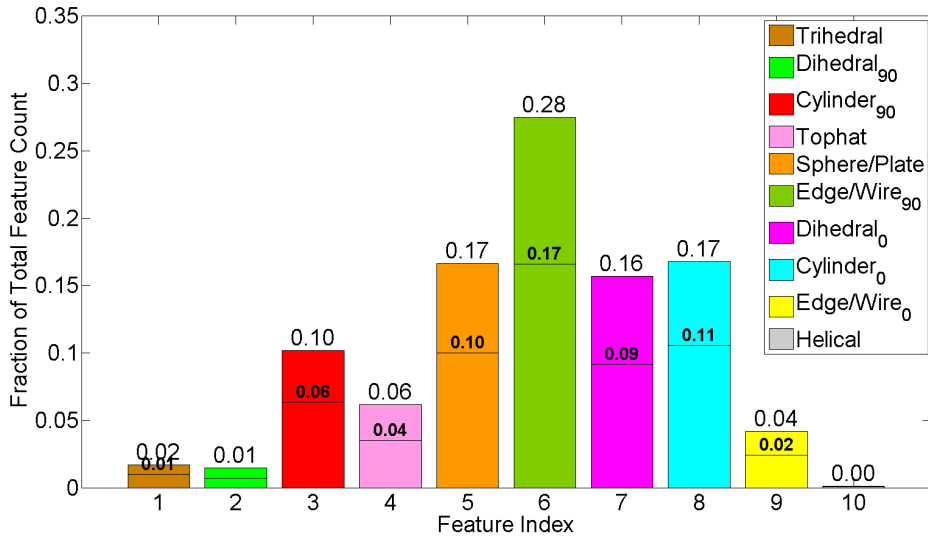


(b) All Extracted HRR Feature Vectors

Figure 4.7: Azimuth angle experiment histograms for HRR FVs ( $Az\ 112.5^\circ$ ). The dividing line illustrated on each canonical feature bar separates FVs according to class origin with sedan FVs below the line and SUV FVs above the line. The value over each dividing line indicates the fraction of only sedan FVs, and the value at the top of each feature bar indicates the fraction of all FVs classified as the specified canonical shape.



(a) Identified Relevant HRR Feature Vectors Only



(b) All Extracted HRR Feature Vectors

Figure 4.8: Azimuth angle experiment histograms for HRR FVs (Az 157.5°). The dividing line illustrated on each canonical feature bar separates FVs according to class origin with sedan FVs below the line and SUV FVs above the line. The value over each dividing line indicates the fraction of only sedan FVs, and the value at the top of each feature bar indicates the fraction of all FVs classified as the specified canonical shape.

#### 4.1.2 Aperture Size Saliency Experiments for HRR Feature Vectors.

The next set of salient HRR feature vector experiments focuses on the effects of aperture size. The three aperture sizes considered for extracted HRR feature vectors are  $3^\circ (\pm 1.5^\circ)$ ,  $5^\circ (\pm 2.5^\circ)$ , and  $10^\circ (\pm 5^\circ)$ . Similar to previous experiments, all other parameters are held constant so that saliency results may be attributed only to aperture size. Elevation remains  $40^\circ$  and azimuth is centered on either  $90^\circ$  or  $180^\circ$  in order to provide two sets of saliency results for aperture size testing. The RBF kernel is implemented into the RVM, and extracted training and test feature data sets are held constant in accordance with Table 3.3.

Table 4.2: Mean results for aperture size experiments 1 – 24 at  $180^\circ$  azimuth,  $40^\circ$  elevation, and 5.35 GHz bandwidth.

Ap Size	# Train/Test	# RVs	% RV	MFW	AFW	$P_e$ %
		Sedan/SUV	Sedan/SUV	Sedan/SUV	Sedan/SUV	Sedan/SUV
$\pm 1.5^\circ$	5156/1234	50.1/49.6	0.97/0.96	112.94/98.54	32.47/30.33	4.03/42.34
$\pm 2.5^\circ$	8511/2063	75.45/75.41	0.88/0.88	143.94/129.40	36.09/34.46	4.85/38.08
$\pm 5^\circ$	16697/4102	132.87/130.25	0.79/0.78	195.47/209.40	38.28/38.49	6.36/39.19

The first set of aperture size experiments are conducted at  $180^\circ$  azimuth with mean results shown in Table 4.2. All individual and experimental results summarized in Table 4.2 are illustrated in Figure 4.9 through Figure 4.12. Figure 4.9 demonstrates that, as expected, increasing aperture size drives an increase in the amount of extracted training and testing HRR feature vectors for RVM classification. The increase in data results in a higher number of identified RVs as shown in Figure 4.10 but a lower proportion of training data being identified as relevant as illustrated in Figure 4.11. While the increase in SAR data for larger aperture sizes incurs an increased computational expense throughout the feature extraction, feature vector creation, and RVM feature vector classification processes, the sparsest RVM

output is generally desired in terms of proportion of identified RVs to total processed data for 10° aperture size as shown in Figure 4.11.

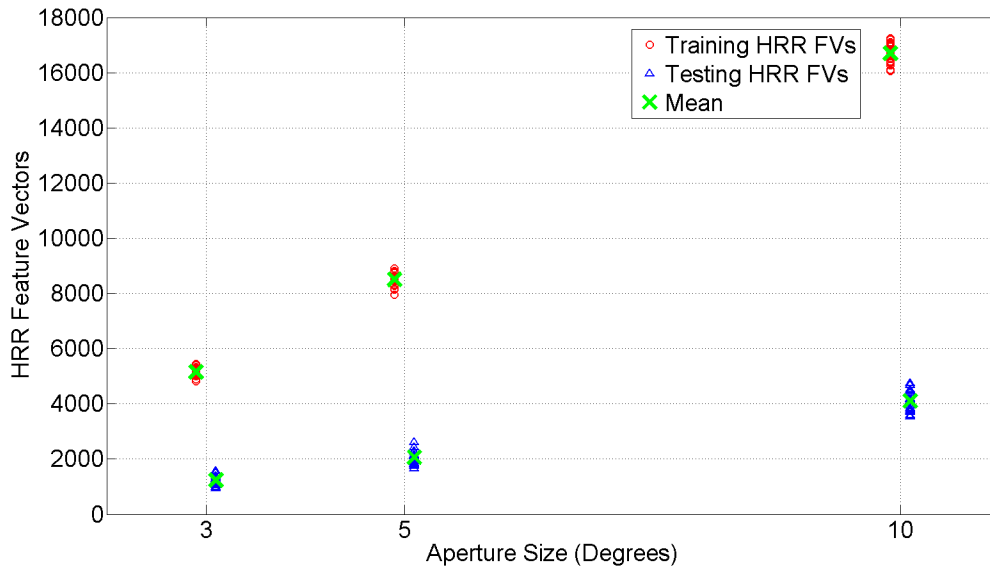


Figure 4.9: Total extracted train and test HRR feature vectors for aperture size experiments at 180° azimuth.

The probability of test classification error results for aperture size experiments at 180° azimuth are shown in Figure 4.12. Results do not demonstrate any significant improvements in  $P_e$  values as aperture size increases, indicating that the computational expense required to process a 10° aperture size may not be justifiable in this case. At the other end of the spectrum, a 3° aperture size is training classes and making classification test decisions from a much smaller set of HRR feature vectors, making it vulnerable to large increases or decreases in classification error from potential anomalies in the SAR data within such a limited aperture. Therefore, a 5° aperture size is recommended, but a

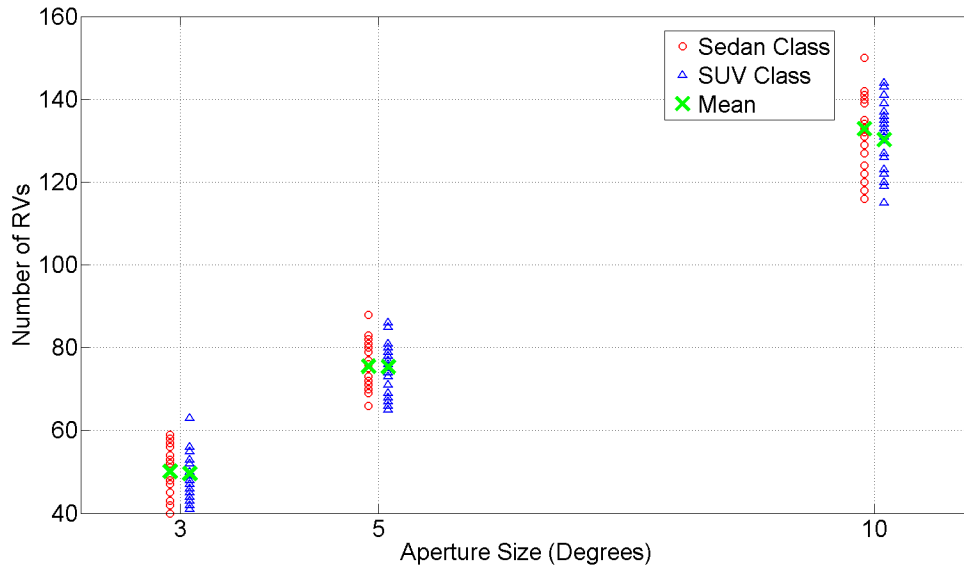


Figure 4.10: Total identified relevant HRR feature vectors for aperture size experiments at 180° azimuth.

second set of aperture size test results is later provided at 90° azimuth to verify the initial results observed.

Histograms of the identified RVs classified into the physical target features which aid most in the RVM classification process for 3° and 10° aperture sizes are shown in Figure 4.13a and Figure 4.14a respectively. The 5° aperture size histograms for 180° azimuth were previously illustrated in Figure 4.6. While all three aperture sizes feature horizontal cylinders as the most impactful physical target feature, some vehicle features prove more impactful than others as aperture size varies. For example, the 3° aperture size demonstrates less target class identification dependence on the horizontal dihedral but slightly more dependence on the trihedral and vertical cylinder features. With such a narrow focus on the rear aspect of the vehicles at a 3° aperture size, features common across all vehicles at 180° azimuth, such as horizontal dihedrals, are deemed less relevant by the RVM

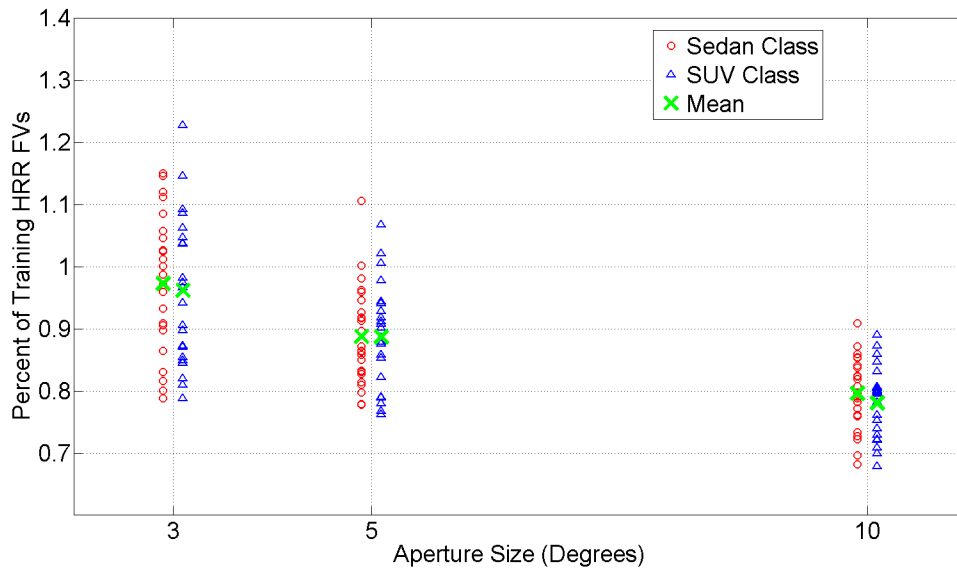


Figure 4.11: Percent of training HRR feature vectors deemed relevant for aperture size experiments at 180° azimuth.

classifier with a limited data set, while more unique target features, such as trihedrals, tend to stand out in the feature vector weighting process. As aperture size grows further from the specular, however, horizontal dihedral feature vectors gain relevance in comparisons between sedan and SUV class vehicles as shown for 5° and 10° aperture sizes.

A second set of aperture size experiments are conducted at 90° azimuth with all other parameters held constant in accordance with Table 3.4. The mean results for the second set of aperture size tests are featured in Table 4.3, and individual test results are illustrated in Figure 4.15 through Figure 4.18. Extracted training and testing HRR feature vector totals in Figure 4.15, RV totals in Figure 4.16, and percentage of training HRR feature vectors deemed relevant in Figure 4.17 are all consistent with the previously discussed aperture size results at 180° azimuth. Based on the 90° azimuth results, the 10° aperture size is preferred due to the sparsity with which the two large SAR training data sets are able to

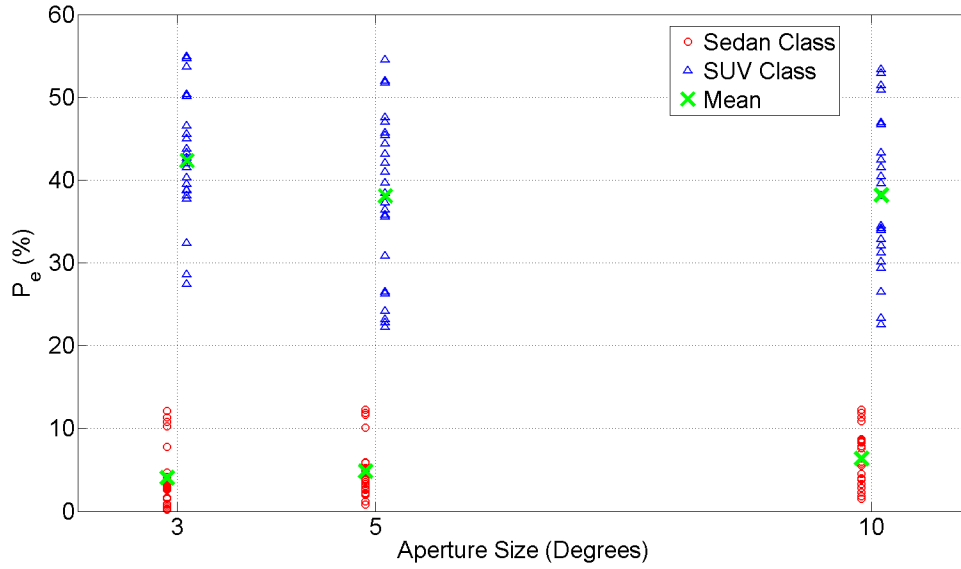


Figure 4.12: Probability of RVM classification error for extracted HRR feature vectors as seen throughout aperture size experiments at  $180^\circ$  azimuth.

be separated in the transformed kernel space. Since a  $10^\circ$  aperture size requires increased computational expense, however,  $P_e$  results assist in determining the overall aperture size saliency recommendation for  $90^\circ$  azimuth.

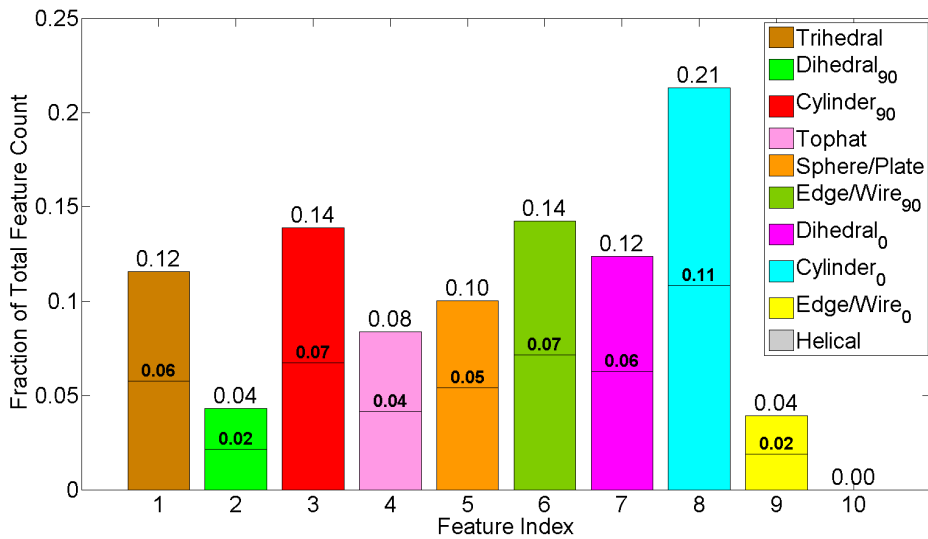
Table 4.3: Mean results for aperture size experiments 1 – 24 at  $90^\circ$  azimuth,  $40^\circ$  elevation, and 5.35 GHz bandwidth.

Ap Size	# Train/Test	# RVs	% RV	MFW	AFW	$P_e$ %
		Sedan/SUV	Sedan/SUV	Sedan/SUV	Sedan/SUV	Sedan/SUV
$\pm 1.5^\circ$	3733/962	44.79/43.66	1.20/1.17	380.92/382.40	94.35/93.93	5.17/29.83
$\pm 2.5^\circ$	6413/1642	61.79/60.79	0.96/0.94	409.87/430.98	84.82/83.83	4.42/31.23
$\pm 5^\circ$	14138/3596	114.29/114.29	0.80/0.80	469.70/431.57	79.37/77.79	4.44/29.78

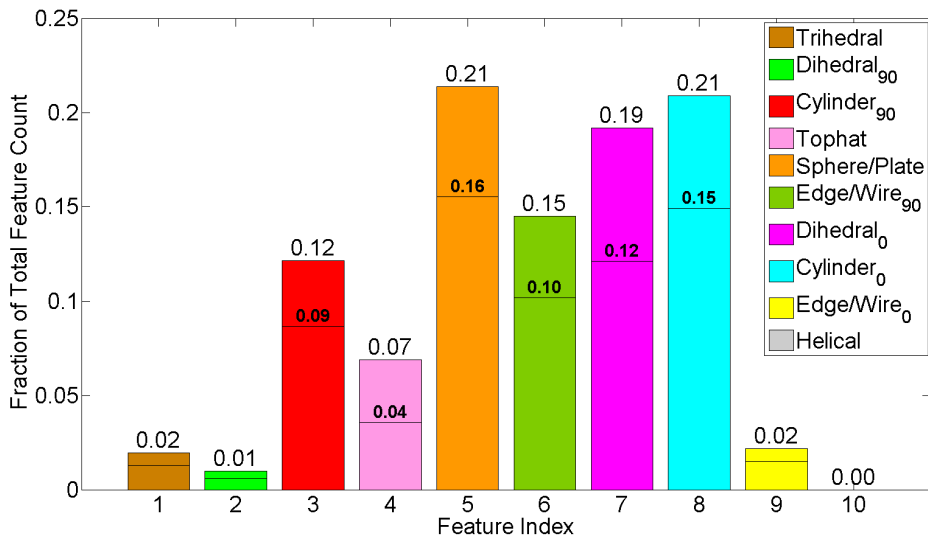
Probability of test classification error results are illustrated in Figure 4.18. Similar to aperture size testing at 180° azimuth, no significant improvement in classification error is achieved by increasing aperture. One exception seen in Figure 4.18 is that the individual experiments with the highest  $P_e$  values, those greater than 50% in the 3° and 5° aperture sizes, fell to less than 50% in the 10° aperture case. The modest improvement in  $P_e$  outlier values, however, is not enough to justify the increased resources required for a 10° SAR collection aperture. It should be noted that the six individual experiments with the highest  $P_e$  values in all three aperture sizes correspond to the Toyota Tacoma as the test vehicle. The poor classification results therefore have more to do with increased separation in the relationship between training and test feature vector data than with the aperture sizes being investigated for salience. While the 3° and 5° aperture sizes achieved similar  $P_e$  results, an aperture size of 5° includes a slightly larger, and therefore more target class representative set of extracted HRR feature vectors for classification. Consistent with aperture size experiments conducted at 180° azimuth, an aperture size of 5° is recommended for improving ATR classification potential at 90° azimuth between sedan and SUV class vehicles.

Target feature histograms for 3° and 10° aperture sizes at 90° azimuth are shown in Figure 4.19 and Figure 4.20, respectively. The 5° aperture size histograms for 90° azimuth were previously illustrated in Figure 4.5. While the total number of relevant feature vectors being classified increases as aperture size grows, the target feature index rankings remain fairly constant. The top five relevant canonical shapes are in the same order of importance for all three aperture sizes tested. This result indicates that increasing aperture size from 3° to 10° does not provide additional salient target feature information at 90° azimuth. At the 90° spectral azimuth, horizontal cylinders, primarily stemming from the roof line of the vehicles, and horizontal dihedrals, formed between the flat surfaces of vehicle doors and the ground plane, should be provided the most attention for target class identification.



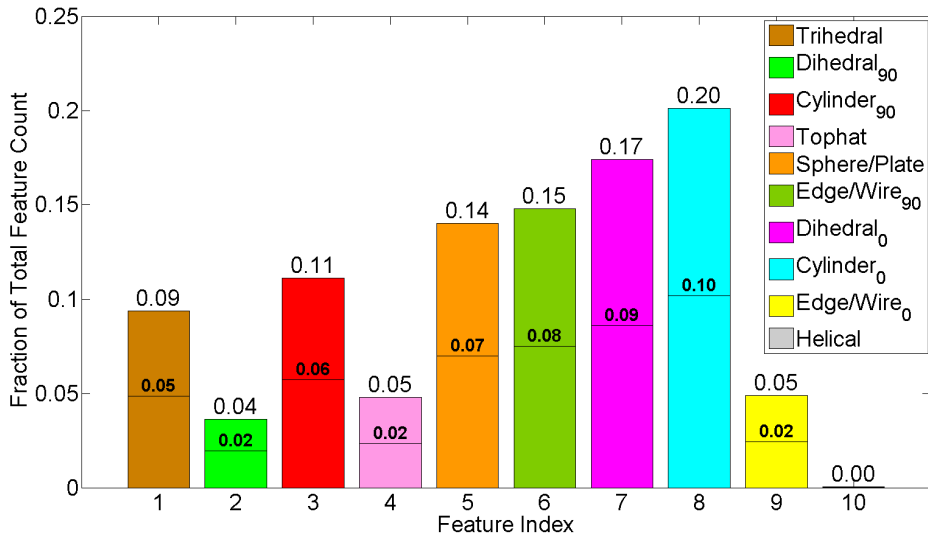


(a) Identified Relevant HRR Feature Vectors Only

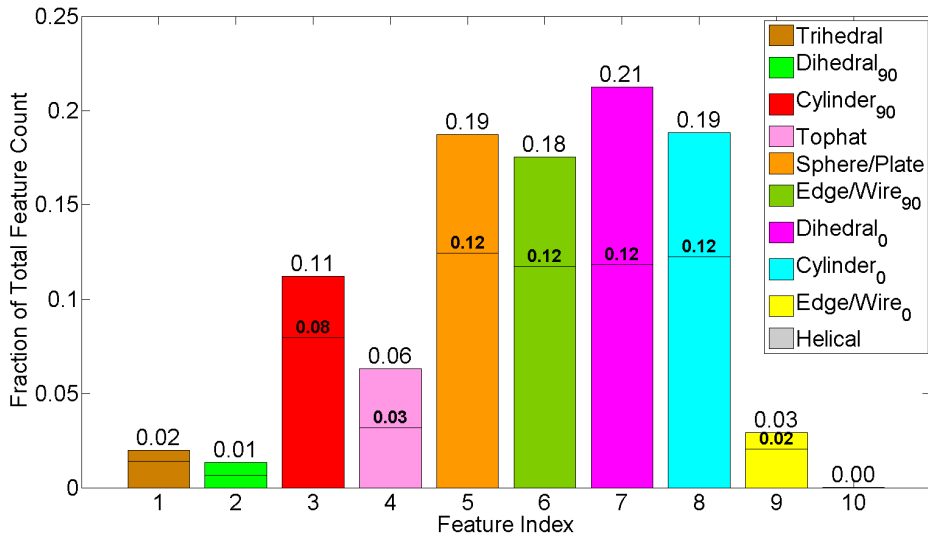


(b) All Extracted HRR Feature Vectors

Figure 4.13: Aperture size experiment histograms for HRR FVs ( $A_p$  size  $3^\circ$ ,  $A_z$   $180^\circ$ ). The dividing line illustrated on each canonical feature bar separates FVs according to class origin with sedan FVs below the line and SUV FVs above the line. The value over each dividing line indicates the fraction of only sedan FVs, and the value at the top of each feature bar indicates the fraction of all FVs classified as the specified canonical shape.



(a) Identified Relevant HRR Feature Vectors Only



(b) All Extracted HRR Feature Vectors

Figure 4.14: Aperture size experiment histograms for HRR FVs ( $A_p$  size  $10^\circ$ ,  $A_z$   $180^\circ$ ). The dividing line illustrated on each canonical feature bar separates FVs according to class origin with sedan FVs below the line and SUV FVs above the line. The value over each dividing line indicates the fraction of only sedan FVs, and the value at the top of each feature bar indicates the fraction of all FVs classified as the specified canonical shape.

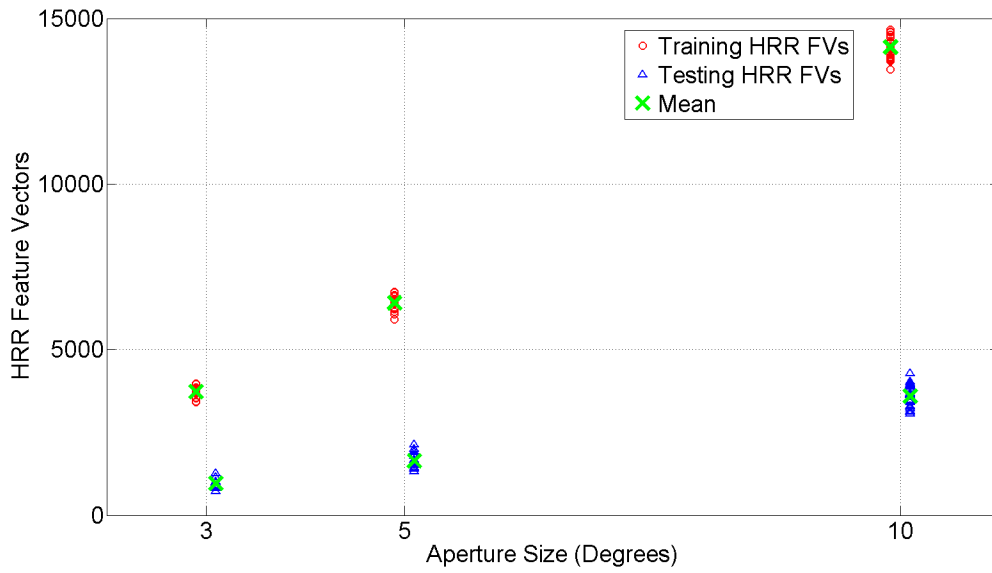


Figure 4.15: Total extracted train and test HRR feature vectors for aperture size experiments at 90° azimuth.

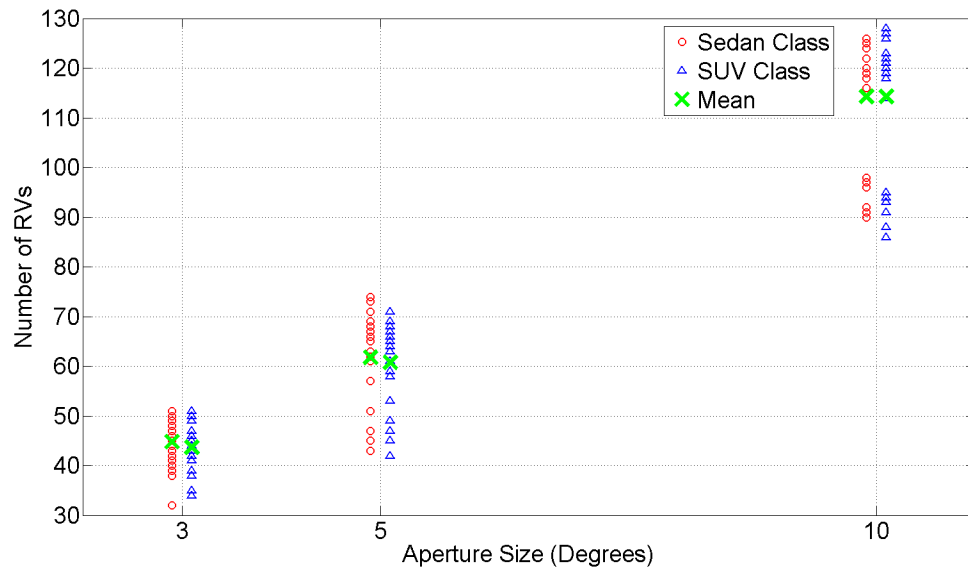


Figure 4.16: Total identified relevant HRR feature vectors for aperture size experiments at 90° azimuth.

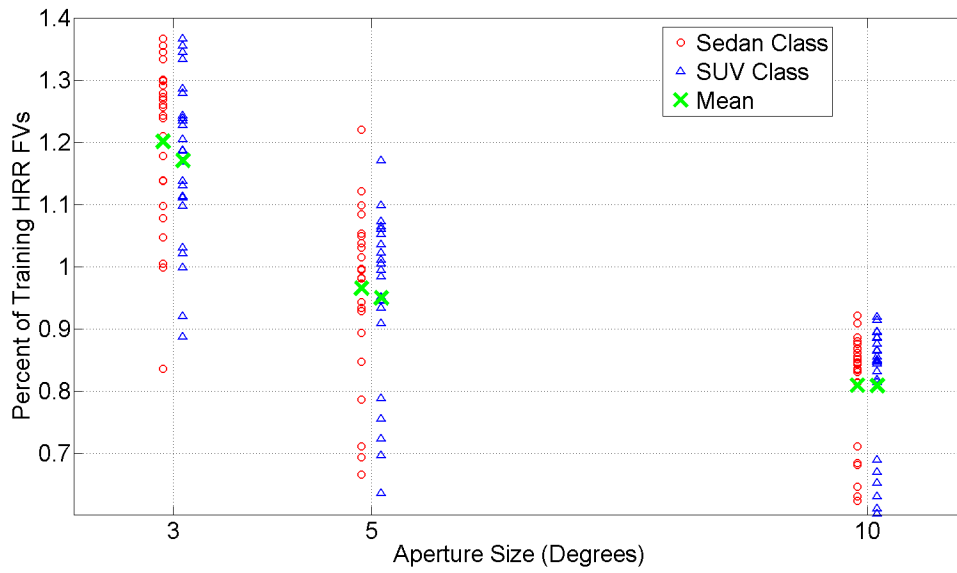


Figure 4.17: Percent of training HRR feature vectors deemed relevant for aperture size experiments at 90° azimuth.

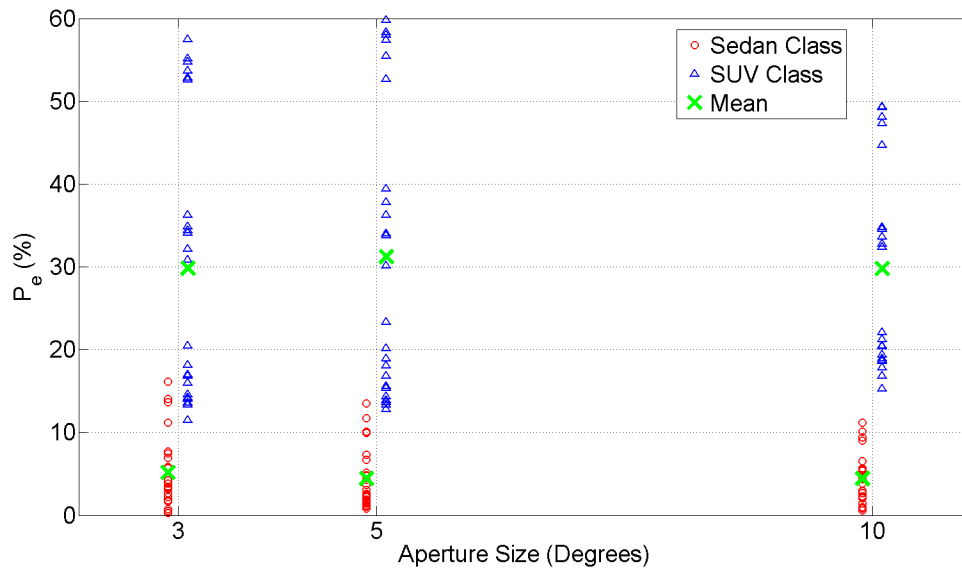
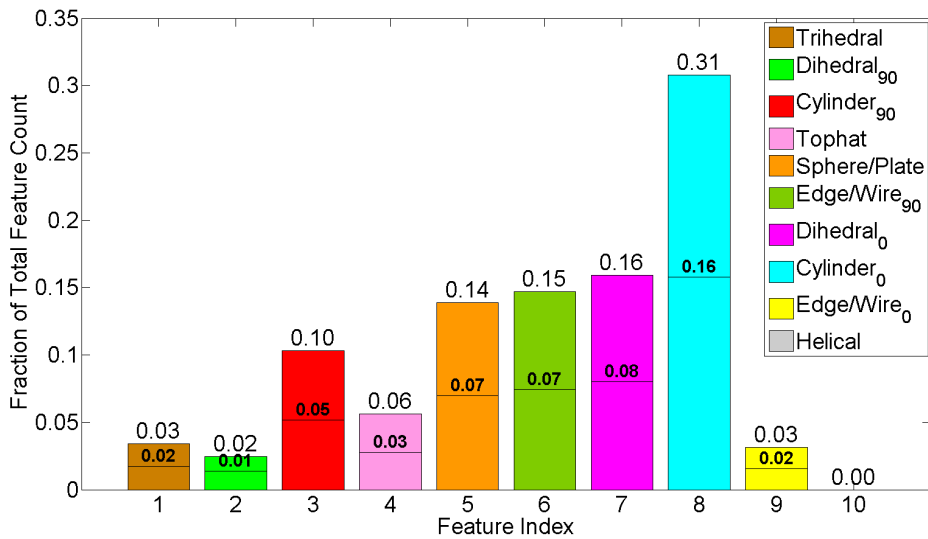
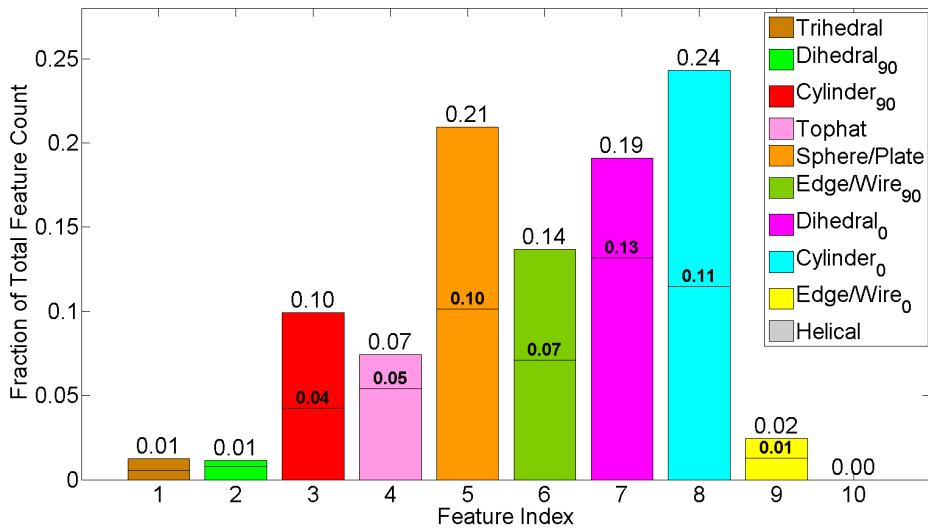


Figure 4.18: Probability of RVM classification error for extracted HRR feature vectors as seen throughout aperture size experiments at 90° azimuth.

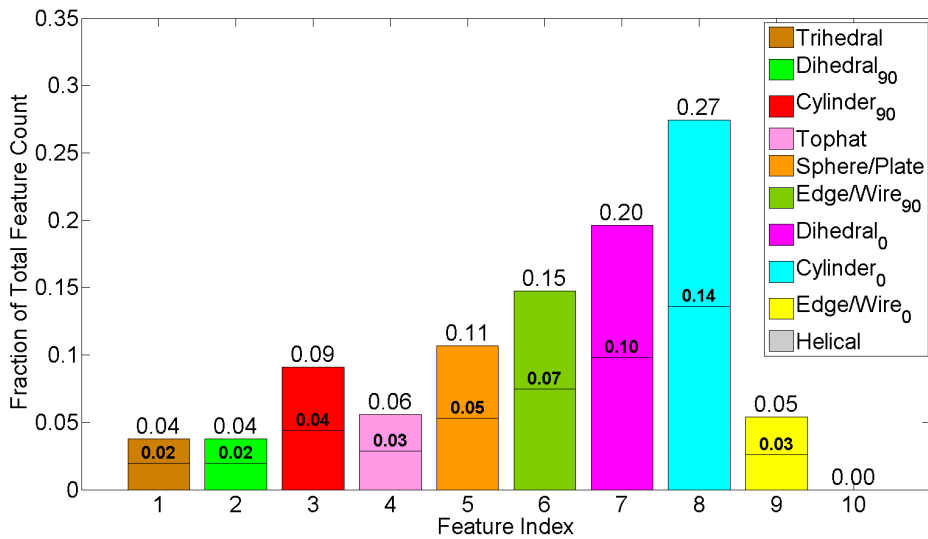


(a) Identified Relevant HRR Feature Vectors Only

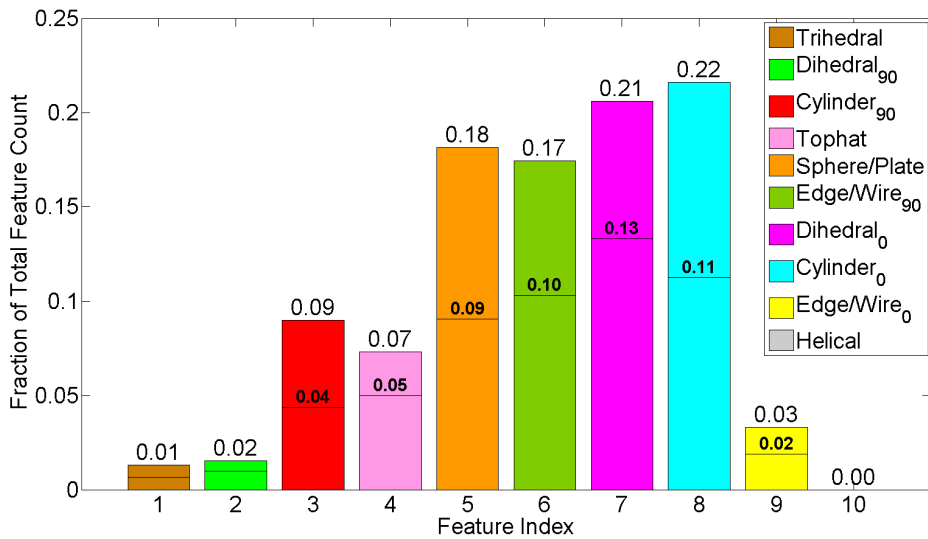


(b) All Extracted HRR Feature Vectors

Figure 4.19: Aperture size experiment histograms for HRR FVs ( $A_p$  size  $3^\circ$ ,  $A_z$   $90^\circ$ ). The dividing line illustrated on each canonical feature bar separates FVs according to class origin with sedan FVs below the line and SUV FVs above the line. The value over each dividing line indicates the fraction of only sedan FVs, and the value at the top of each feature bar indicates the fraction of all FVs classified as the specified canonical shape.



(a) Identified Relevant HRR Feature Vectors Only



(b) All Extracted HRR Feature Vectors

Figure 4.20: Aperture size experiment histograms for HRR FVs ( $A_p$  size  $10^\circ$ ,  $A_z$   $90^\circ$ ). The dividing line illustrated on each canonical feature bar separates FVs according to class origin with sedan FVs below the line and SUV FVs above the line. The value over each dividing line indicates the fraction of only sedan FVs, and the value at the top of each feature bar indicates the fraction of all FVs classified as the specified canonical shape.

### 4.1.3 Elevation Angle Saliency Experiments for HRR Feature Vectors.

The effects of elevation angle on saliency and target class identification are tested using three realistic flight path elevation angles: 30°, 40°, and 50°. All experiments are conducted with all available bandwidth (5.35 GHz) and a 5° aperture size at two separate azimuths, 90° and 180°. The same 24 original experiments in Table 3.3 are tested once again for consistency. A summary of all elevation test results at 180° azimuth are shown in Table 4.4.

Table 4.4: Mean results for elevation angle experiments 1 – 24 at 180° azimuth,  $\pm 2.5^\circ$  aperture size, and 5.35 GHz bandwidth.

El	# Train/Test	# RVs		% RV		MFW		AFW		$P_e$ %	
		Sedan/SUV	Sedan/SUV	Sedan/SUV	Sedan/SUV	Sedan/SUV	Sedan/SUV	Sedan/SUV	Sedan/SUV		
30°	7894/1921	62.3/61.2	0.79/0.77	110.60/109.31	28.92/27.77	1.85/43.63					
40°	8511/2063	75.45/75.41	0.88/0.88	143.94/129.40	36.09/34.46	4.86/38.08					
50°	8904/2231	70.6/71.9	0.79/0.80	155.45/152.06	41.04/40.26	5.51/35.27					

The total number of extracted training and testing HRR feature vectors are illustrated in Figure 4.21. Unlike the azimuth and aperture size experiments, the elevation experiments are conducted at the same azimuth with the same aperture size, so the size of the extracted feature vector data sets are relatively close. Observe in Figure 4.21, however, that the amount of training and testing data for RVM classification gradually rises as elevation moves from 30° to 50°, demonstrating that a steeper elevation angle reveals more target surface to the radar for the CV data domes targets with extracted HRR feature vectors. The total number of RVs output by the RVM is shown in Figure 4.22 and the ratio of RVs to training feature vectors is shown in Figure 4.23. In both figures, notice the increased spread in standard deviation of results at 30° elevation compared to 40° and 50°. In Figure 4.23, for example, the standard deviation across all 24 experiments is 0.162 for the sedan class

and 0.160 for the SUV class at 30°, compared to 0.078/0.082 (sedan/SUV) at 40° and 0.092/0.083 (sedan/SUV) at 50°. The mean values in Figure 4.23 are fairly similar between 30° and 50°, so we move to  $P_e$  results for further analysis of elevation angle saliency.

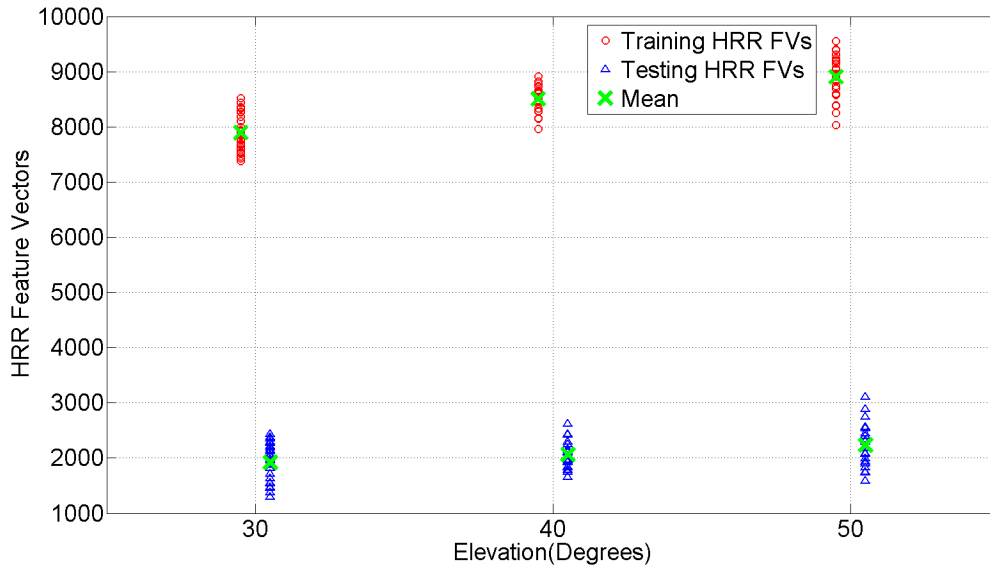


Figure 4.21: Total extracted train and test HRR feature vectors for elevation angle experiments at 180° azimuth.

Probability of RVM classification error results for elevation tests at 180° azimuth are shown in Figure 4.24. Results show that 30° elevation achieved the lowest average  $P_e$  for sedan tests, while 50° elevation had the lowest mean classification error for SUV tests. None of the elevation angles at 180° azimuth demonstrated clear saliency worthy of being recommended for improving SAR binary classification performance. Therefore, elevation experiments are also conducted at 90° azimuth for further investigation into elevation angle saliency.



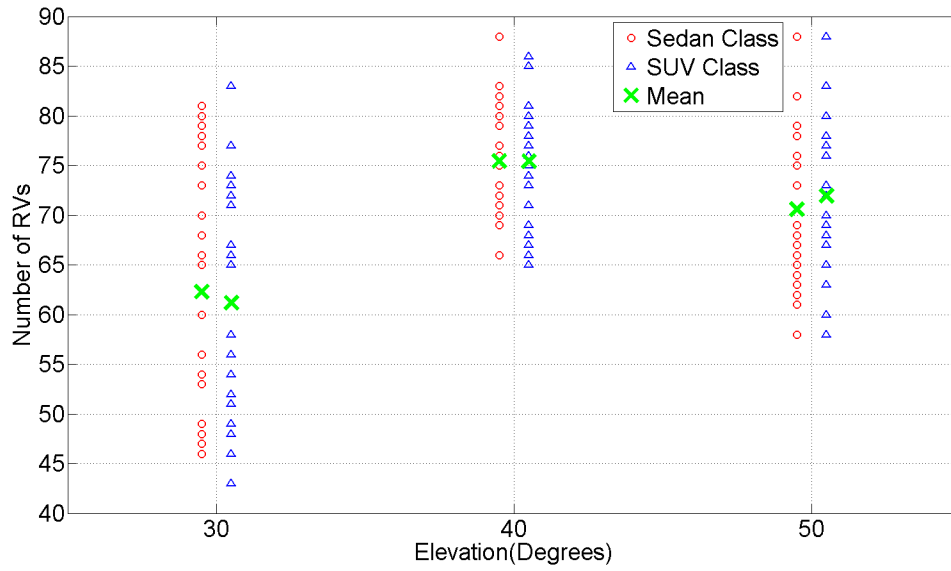


Figure 4.22: Total identified relevant HRR feature vectors for elevation angle experiments at 180° azimuth.

Salient target feature histograms are illustrated for elevations 30° and 50° at 180° azimuth in Figure 4.25 and Figure 4.26, respectively. The histograms for 40° elevation were previously shown in Figure 4.6. Observe that with azimuth angle, aperture size, and bandwidth all held constant, the change in elevation angle alone presents new relevant target features to the radar. While the most relevant shapes for classification are similar for elevations 40° and 50°, elevation 30° demonstrates an increased dependence on vertical edges and vertical cylinders for classification decisions. This information may be useful in characterizing elevation saliency. Elevations 40° and 50° present a steeper, more top-down view of the vehicles, emphasizing the significance of the horizontal cylinders making up the roof lines and the horizontal dihedrals formed with the speculars of the vehicle and the ground plane. Since horizontal cylinders and dihedrals are two primary target features common in all vehicles, however, potential complications may arise in vehicle classifications at steeper azimuths. While horizontal cylinders and dihedrals remain

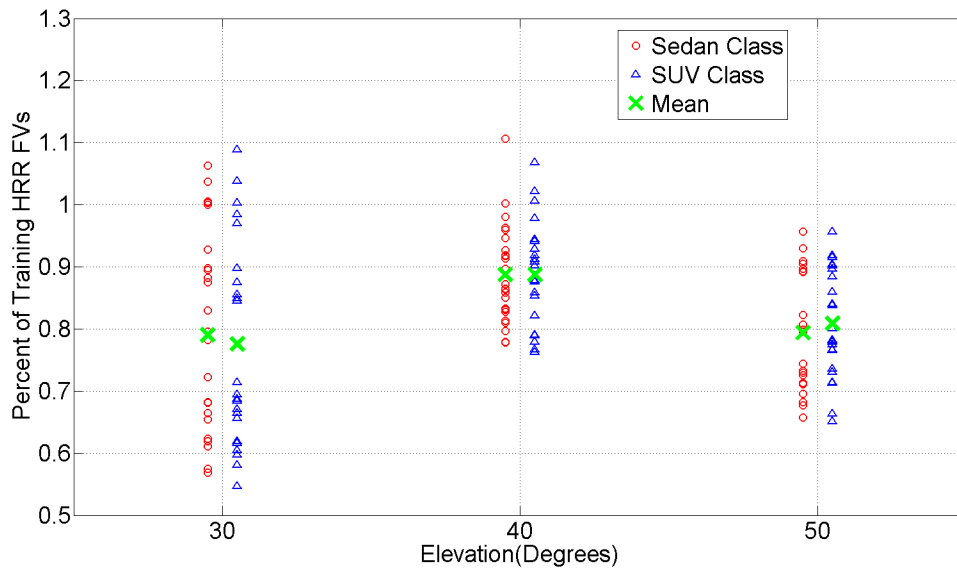


Figure 4.23: Percent of training HRR feature vectors deemed relevant for elevation angle experiments at 180° azimuth.

relevant target features for 30° elevation, additional features gain relevance that may prove valuable in vehicle classification decisions. The roofs of civilian vehicles are all relatively similar, but the bodies of the vehicles below the roof lines contain many identifying physical features separating one vehicle from another. Highlighting the distinct body style features at lower elevation angles may allow for increased separability among extracted feature vectors and serve to improve vehicle classifications for application to ATR.

Another set of elevation angle experiments is conducted at 90° azimuth with mean results shown in Table 4.5. In addition, the total amount of extracted HRR feature vectors for training and testing, total number of RVs, and percent of training HRR feature vectors deemed relevant are illustrated in Figure 4.27, Figure 4.28, and Figure 4.29, respectively. Similar to 180° azimuth, 30° elevation produces slightly less extracted feature vectors for classification than 40° and 50° elevations, but overall the size of the SAR data sets are

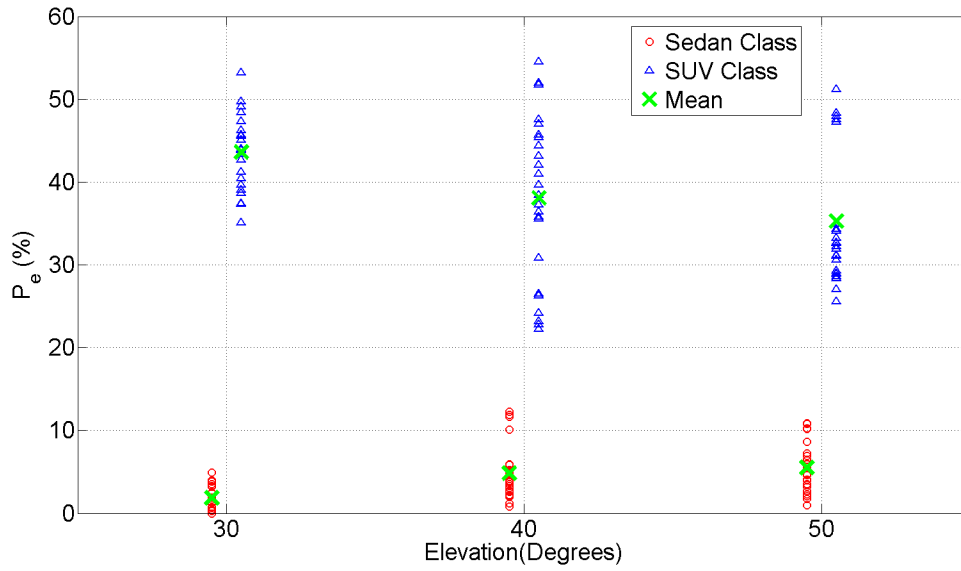


Figure 4.24: Probability of RVM classification error for extracted HRR feature vectors as seen throughout elevation angle experiments at 180° azimuth.

relatively close for all three elevation angles tested. In Figure 4.28 and Figure 4.29, notice that 50° elevation identifies fewer RVs on average than do 30° and 40° elevations, producing a more desired RVM output by both representing and separating the sedan and SUV classes with a more sparse set of HRR feature vectors.

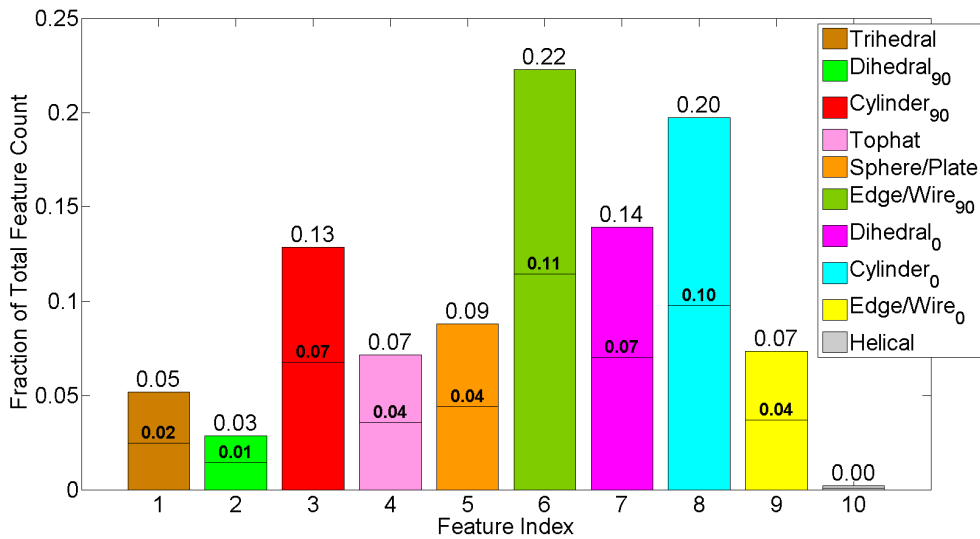
Table 4.5: Mean results for elevation angle experiments 1 – 24 at 90° azimuth, ±2.5° aperture size, and 5.35 GHz bandwidth.

El	# Train/Test	# RVs	% RV	MFW	AFW	$P_e$ %
		Sedan/SUV	Sedan/SUV	Sedan/SUV	Sedan/SUV	Sedan/SUV
30°	5754/1532	59.29/59.70	1.03/1.03	429.10/399.04	87.29/90.21	5.65/16.04
40°	6413/1642	61.79/60.79	0.96/0.94	409.87/430.98	84.82/83.83	4.41/31.24
50°	6194/1678	49.45/50.25	0.79/0.81	227.41/228.60	51.71/52.66	10.94/20.14

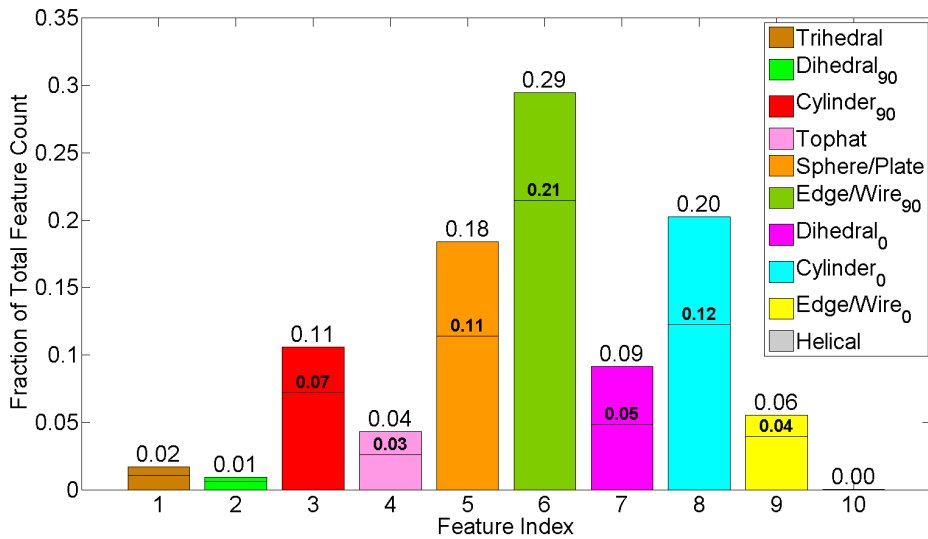
Referring now to the probability of classification error values in Figure 4.30, 30° elevation significantly outperformed 40° and 50° elevations overall. Additionally, 30° elevation experiments demonstrated no poor classification test outliers as seen in the other two elevations at 90° azimuth. All classification error values greater than 40% in 40° and 50° elevations were a result of the Toyota Tacoma truck being tested, but the same Tacoma tests at 30° elevation produced RVM classification errors just over 20%.

All extracted and relevant HRR feature vectors classified into physical canonical shapes and ranked as histograms are shown for 90° azimuth in Figure 4.31, Figure 4.5, and Figure 4.32, for elevations 30°, 40°, and 50°, respectively. Results remained consistent with the relevant target features discussed for 180° azimuth in that 40° and 50° elevations demonstrated similar feature rankings while 30° elevation highlighted many additional unique target features as relevant to classification decisions. The increase in distinct target features at 30° elevation is a benefit to vehicle classification performance, as it allows more opportunity for separation of sedan and SUV class HRR feature vectors. This assertion is supported by the improvement in  $P_e$  at 30° elevation shown in Figure 4.30.

Considering all aspects of the brief investigation into the nature of elevation angle saliency for extracted HRR feature vectors, 30° is the recommended elevation angle for maximizing potential vehicle classification performance. The recommendation, however, applies only to our specific set of experiments with the chosen parameters and the AFRL CV domes SAR data set. The process implemented here may be applied to new classes of SAR data to characterize elevation angle salience, but the results will be specific to the experiments, parameters, and data chosen for that particular salient feature analysis.

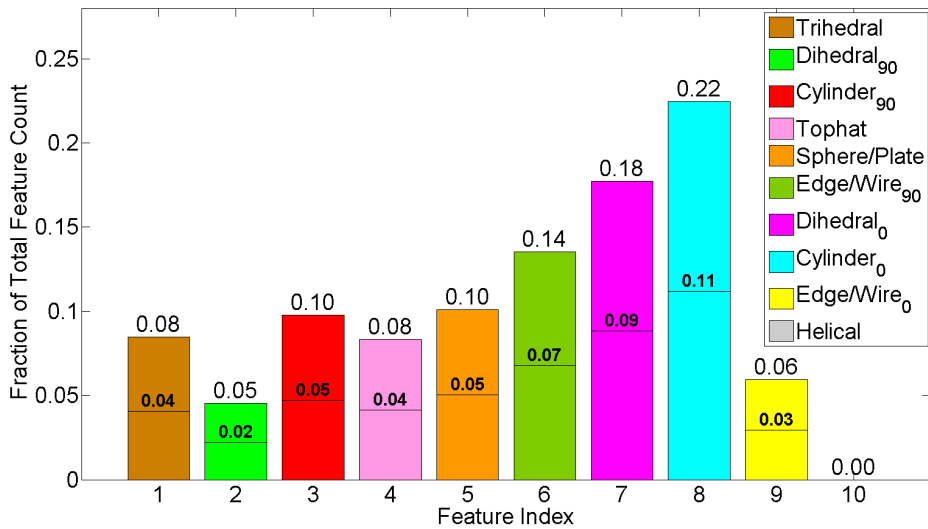


(a) Identified Relevant HRR Feature Vectors Only

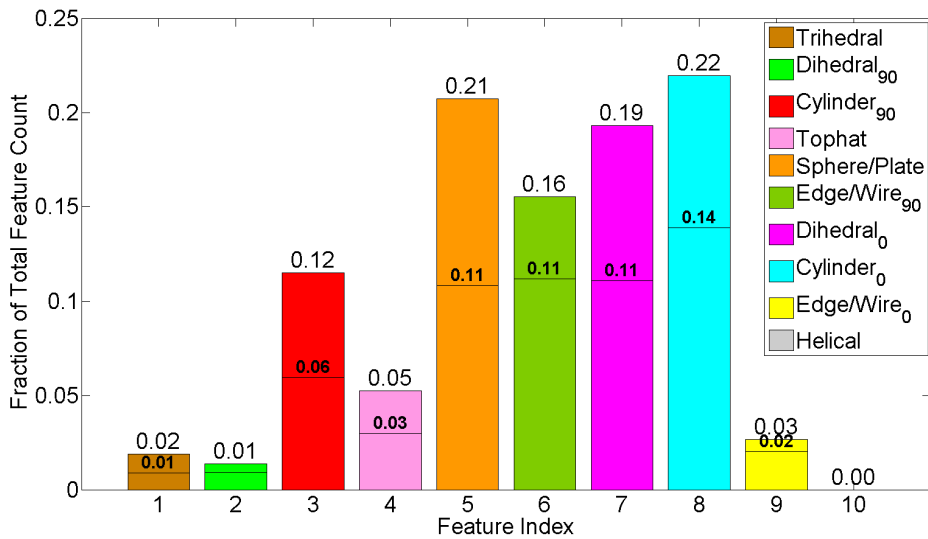


(b) All Extracted HRR Feature Vectors

Figure 4.25: Elevation angle experiment histograms for HRR FVs (El 30°, Az 180°). The dividing line illustrated on each canonical feature bar separates FVs according to class origin with sedan FVs below the line and SUV FVs above the line. The value over each dividing line indicates the fraction of only sedan FVs, and the value at the top of each feature bar indicates the fraction of all FVs classified as the specified canonical shape.



(a) Identified Relevant HRR Feature Vectors Only



(b) All Extracted HRR Feature Vectors

Figure 4.26: Elevation angle experiment histograms for HRR FVs (El 50°, Az 180°). The dividing line illustrated on each canonical feature bar separates FVs according to class origin with sedan FVs below the line and SUV FVs above the line. The value over each dividing line indicates the fraction of only sedan FVs, and the value at the top of each feature bar indicates the fraction of all FVs classified as the specified canonical shape.

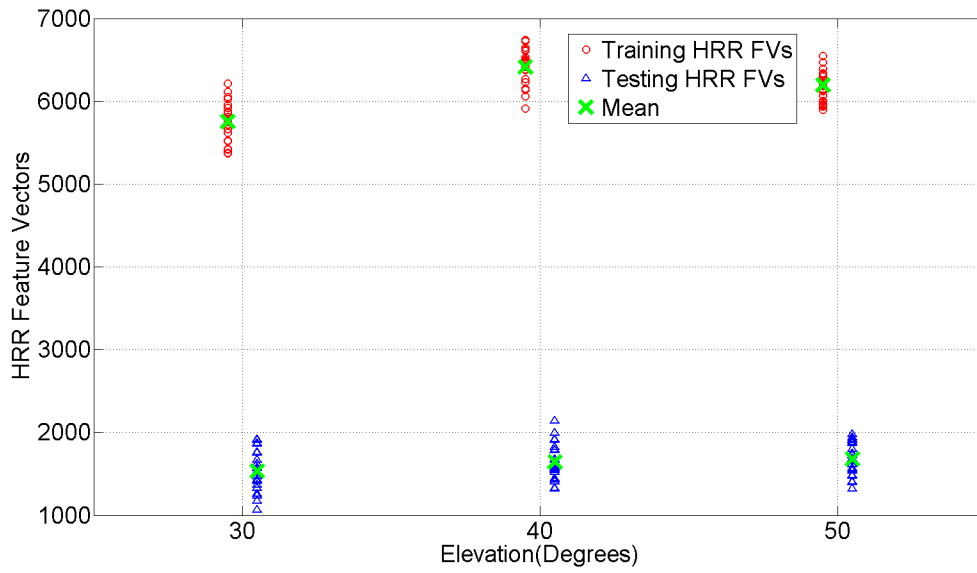


Figure 4.27: Total extracted train and test HRR feature vectors for elevation angle experiments at 90° azimuth.

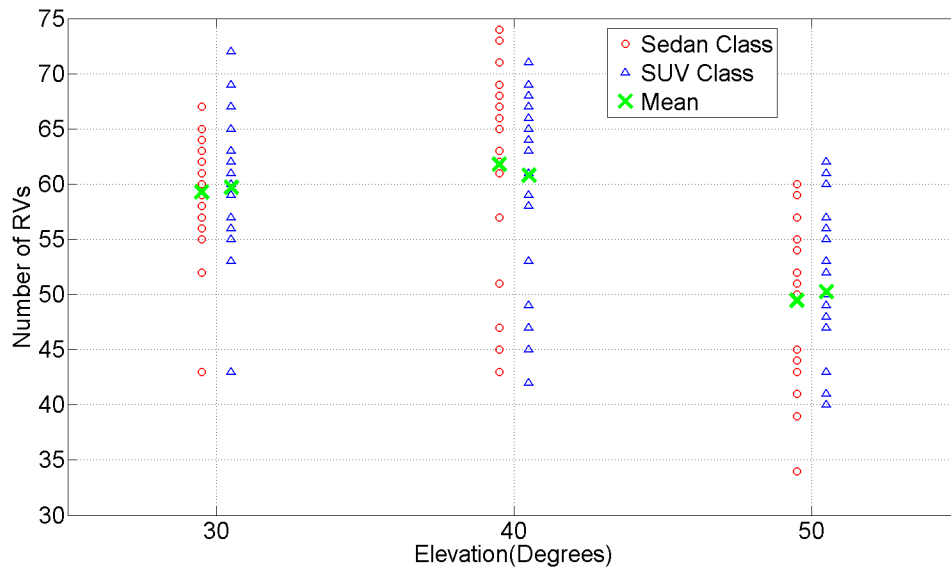


Figure 4.28: Total identified relevant HRR feature vectors for elevation angle experiments at 90° azimuth.

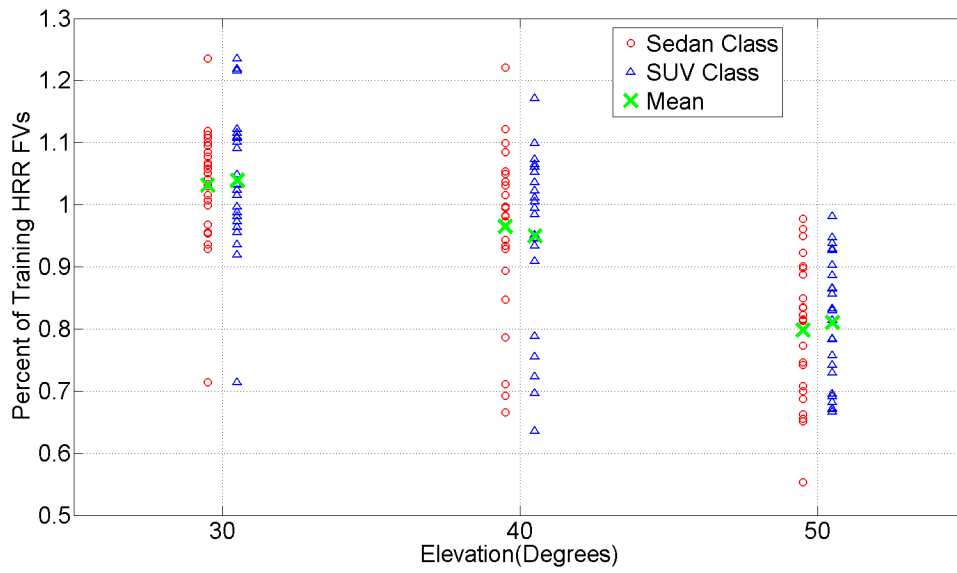


Figure 4.29: Percent of training HRR feature vectors deemed relevant for elevation angle experiments at 90° azimuth.

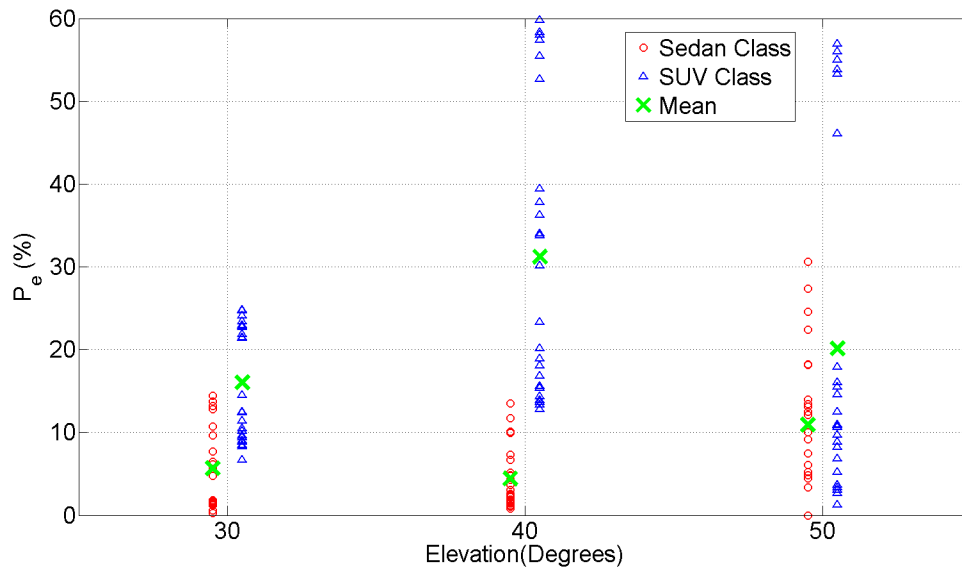
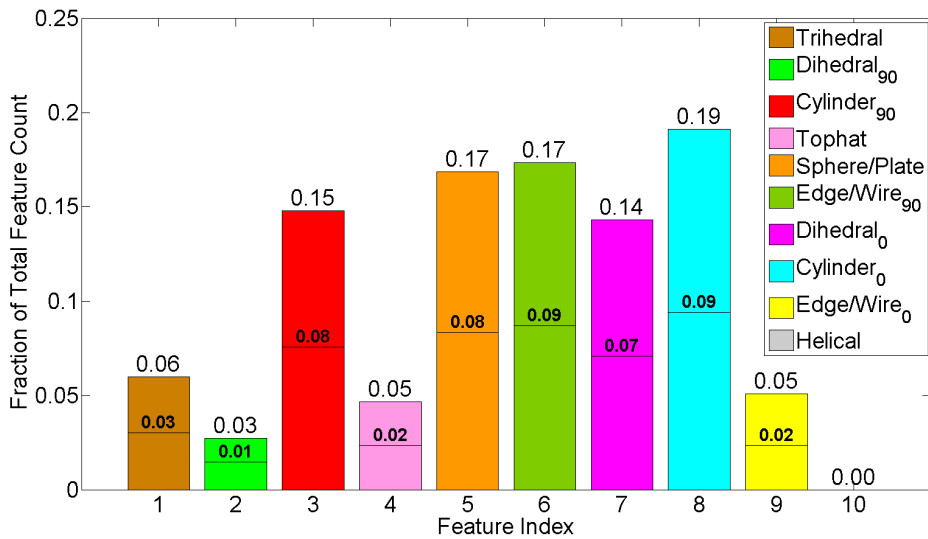
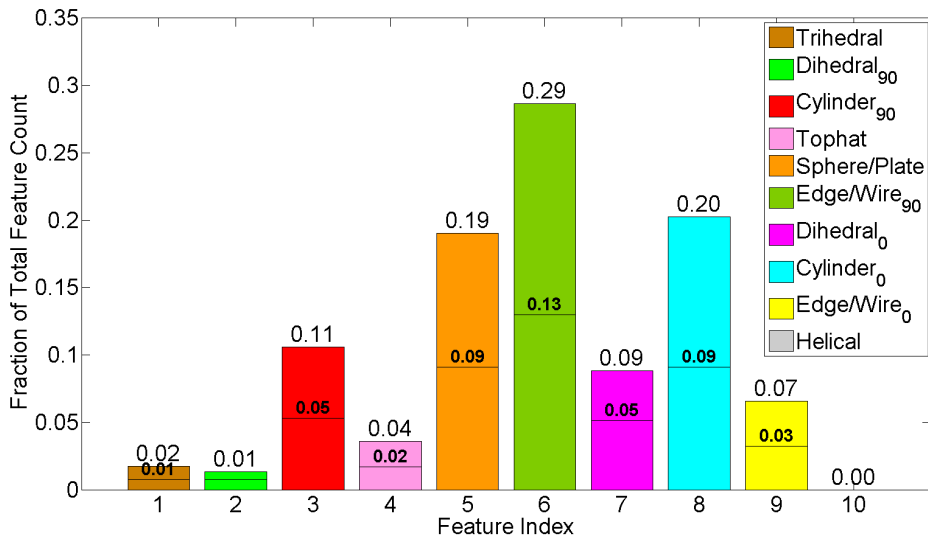


Figure 4.30: Probability of RVM classification error for extracted HRR feature vectors as seen throughout elevation experiments at 90° azimuth.



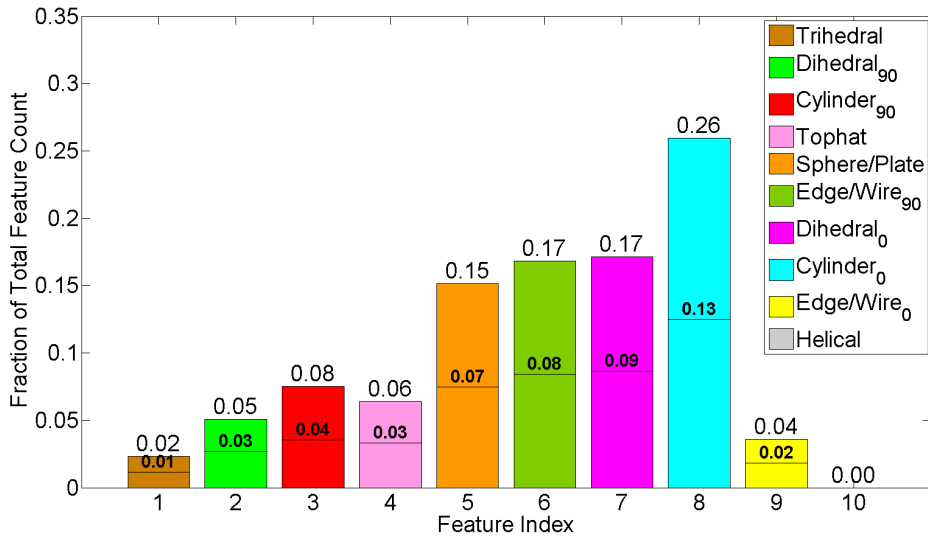


(a) Identified Relevant HRR Feature Vectors Only

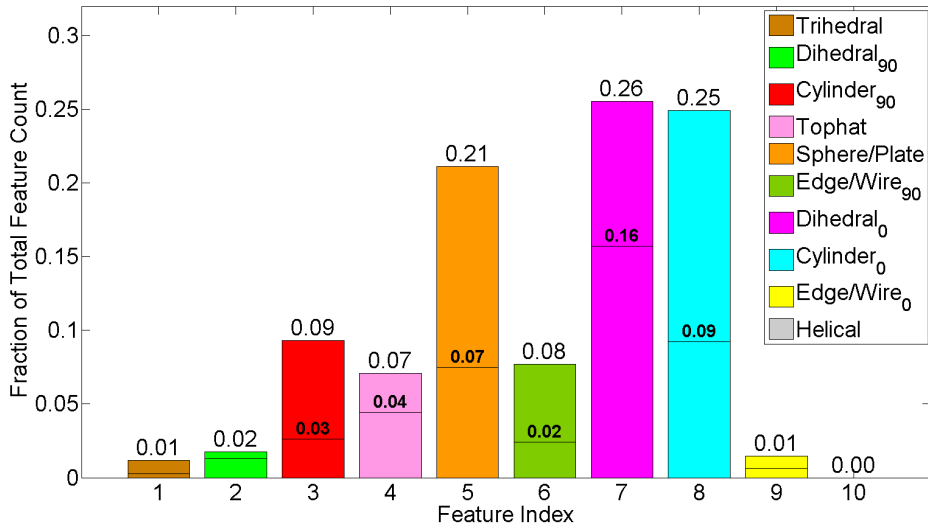


(b) All Extracted HRR Feature Vectors

Figure 4.31: Elevation angle experiment histograms for HRR FVs (El 30°, Az 90°). The dividing line illustrated on each canonical feature bar separates FVs according to class origin with sedan FVs below the line and SUV FVs above the line. The value over each dividing line indicates the fraction of only sedan FVs, and the value at the top of each feature bar indicates the fraction of all FVs classified as the specified canonical shape.



(a) Identified Relevant HRR Feature Vectors Only



(b) All Extracted HRR Feature Vectors

Figure 4.32: Elevation angle experiment histograms for HRR FVs (El 50°, Az 90°). The dividing line illustrated on each canonical feature bar separates FVs according to class origin with sedan FVs below the line and SUV FVs above the line. The value over each dividing line indicates the fraction of only sedan FVs, and the value at the top of each feature bar indicates the fraction of all FVs classified as the specified canonical shape.

#### 4.1.4 Bandwidth Saliency Experiments for HRR Feature Vectors.

The final SAR collection parameter investigated for saliency of extracted HRR feature vectors is bandwidth. The effects of bandwidth on classification performance are observed for three possible bandwidths. The three bandwidths include the maximum available bandwidth for the CV data domes vehicles, 5.35 GHz, a mid level, but still large, bandwidth of 3.0 GHz, and a real-world operational bandwidth of 640 MHz. The lowest bandwidth of 640 MHz was chosen to mimic AFRL’s Sensor Data Management System (SDMS) real-world Gotcha SAR data collection of various target scenes [29]. Mean results for the original 24 experiments over the three possible bandwidths at 180° azimuth are shown in Table 4.6.

Table 4.6: Mean results for bandwidth experiments 1 – 24 at 180° azimuth, 40° elevation, and 5.35 GHz bandwidth.

El	# Train/Test	# RVs	% RV	MFW	AFW	$P_e$ %
		Sedan/SUV	Sedan/SUV	Sedan/SUV	Sedan/SUV	Sedan/SUV
640MHz	3629/892	62.92/62.04	1.74/1.71	188.63/179.34	36.09/33.69	5.74/32.52
3.0GHz	6866/1680	77.37/74.20	1.12/1.08	281.46/291.49	40.61/38.35	4.74/36.59
5.35GHz	8511/2063	75.45/75.41	0.88/0.88	143.94/129.40	36.09/34.46	4.86/38.08

The amount of extracted training and testing HRR feature vectors for RVM classification at each bandwidth are shown in Figure 4.33. As expected, a steady increase occurred in the SAR data sets as bandwidth rose from 640 MHz to the full 5.35 GHz. Post RVM classification, the total number of identified RVs are shown in Figure 4.34, and the percent of training feature vectors constituted as relevant are illustrated in Figure 4.35. Similar to aperture size saliency testing, larger SAR data sets, such as those using 5.35 GHz bandwidth or a 10° aperture size, are preferred for RVM classification due to the compressibility with which the RVM is able to sparsely, yet accurately, represent the data.

The downside to extremely large SAR phase history data sets, however, is the increased computational cost required to fully characterize saliency.

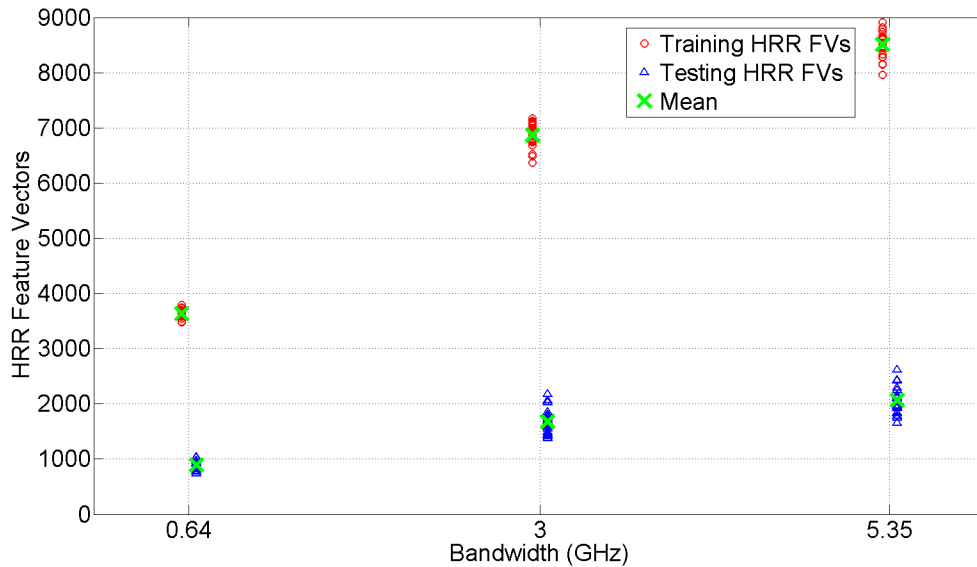


Figure 4.33: Total extracted train and test HRR feature vectors for bandwidth experiments at 180° azimuth.

Probability of RVM classification error results are shown in Figure 4.36. The results were not expected, however, as testing with 640 MHz bandwidth outperformed the two larger bandwidths for SUV experiments and was only slightly behind the other bandwidths for sedan experiments. The  $P_e$  results may indicate that an operational bandwidth around 640 MHz is sufficient to collect SAR phase history data of targets for effective RVM classification and other ATR applications. Additional bandwidth experiments at a separate azimuth angle are later conducted for verification of the initial results.

Before declaring 640 MHz as the desired bandwidth for 180° azimuth due to the favorable  $P_e$  results and reduced computational complexity, we must examine the salient

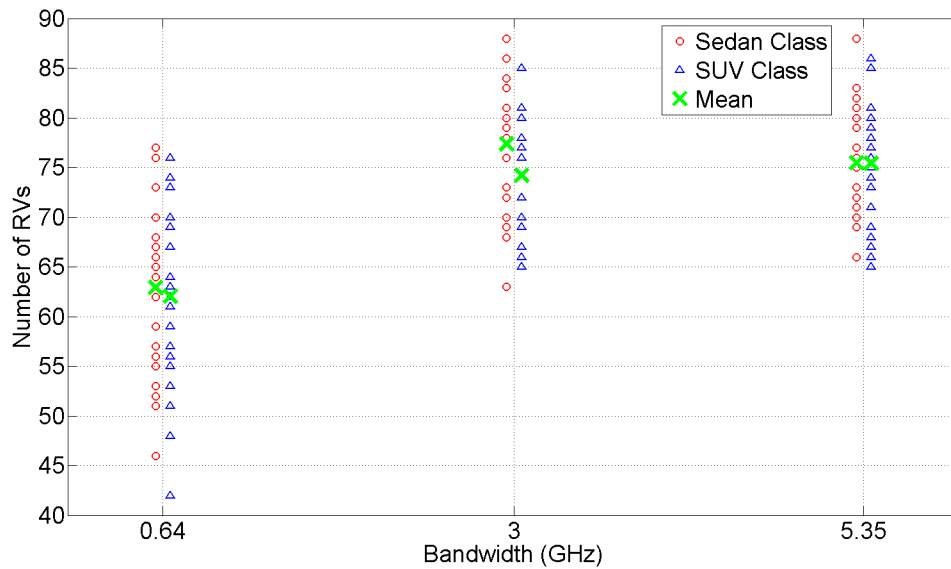


Figure 4.34: Total identified relevant HRR feature vectors for bandwidth experiments at 180° azimuth.

physical target features for classification. Previous parameter testing, to include azimuth, elevation, and aperture size, all use salient target feature histograms to identify the most significant physical shapes on the target surfaces contributing to classification decisions between sedan and SUV vehicles. The salient feature histogram analysis method provides excellent benefits to improving the classification process for ATR applications such as modeling and simulation by highlighting the target feature types that demand the greatest level of attention. Because azimuth, elevation, and aperture size testing involve collecting SAR target data from different vehicle aspects, however, the canonical shape histograms may only be used to aid in SAR classification performance for the specified parameters within each case. Since bandwidth testing involves comparing SAR target data from the same angular vehicle aspects, however, additional saliency information may be gathered by comparing the bandwidth histograms for potential misclassifications at reduced bandwidths.

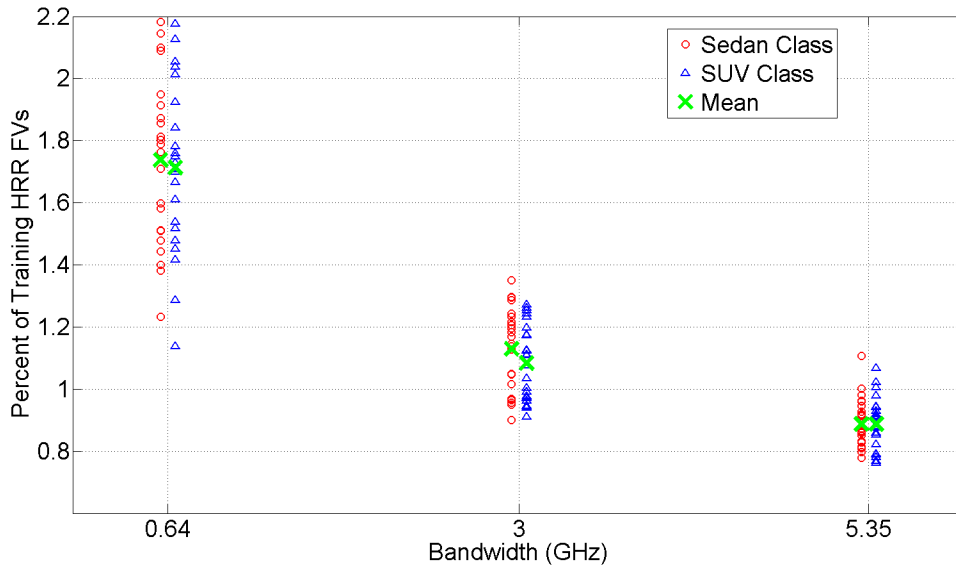


Figure 4.35: Percent of training HRR feature vectors deemed relevant for bandwidth experiments at 180° azimuth.

Identified relevant HRR feature vectors along with all extracted HRR feature vectors are once again classified as canonical shapes and presented as histograms for 640 MHz in Figure 4.37, for 3 GHz in Figure 4.38, and for 5.35 GHz in Figure 4.6. All three bandwidths recognize horizontal cylinders as the most relevant canonical shape to classification decisions, but beyond that, feature rankings vary. Consistency may be recognized across all three bandwidths in the fact that the top five canonical shapes for classification decisions are the same for all three bandwidths. The relative dependence on one target feature over another varies as bandwidth is adjusted, citing that the degradation in the resolution of the collected SAR data may have adverse affects on some target feature classifications at reduced bandwidths. Overall, however, the 640 MHz salient feature results are consistent enough with higher bandwidth results to highlight the top five most significant target features with little more than 10% of the total available bandwidth. In order to avoid as many target feature misclassifications as possible from degraded resolution, the desired

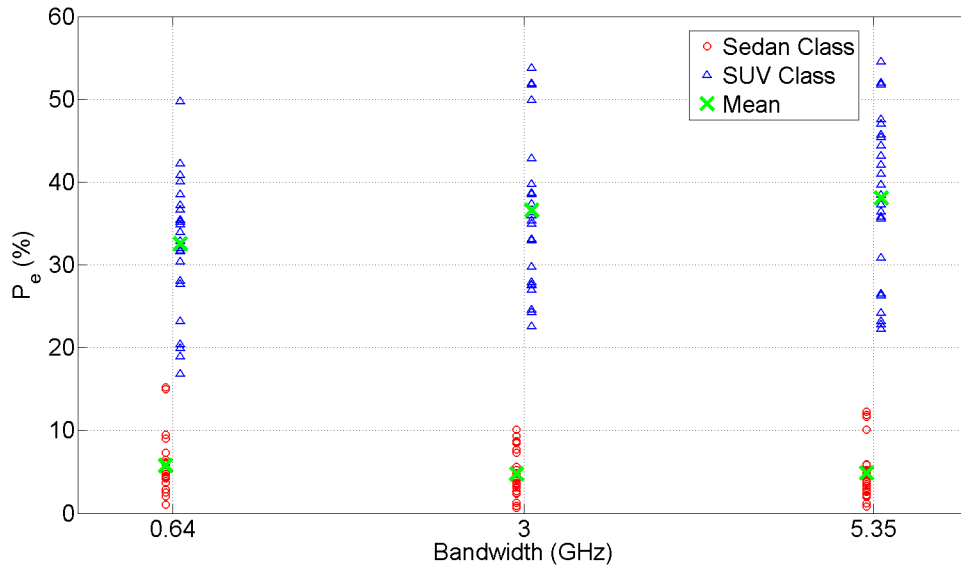


Figure 4.36: Probability of RVM classification error for extracted HRR feature vectors as seen throughout bandwidth experiments at 180° azimuth.

bandwidth recommendation for 180° azimuth is as much as available resources allow above the operational Gotcha [29] bandwidth of 640 MHz.

A second set of bandwidth experiments is conducted at 90° azimuth. All other parameters are held constant so that only effects of the varying bandwidth parameter may be observed. The mean results are shown in Table 4.7. To better visualize the results, Figure 4.39 through Figure 4.42 highlight the most significant findings contributing to the investigation into bandwidth saliency. The total amount of extracted training and testing HRR feature vectors in Figure 4.39, the amount of RVs identified by the RVM classifier in Figure 4.40, and the ratio of RVs to training HRR feature vectors in Figure 4.41 all remain consistent with the corresponding bandwidth results for 180° azimuth. One exception is that overall, less SAR data is collected on the vehicle targets at 90° azimuth than at 180° azimuth. As expected, the largest bandwidth creates the sparsest set of RVs relative to

the size of the training data set in Figure 4.41. Prior to weighing resource requirements and probability of test classification error results, 5.35 GHz would be the ideal desired bandwidth in regards to saliency.

Table 4.7: Mean results for bandwidth experiments 1 – 24 at 90° azimuth, 40° elevation, and 5.35 GHz bandwidth.

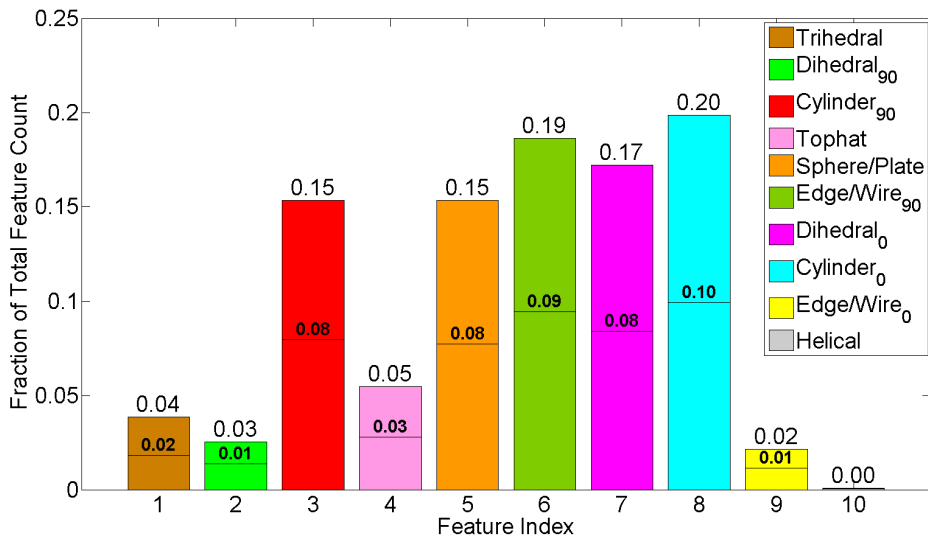
EI	# Train/Test	# RVs	% RV	MFW	AFW	$P_e$ %
		Sedan/SUV	Sedan/SUV	Sedan/SUV	Sedan/SUV	Sedan/SUV
640MHz	2588/642	47.12/45.29	1.81/1.75	566.31/567.96	64.37/66.11	2.82/31.83
3.0GHz	5195/1311	62.70/63.16	1.20/1.21	558.08/502.16	104.11/99.25	4.54/32.43
5.35GHz	6413/1642	61.79/60.79	0.96/0.94	409.87/430.98	84.82/83.83	4.42/31.23

We turn now to the bandwidth experiment  $P_e$  results at 90° azimuth, presented in Figure 4.42. Similar to results seen at 180° azimuth, no significant improvement in  $P_e$  is observed as bandwidth increases. In fact, sedan experiments at 640 MHz demonstrated the lowest average  $P_e$  value of the three bandwidths tested. All three bandwidths were consistent in that a small group of individual experiments demonstrated  $P_e$  results greater than 50%. Upon further investigation, it was discovered that all of the over 50% error results, and thus any  $P_e$  result greater than 40% in Figure 4.42, belonged to experiments in which the Tacoma pick-up truck was the vehicle under test, an adverse effect stemming from the relationship between physically dissimilar training and test vehicle class feature data.

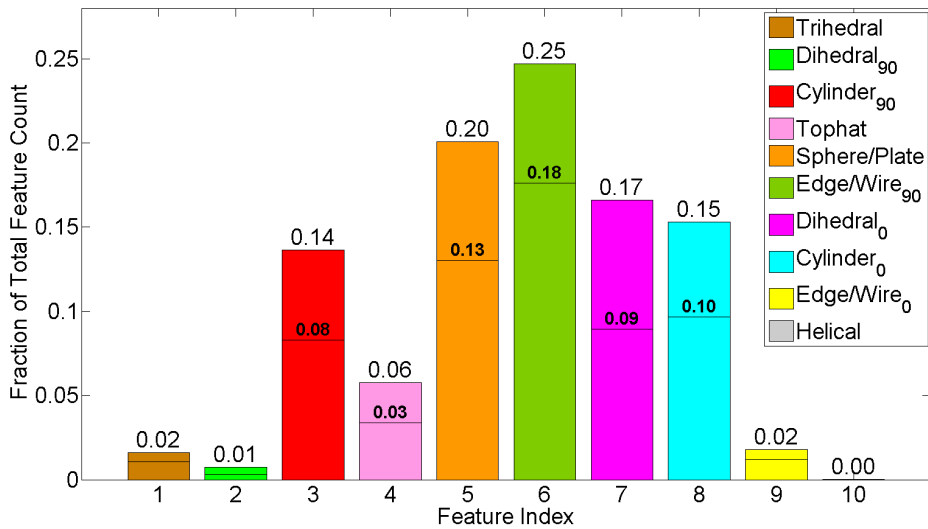
Histograms for bandwidth experiments at 90° azimuth are created for analysis of relevant target features between the sedan and SUV classes. The classified HRR feature vectors for 640 MHz bandwidth are shown in Figure 4.43, for 3 GHz bandwidth in



Figure 4.44, and for 5.35 GHz in Figure 4.5. Similar to bandwidth experiments at 180° azimuth, the potential for canonical feature misclassifications increases as bandwidth decreases. Notice, for example, that the most relevant target feature for class separation at 640 MHz in Figure 4.43a is the sphere/plate, while in Figure 4.44a at 3 GHz, the most relevant feature is the horizontal cylinder. In many cases, the relevant feature vectors may be referencing the same physical target feature and experiencing degraded classification performance. At reduced bandwidths, poorer resolution may cause some target features to blend, leading to inaccurate classification decisions. While sedan and SUV vehicle SAR targets collected with less bandwidth may still demonstrate comparable  $P_e$  results to the same targets collected with additional bandwidth, the classes being separated at reduced bandwidths may not be accurate enough representations of the complex CV targets. Subsequently, the conclusion in regards to saliency is that SAR CV targets should be collected with as much bandwidth as available resources allow between the two lowest bandwidths tested, 640 MHz and 3 GHz.

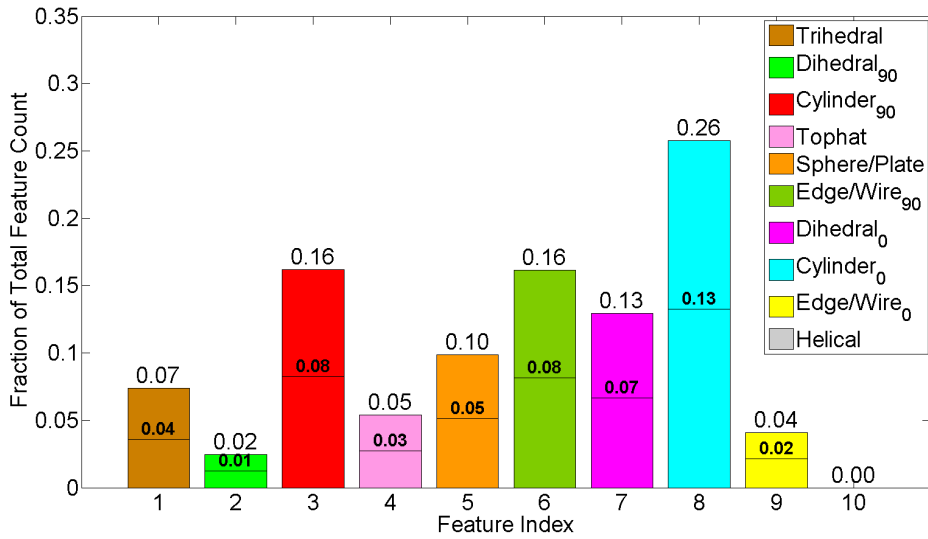


(a) Identified Relevant HRR Feature Vectors Only

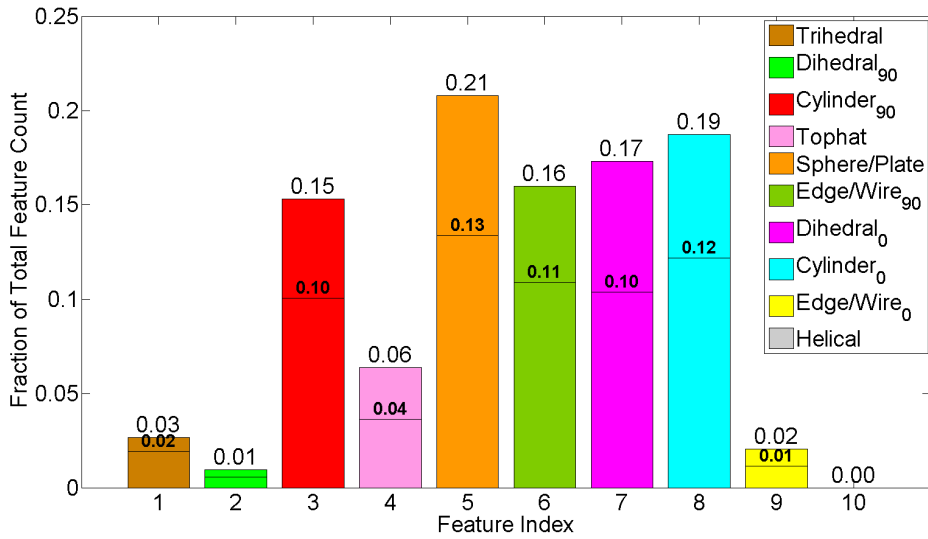


(b) All Extracted HRR Feature Vectors

Figure 4.37: Bandwidth experiment histograms for HRR FVs (BW 640 MHz, Az 180°). The dividing line illustrated on each canonical feature bar separates FVs according to class origin with sedan FVs below the line and SUV FVs above the line. The value over each dividing line indicates the fraction of only sedan FVs, and the value at the top of each feature bar indicates the fraction of all FVs classified as the specified canonical shape.



(a) Identified Relevant HRR Feature Vectors Only



(b) All Extracted HRR Feature Vectors

Figure 4.38: Bandwidth experiment histograms for HRR FVs (BW 3 GHz, Az 180°). The dividing line illustrated on each canonical feature bar separates FVs according to class origin with sedan FVs below the line and SUV FVs above the line. The value over each dividing line indicates the fraction of only sedan FVs, and the value at the top of each feature bar indicates the fraction of all FVs classified as the specified canonical shape.

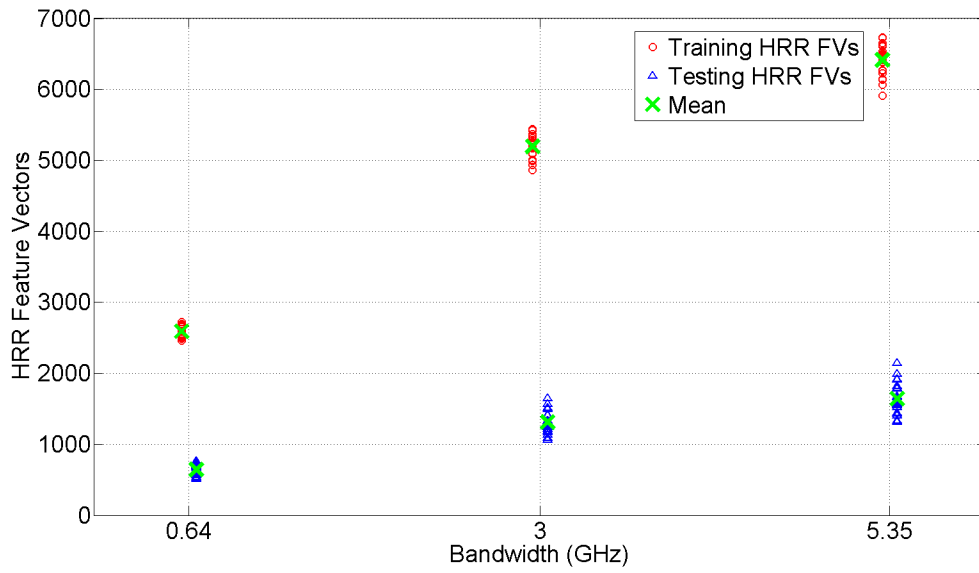


Figure 4.39: Total extracted train and test HRR feature vectors for bandwidth experiments at 90° azimuth.

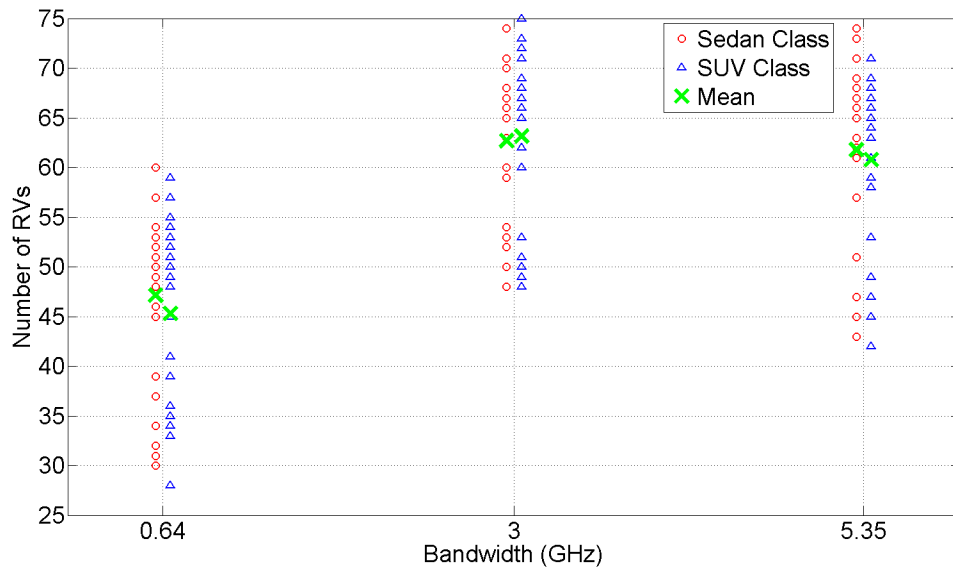


Figure 4.40: Total identified relevant HRR feature vectors for bandwidth experiments at 90° azimuth.

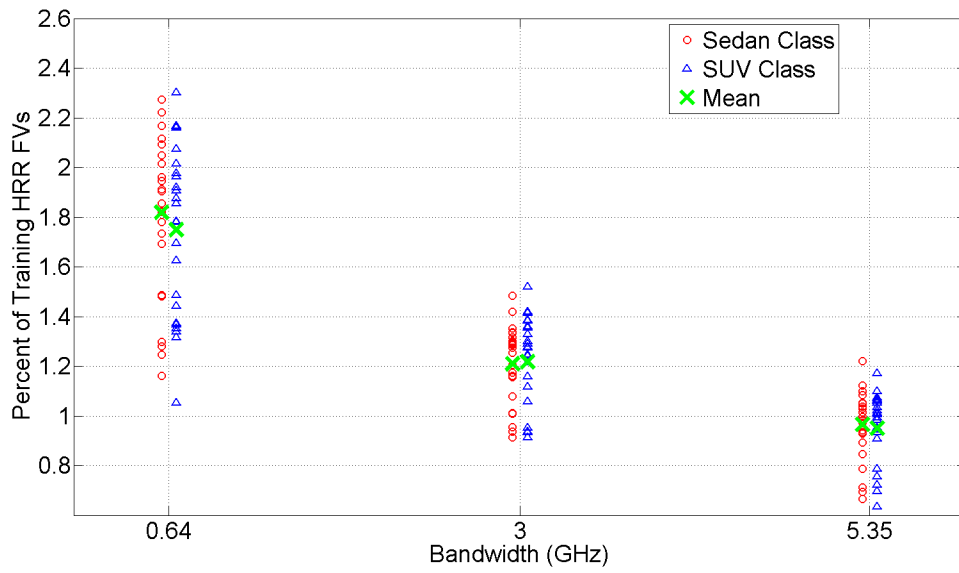


Figure 4.41: Percent of training HRR feature vectors deemed relevant for bandwidth experiments at 90° azimuth.

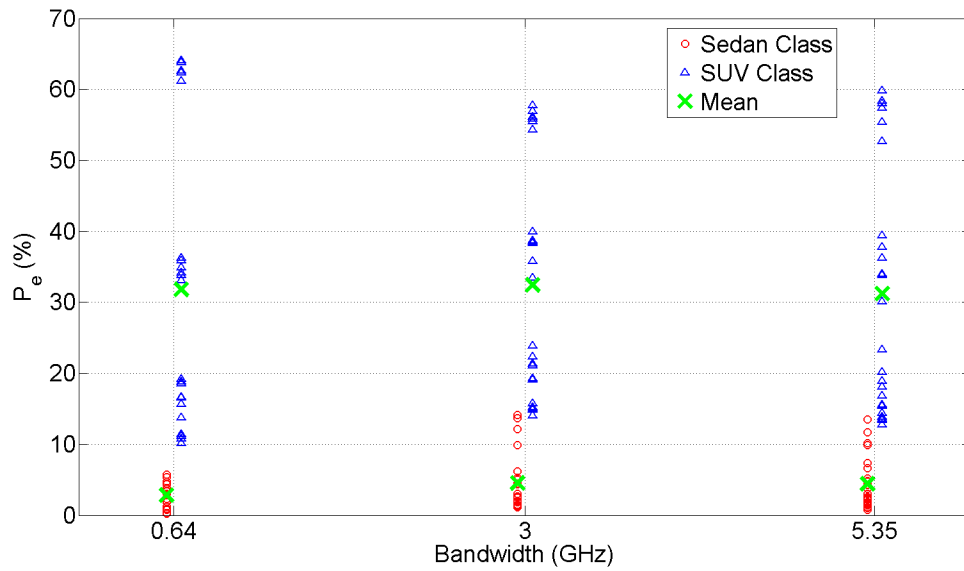
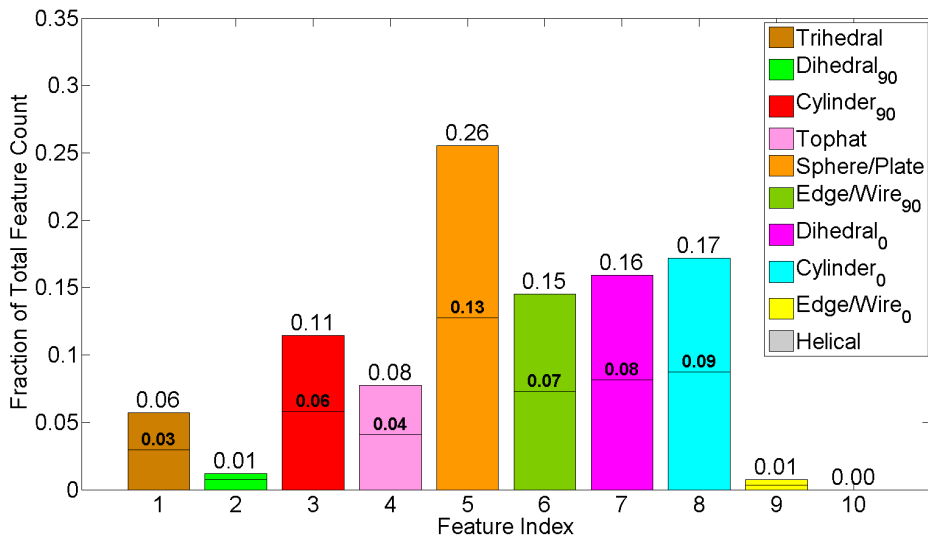
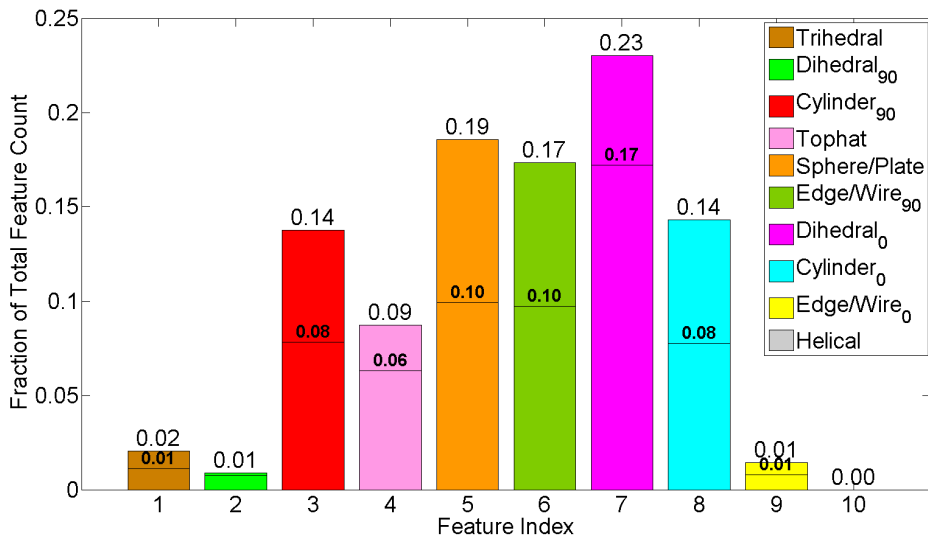


Figure 4.42: Probability of RVM classification error for extracted HRR feature vectors as seen throughout bandwidth experiments at 90° azimuth.

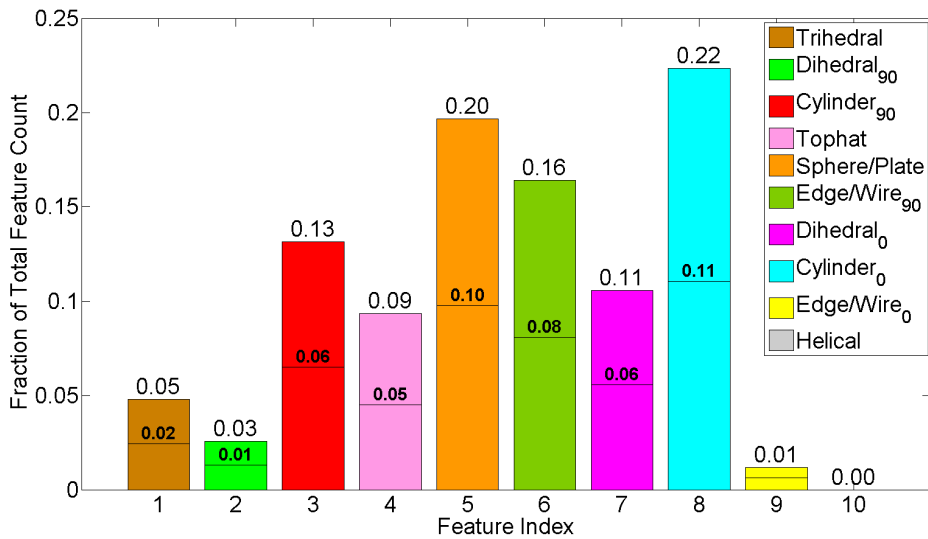


(a) Identified Relevant HRR Feature Vectors Only

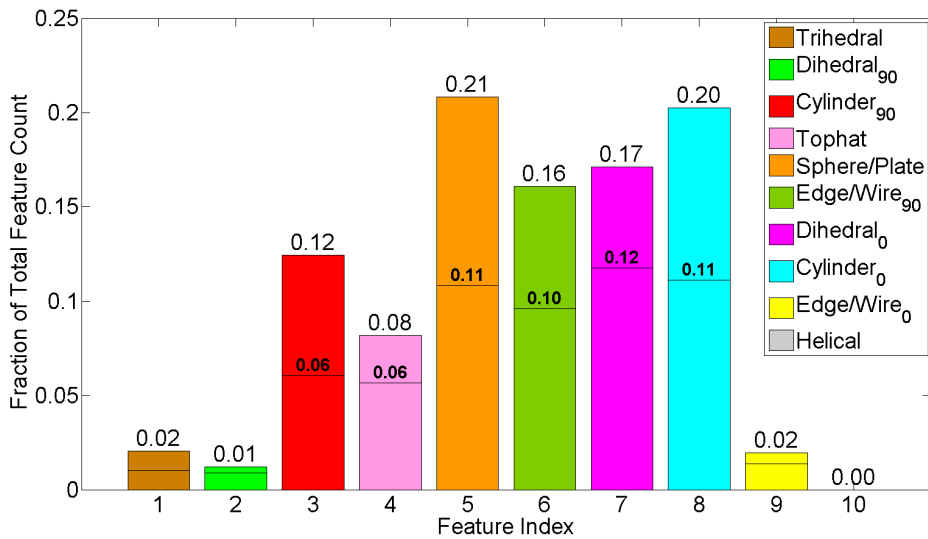


(b) All Extracted HRR Feature Vectors

Figure 4.43: Bandwidth experiment histograms for HRR FVs (BW 640 MHz, Az 90°). The dividing line illustrated on each canonical feature bar separates FVs according to class origin with sedan FVs below the line and SUV FVs above the line. The value over each dividing line indicates the fraction of only sedan FVs, and the value at the top of each feature bar indicates the fraction of all FVs classified as the specified canonical shape.



(a) Identified Relevant HRR Feature Vectors Only



(b) All Extracted HRR Feature Vectors

Figure 4.44: Bandwidth experiment histograms for HRR FVs (BW 3 GHz, Az 90°). The dividing line illustrated on each canonical feature bar separates FVs according to class origin with sedan FVs below the line and SUV FVs above the line. The value over each dividing line indicates the fraction of only sedan FVs, and the value at the top of each feature bar indicates the fraction of all FVs classified as the specified canonical shape.

## 4.2 Salient Feature Experiments for SPLIT Feature Vectors

In order to fully investigate the nature of saliency with regards to the effects on SAR binary classification performance, a second type of feature vector is extracted for classification and analysis. The SPLIT feature vector, expressed as  $(\alpha, k_e, k_o, x, y)$ , is a feature vector corresponding to  $x$  and  $y$  pixel locations on a SAR backprojected image. Details on the feature vector extraction methods are covered in Section 2.1, and background regarding the SPLIT algorithm may be found in Section 2.3.2 [8].

Similar to HRR feature vector saliency experiments, SPLIT feature vector experiments include testing azimuth angle, aperture size, elevation angle, and bandwidth SAR collection parameters. In some cases, the parameter values for SPLIT experiments are modified from HRR experiments due to the nature of the SPLIT algorithm. Primarily, aperture size testing for SPLIT feature vectors is increased to  $60^\circ (\pm 30^\circ)$ ,  $90^\circ (\pm 45^\circ)$ , and  $120^\circ (\pm 60^\circ)$ . The reason for the increase in aperture lies in the essence of SPLIT. Extracted HRR feature vectors include all received SAR phase history data, resulting in large feature vector data sets over even relatively small apertures. As discussed in Section 2.3.2, however, the primary goal of SPLIT is to classify SAR image peak pixels as canonical shapes according to the extracted frequency and polarization features. In doing so, many pixels are excluded for feature classification due to various thresholds which aim to highlight only image peaks. The primary benefit of the peak search process is an increased confidence in the pixels chosen for feature classification. The challenge in applying SPLIT feature vectors to our saliency investigation is that fewer feature vectors are extracted over a given parameter set, and as shown in HRR feature vector results, larger data sets are generally preferred for RVM classification due to the sparsity in RV class representation. Increasing aperture sizes allows the RVM sparsity concern to be addressed within SPLIT feature vector saliency experiments. While the specific SPLIT feature vector saliency recommendations for the aperture size parameter may differ from the HRR feature vector recommendations, the



effects of aperture size on sedan and SUV vehicle classification decisions remain fully characterized for both feature vector types. The full set of extracted SPLIT feature vector aperture size experiment results and analysis are detailed in Section 4.2.2.

Azimuth angle experiment results for extracted SPLIT feature vectors are presented and analyzed in Section 4.2.1. Due to the increase in aperture sizes for SPLIT testing, fewer azimuth angles were included for testing due to the extensive overlapping of azimuths. HRR testing included no overlap of azimuth angles, while most azimuths for SPLIT testing are incorporated in three separate azimuth experiment sets, allowing azimuth saliency to be sufficiently characterized with fewer parameter values. Elevation and bandwidth experiments for extracted SPLIT feature vectors are conducted at the same three SAR collection parameter values as the HRR feature vector experiments. The results and discussion for SPLIT elevation and bandwidth experiments may be found in Section 4.2.3 and Section 4.2.4, respectively. All extracted SPLIT feature vector saliency experiments are conducted according to the set-up parameters shown in Table 3.5.

#### ***4.2.1 Azimuth Angle Saliency Experiments for SPLIT Feature Vectors.***

The mean results for azimuth angle experiments with extracted SPLIT feature vectors are presented in Table 4.8. When comparing to the azimuth results for HRR feature vector testing, observe that while the percent of training data identified by the RVM as relevant is comparable between both extracted feature vector types, the total size of training, testing, and RV data sets are significantly reduced throughout SPLIT testing due to the image peak location properties of the original SPLIT algorithm. In initial testing, extracted SPLIT feature vector data sets were even smaller than the results presented in Table 4.8, but several configuration threshold properties were relaxed to increase the number of image peak pixels processed by SPLIT for improved RVM performance. Most notably, the side lobe level implemented in searching for image peaks for extraction was reduced from  $-32$

dB to  $-500$  dB, significantly increasing the number of extracted pixels over a particular aperture.

Table 4.8: Mean results for azimuth angle experiments 1–24 at  $40^\circ$  elevation,  $\pm 45^\circ$  aperture size, and 5.35 GHz bandwidth.

Az	# Train/Test	# RVs	% RV	MFW	AFW	$P_e$ %
		Sedan/SUV	Sedan/SUV	Sedan/SUV	Sedan/SUV	Sedan/SUV
$0^\circ$	1370.3/339.6	7.0/6.9	0.51/0.50	3.12/3.24	1.58/1.60	0.14/12.94
$45^\circ$	1408.6/350.3	6.3/5.9	0.44/0.42	3.52/3.64	1.67/1.70	0.27/9.84
$90^\circ$	1505.2/376.7	6.0/6.4	0.39/0.42	3.86/3.61	1.85/1.68	0.13/7.93
$135^\circ$	1553.1/389.9	10.0/9.6	0.64/0.62	15.90/14.69	5.52/5.02	0.59/7.46
$180^\circ$	1513.9/380.1	10.2/9.8	0.67/0.65	13.34/12.42	4.64/4.25	0.56/12.45

Extracted training and testing SPLIT feature vector totals are shown in Figure 4.45. Unlike HRR feature vector extraction, azimuth angle did not have any significant effect on the size of SPLIT feature vector training and testing data sets due to the selective nature of the SPLIT algorithm. The identified RV totals and percent of training data deemed relevant are illustrated in Figure 4.46 and Figure 4.47, respectively. While  $90^\circ$  azimuth achieved slightly more sparse relevant vector outputs when compared to the other tested azimuths, no clear area of interest may be highlighted in terms of saliency prior to analysis of test classification results.

Probability of RVM classification results for SPLIT feature vector azimuth tests are shown in Figure 4.48. First comparing the the SPLIT  $P_e$  results to the corresponding HRR  $P_e$  results from Figure 4.4, we notice that overall, SPLIT feature vector testing performed much better than HRR feature vector testing for both sedan and SUV classes. Similar to HRR testing, SPLIT sedan tests outperformed SPLIT SUV tests due to the size and

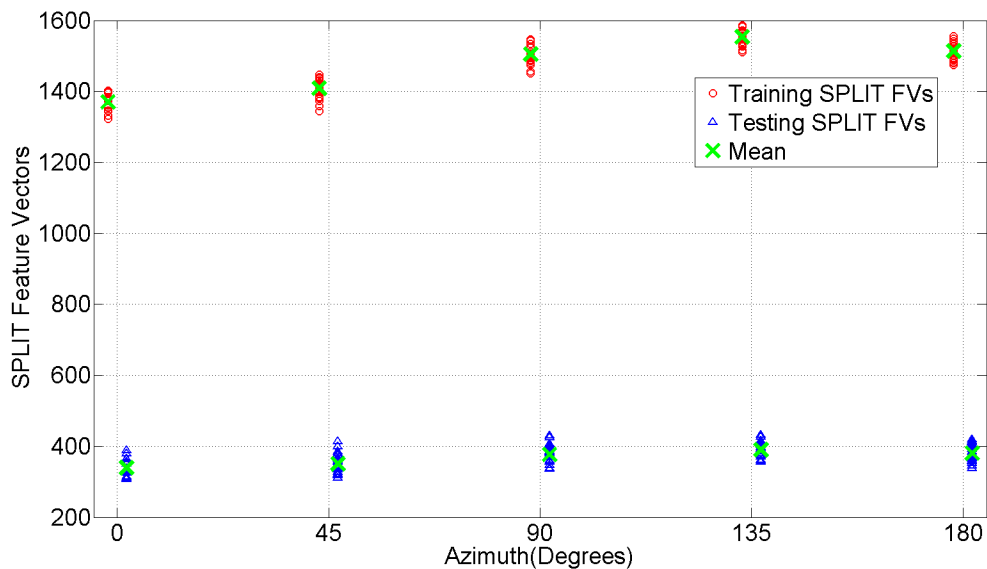


Figure 4.45: Total extracted train and test SPLIT feature vectors for azimuth angle experiments.

physical target feature dissimilarities between the sedan and SUV data classes. On average, however, the  $P_e$  results for extracted SPLIT feature vectors are significantly more accurate than the extracted HRR feature vector  $P_e$  results. The improvement in test classification error may be attributed to several reasons. First, using SAR backprojection to map pixel locations to a SAR image may provide increased separability of feature vectors through the RVM classification process. Choosing a feature set with  $x$  and  $y$  pixel coordinates may be more conducive to kernel-based class separation than an HRR feature vector that includes  $\phi$  and  $r$ . Another reason for the overall improvement in  $P_e$  performance for SPLIT may stem from the SPLIT image peak selection process. By throwing out pixels that do not qualify for accurate classification, SPLIT creates smaller but more more separable classes for the RVM to make classification decisions between, thus improving  $P_e$  test results. A third reason for the improvement may come from the necessary increase in SPLIT aperture size. Cumbersome extracted HRR feature vector data sets over small apertures may create

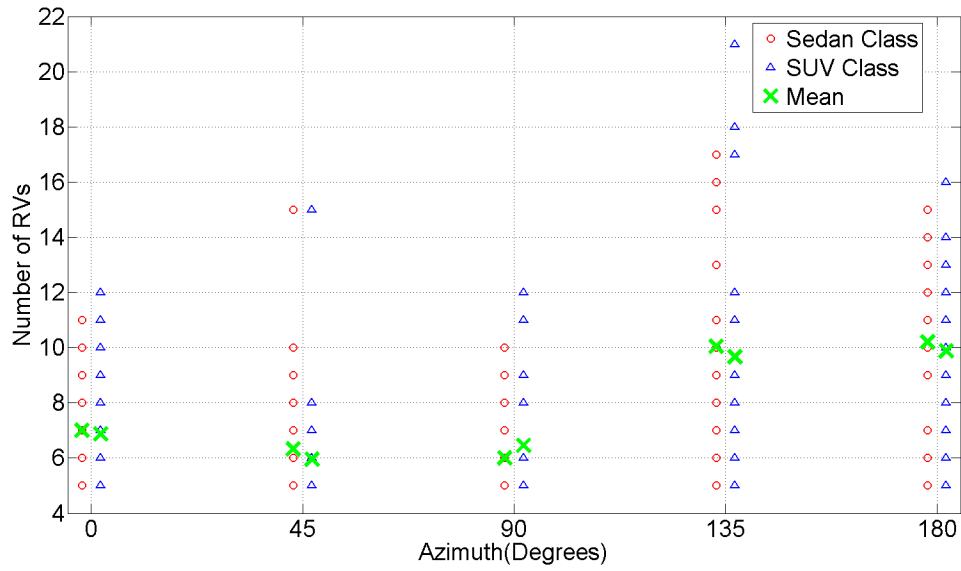


Figure 4.46: Total identified relevant SPLIT feature vectors for azimuth angle experiments.

data classes muddled with many similar feature vectors, making classification decisions more difficult for the RVM. The SPLIT selective image peak search over a larger aperture creates more distinctive feature vectors from many different vehicle aspects, leading to a more simplified class separation and representation throughout the RVM process.

Comparing only the SPLIT feature vector  $P_e$  results across azimuth, notice that  $90^\circ$  and  $135^\circ$  performed slightly better than the other azimuths tested, highlighting the side specular and rear canted azimuths as the most important to accurate vehicle classification decisions. The results agree with the HRR azimuth  $P_e$  results from Section 4.1.1 which identifies the rear canted azimuths, specifically  $112.5^\circ$ , as the most desired to RVM class decisions.

Histograms highlighting the most significant physical target features for classification are shown alongside all extracted SPLIT feature vectors in Figure 4.49 for  $90^\circ$  azimuth, Figure 4.50 for  $135^\circ$  azimuth, and Figure 4.51 for  $180^\circ$  azimuth. All SPLIT feature vector

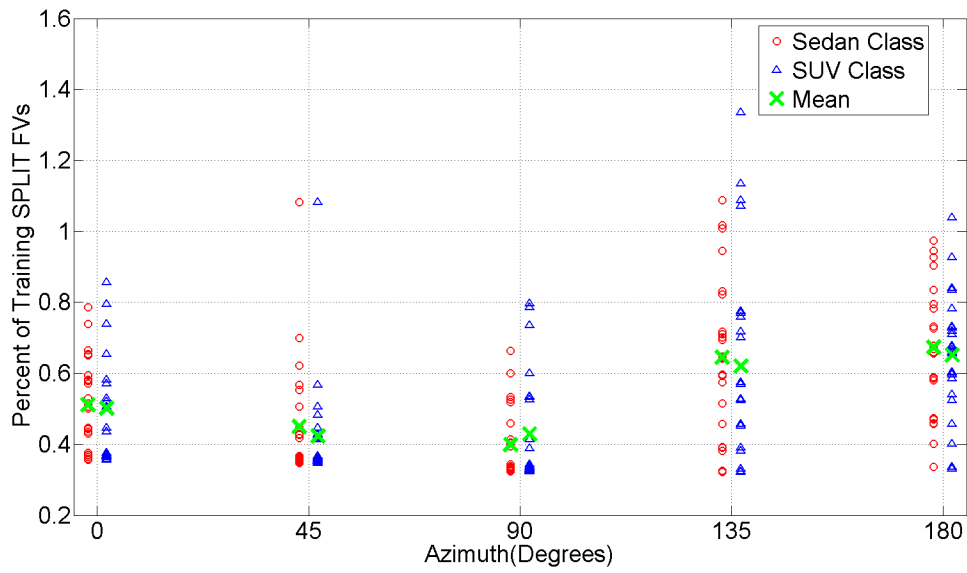


Figure 4.47: Percent of training SPLIT feature vectors deemed relevant for azimuth angle experiments.

histograms demonstrate less variation among physical target features than HRR feature vector histograms due to the classification limitations implemented throughout the SPLIT algorithm. At all three highlighted azimuths, horizontal cylinders are considered most significant to classification decisions. At  $90^\circ$  azimuth, the target feature gaining the most relevance from all extracted SPLIT feature vectors is the horizontal dihedral, which rose from 21% of all feature vectors to 27% of relevant feature vectors. Another significant emphasis in relevance may be observed at  $180^\circ$  azimuth, where trihedral features increased from 13% of all SPLIT feature vectors to 21% of the relevant SPLIT feature vectors. The upsurge in relevance of particular target features demand increased attention for improving SAR classification performance.

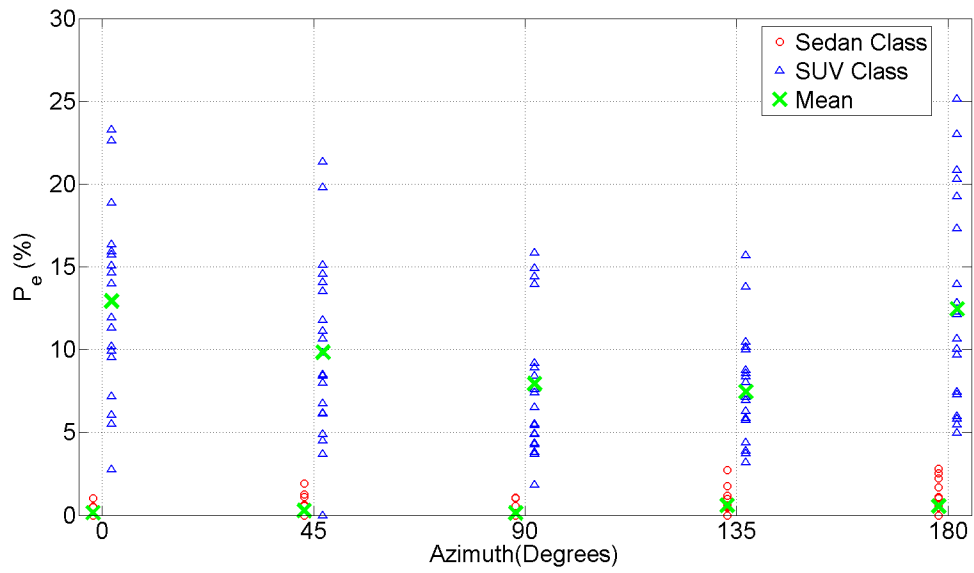
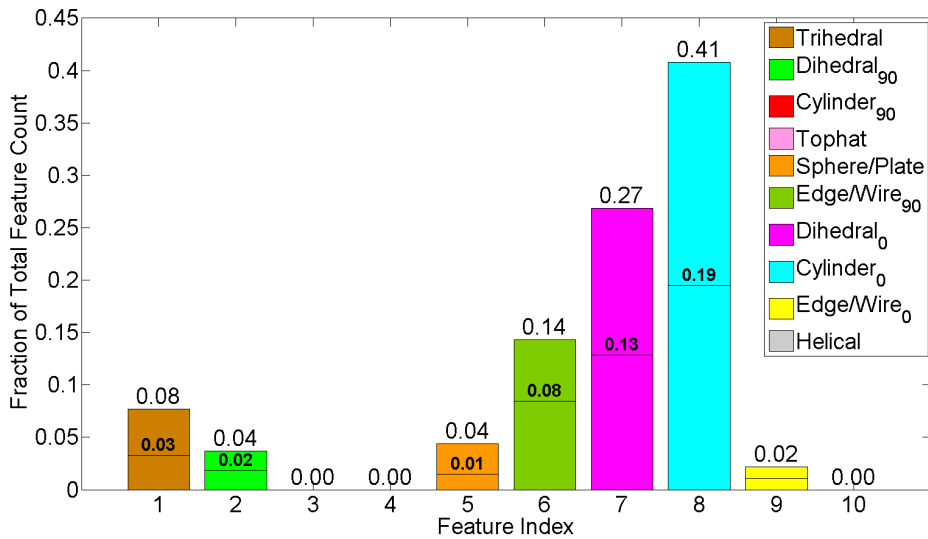
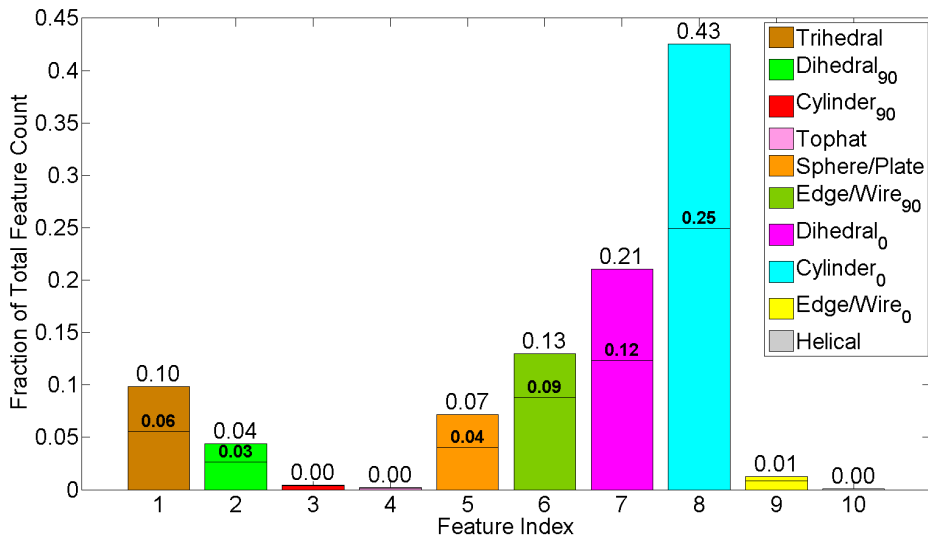


Figure 4.48: Probability of RVM classification error for extracted SPLIT feature vectors as seen throughout azimuth angle experiments.

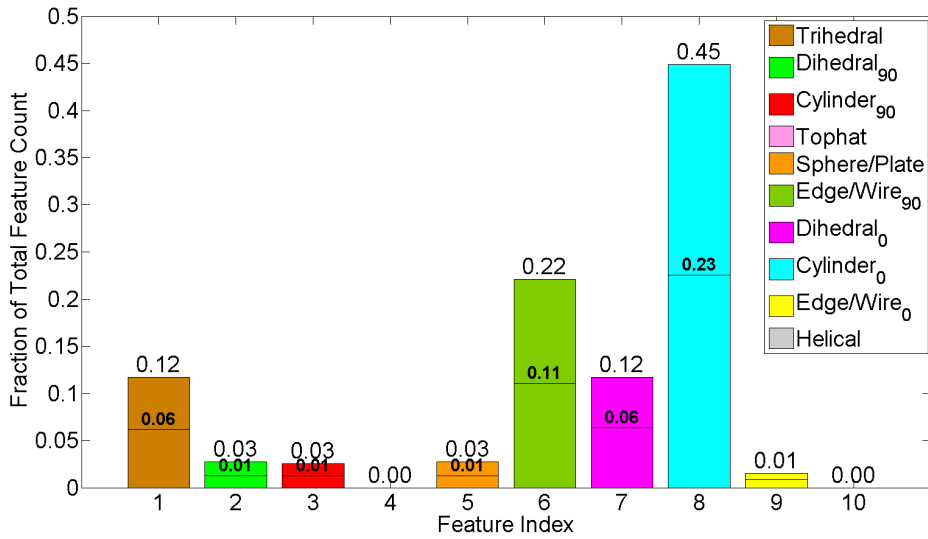


(a) Identified Relevant SPLIT Feature Vectors Only

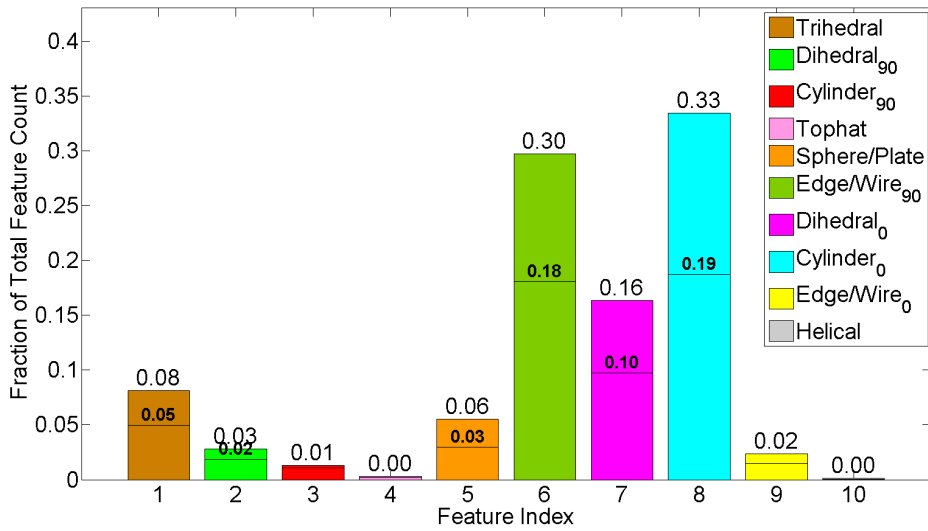


(b) All Extracted SPLIT Feature Vectors

Figure 4.49: Azimuth angle experiment histograms for SPLIT FVs ( $Az\ 90^\circ$ ). The dividing line illustrated on each canonical feature bar separates FVs according to class origin with sedan FVs below the line and SUV FVs above the line. The value over each dividing line indicates the fraction of only sedan FVs, and the value at the top of each feature bar indicates the fraction of all FVs classified as the specified canonical shape.



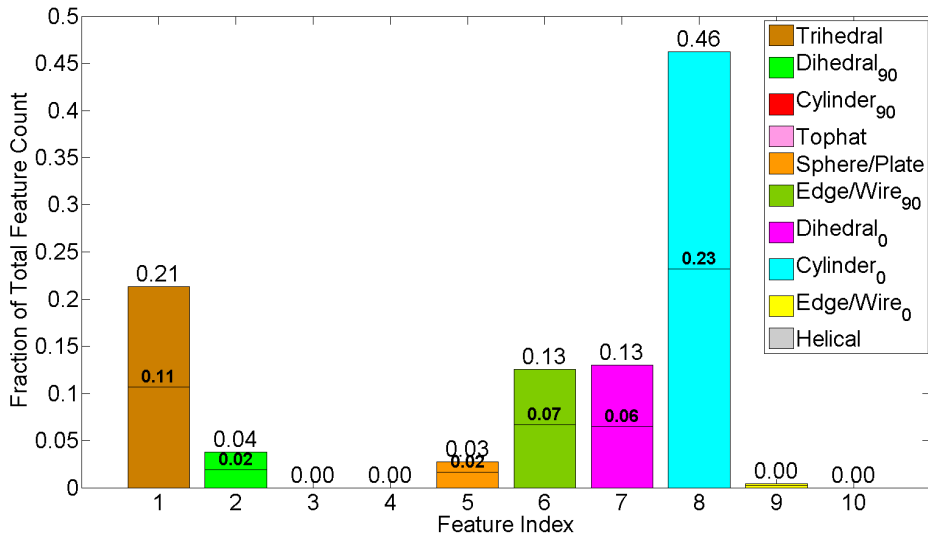
(a) Identified Relevant SPLIT Feature Vectors Only



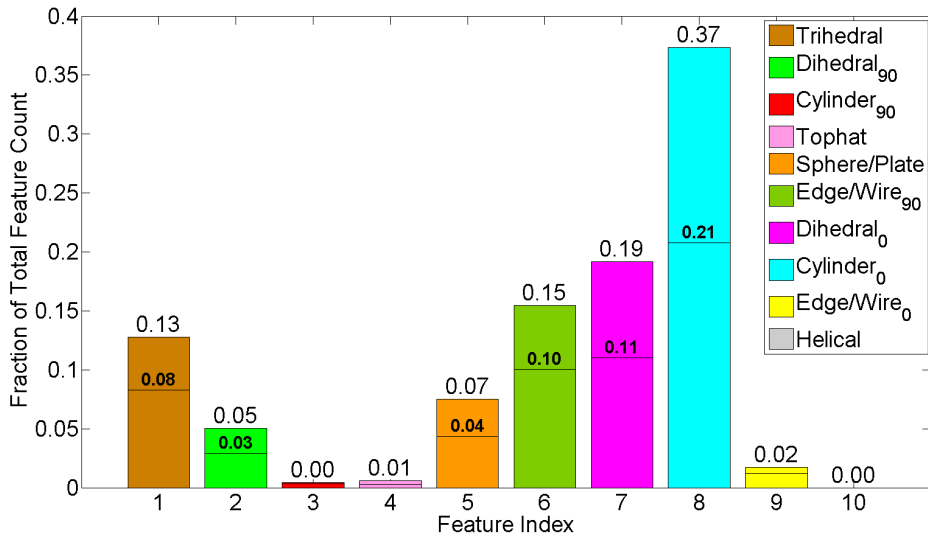
(b) All Extracted SPLIT Feature Vectors

Figure 4.50: Azimuth angle experiment histograms for SPLIT FVs ( $Az\ 135^\circ$ ). The dividing line illustrated on each canonical feature bar separates FVs according to class origin with sedan FVs below the line and SUV FVs above the line. The value over each dividing line indicates the fraction of only sedan FVs, and the value at the top of each feature bar indicates the fraction of all FVs classified as the specified canonical shape.





(a) Identified Relevant SPLIT Feature Vectors Only



(b) All Extracted SPLIT Feature Vectors

Figure 4.51: Azimuth angle experiment histograms for SPLIT FVs (Az 180°). The dividing line illustrated on each canonical feature bar separates FVs according to class origin with sedan FVs below the line and SUV FVs above the line. The value over each dividing line indicates the fraction of only sedan FVs, and the value at the top of each feature bar indicates the fraction of all FVs classified as the specified canonical shape.

#### 4.2.2 Aperture Size Saliency Experiments for SPLIT Feature Vectors.

The next set of experiments tested varying aperture size using extracted SPLIT feature vectors. As previously discussed, aperture sizes were increased to accommodate the selective SPLIT image peak search in order to provide the RVM classifier with enough data for stable classification. Aperture sizes of  $60^\circ(\pm 30^\circ)$ ,  $90^\circ(\pm 45^\circ)$ , and  $120^\circ(\pm 60^\circ)$  were used at  $90^\circ$  azimuth,  $40^\circ$  elevation, and the full 5.35 GHz bandwidth. The results are summarized in Table 4.9.

Table 4.9: Mean results for aperture size experiments 1 – 24 at  $90^\circ$  azimuth,  $40^\circ$  elevation, and 5.35 GHz bandwidth.

Ap Size	# Train/Test	# RVs	% RV	MFW	AFW	$P_e$ %
		Sedan/SUV	Sedan/SUV	Sedan/SUV	Sedan/SUV	Sedan/SUV
$\pm 30^\circ$	1058.9/268.0	6.0/6.4	0.56/0.60	3.78/4.29	1.93/2.10	0.33/5.89
$\pm 45^\circ$	1505.2/376.7	6.0/6.5	0.39/0.42	3.86/3.61	1.85/1.68	0.13/7.93
$\pm 60^\circ$	1951.2/488.7	6.7/7.5	0.34/0.38	2.62/2.85	1.42/1.56	0.24/10.38

The total number of extracted training and testing SPLIT feature vectors, identified RVs, and ratio of RVs to training data are illustrated in Figure 4.52, Figure 4.53, and Figure 4.54, respectively. As expected, results are consistent with aperture size experimental results using extracted HRR feature vectors. As aperture size increases, the amount of extracted SPLIT feature vectors increases, and since similar totals of RVs are output by the RVM at all aperture sizes, the largest aperture size is preferred by the classifier due to the compressibility with which it represents and separates the two classes.

Probability of classification error results are shown in Figure 4.55. While the  $\pm 45^\circ$  aperture size demonstrated the lowest mean error for sedan tests, the smallest aperture size tested,  $\pm 30^\circ$ , had the lowest average  $P_e$  for SUV tests. The RVM classification

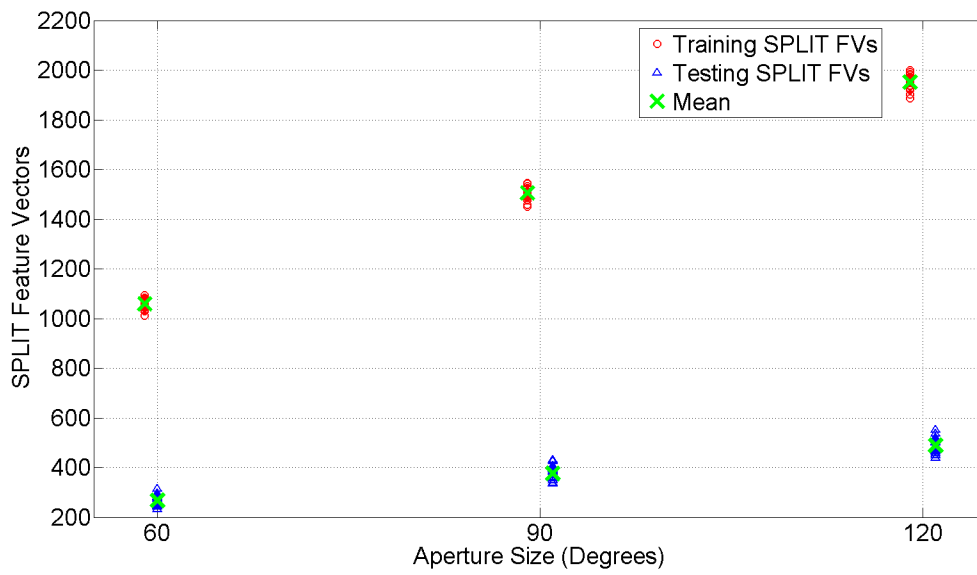


Figure 4.52: Total extracted train and test SPLIT feature vectors for aperture size experiments at 90° azimuth.

tests performed well at all three aperture sizes, but considering the reduction in resource requirements,  $\pm 30^\circ$  is considered the desired aperture size for extracted SPLIT feature vector experiments. Although the middle aperture size was chosen for HRR experiments due to the potential classification vulnerability of the smallest aperture size ( $3^\circ$ ), the smallest aperture size for SPLIT feature vector experiments does not pose the same concerns because the large increase in vehicle aspect coverage ensures radar exposure to many distinguishable target features.

Target features aiding most in RVM classification are shown in Figure 4.56a for  $\pm 30^\circ$  aperture, Figure 4.49a for  $\pm 45^\circ$  aperture, and Figure 4.57a for  $\pm 60^\circ$  aperture. Each RV histogram is illustrated with the corresponding histogram for all extracted SPLIT feature vectors at the specified parameters. Comparing Figure 4.56a and Figure 4.56b at  $\pm 30^\circ$  aperture, observe that the RVM emphasizes horizontal cylinders and trihedrals while

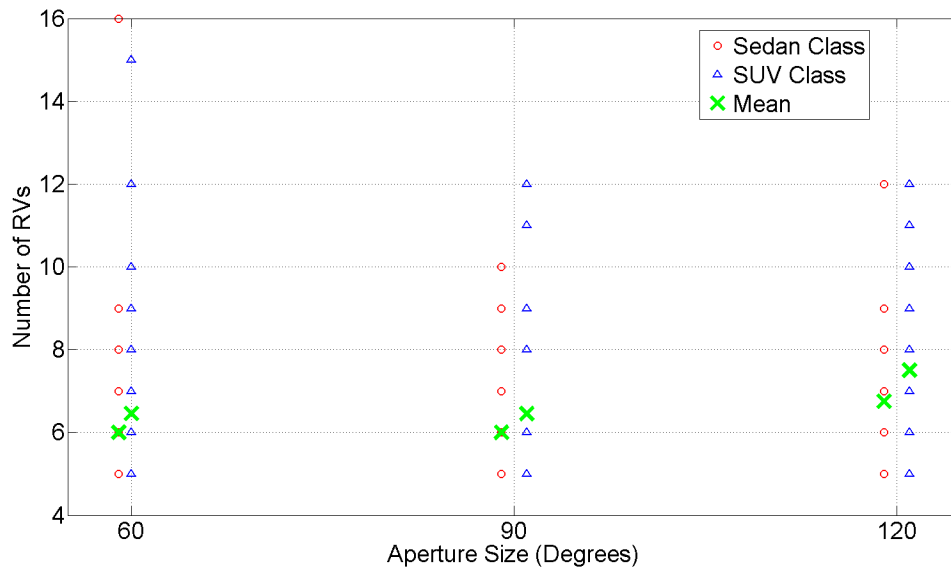


Figure 4.53: Total identified relevant SPLIT feature vectors for aperture size experiments at 90° azimuth.

deemphasizing horizontal dihedrals for classification decisions. Increasing aperture size to  $\pm 60^\circ$  demonstrates relatively consistent results between Figure 4.57a and Figure 4.57b, with the most significant increase in relevant SPLIT feature vectors stemming from trihedral feature classifications.

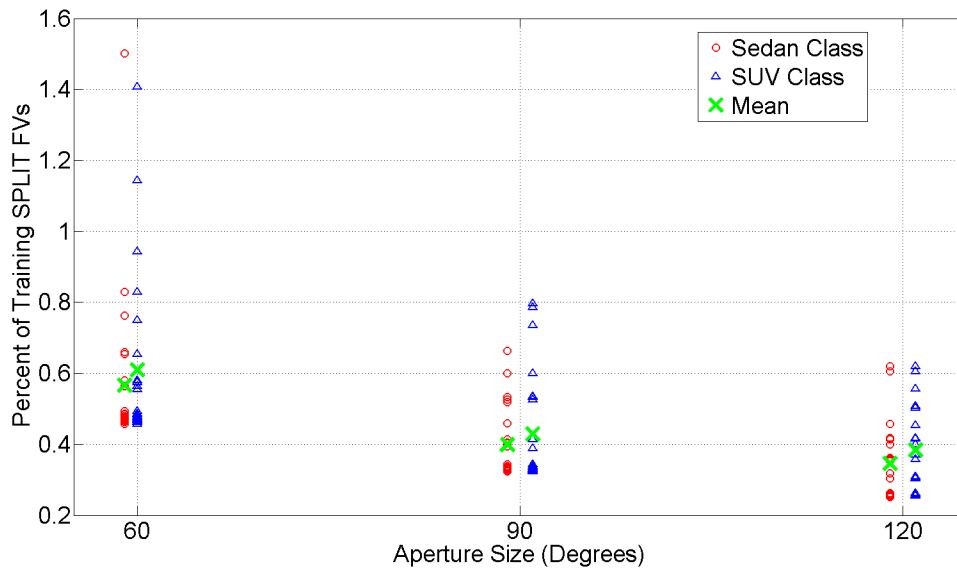


Figure 4.54: Percent of training SPLIT feature vectors deemed relevant for aperture size experiments at 90° azimuth.

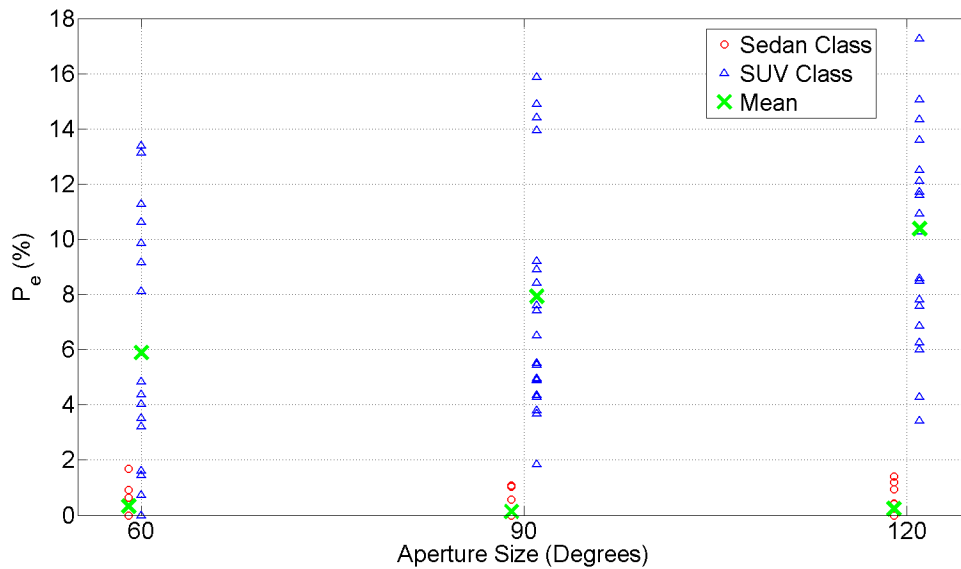
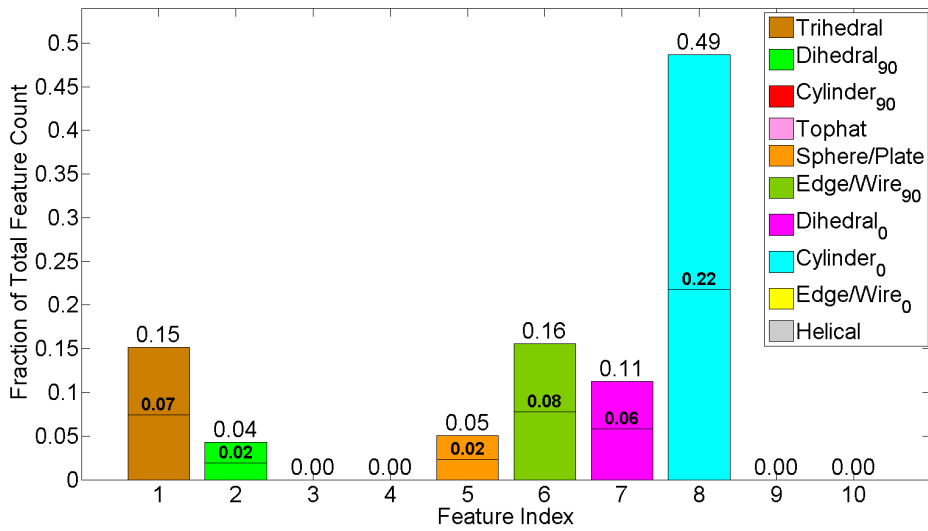
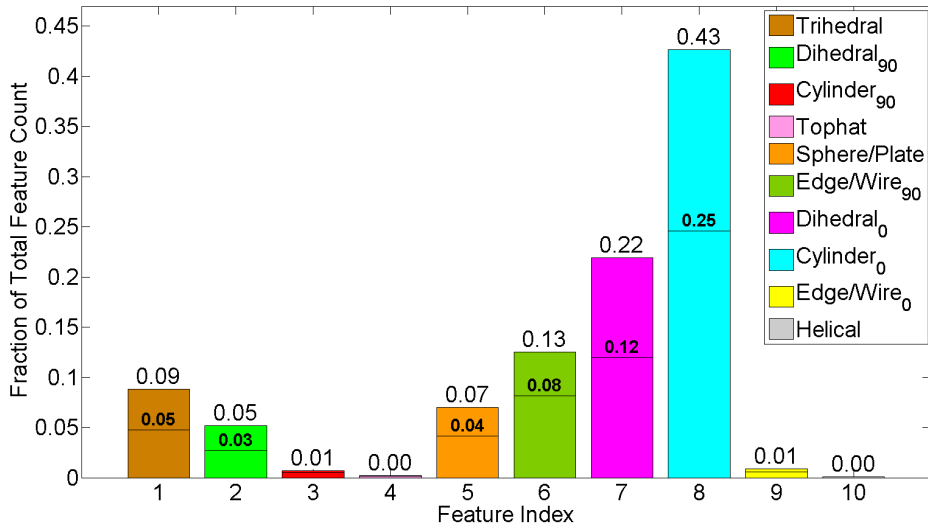


Figure 4.55: Probability of RVM classification error for extracted SPLIT feature vectors as seen throughout aperture size experiments at 90° azimuth.

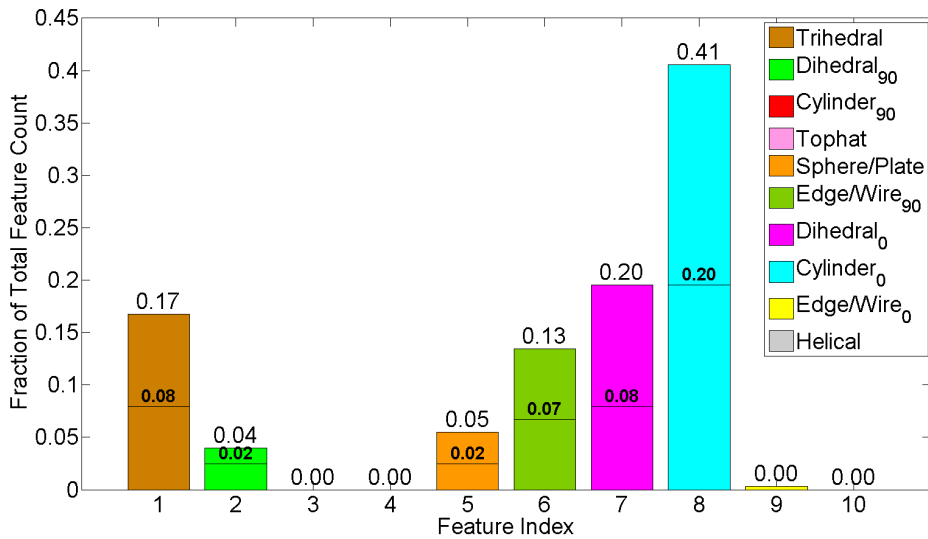


(a) Identified Relevant SPLIT Feature Vectors Only

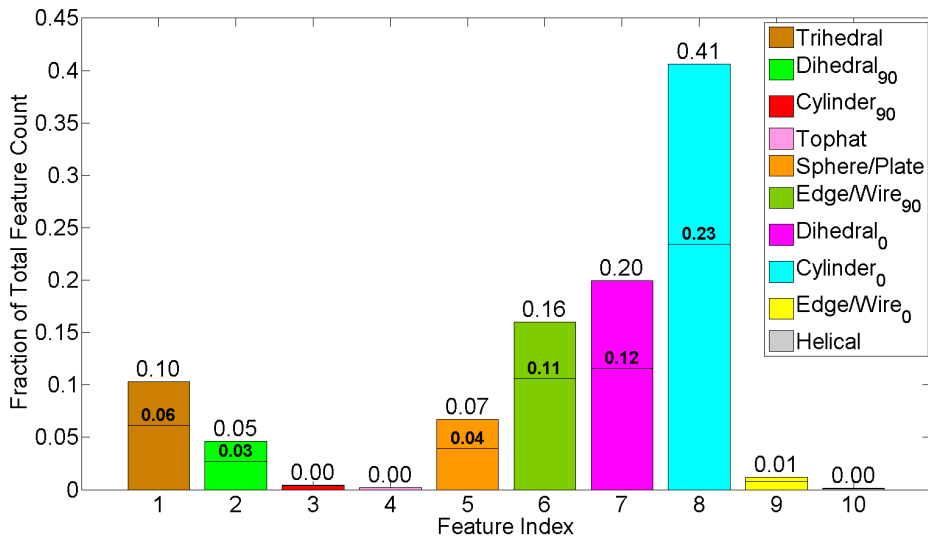


(b) All Extracted SPLIT Feature Vectors

Figure 4.56: Aperture size experiment histograms for SPLIT FVs (Ap size  $60^\circ$ , Az  $90^\circ$ ). The dividing line illustrated on each canonical feature bar separates FVs according to class origin with sedan FVs below the line and SUV FVs above the line. The value over each dividing line indicates the fraction of only sedan FVs, and the value at the top of each feature bar indicates the fraction of all FVs classified as the specified canonical shape.



(a) Identified Relevant SPLIT Feature Vectors Only



(b) All Extracted SPLIT Feature Vectors

Figure 4.57: Aperture size experiment histograms for SPLIT FVs (Ap size 120°, Az 90°). The dividing line illustrated on each canonical feature bar separates FVs according to class origin with sedan FVs below the line and SUV FVs above the line. The value over each dividing line indicates the fraction of only sedan FVs, and the value at the top of each feature bar indicates the fraction of all FVs classified as the specified canonical shape.

### 4.2.3 Elevation Angle Saliency Experiments for SPLIT Feature Vectors.

Elevation angle experiments for extracted SPLIT feature vectors considered the same three elevations as HRR experiments, 30°, 40°, and 50°. SPLIT elevation experiments are conducted at 180° azimuth, ±45° aperture size, and 5.35 GHz bandwidth. The summary of mean results for all SPLIT elevation experiments are included in Table 4.10.

Table 4.10: Mean results for elevation angle experiments 1 – 24 at 180° azimuth, ±45° aperture size, and 5.35 GHz bandwidth.

El	# Train/Test	# RVs	% RV	MFW	AFW	$P_e$ %
		Sedan/SUV	Sedan/SUV	Sedan/SUV	Sedan/SUV	Sedan/SUV
30°	2236.08/571.91	6.33/6.45	0.28/0.29	1.78/1.54	0.94/0.84	0.24/4.26
40°	1513.91/380.08	10.20/9.87	0.67/0.65	13.34/12.42	4.64/4.25	0.56/12.45
50°	1146.25/289.75	5.08/5.12	0.44/0.44	2.31/2.17	1.45/1.37	0.08/8.68

The total size of the training and testing data sets for extracted SPLIT feature vectors is shown in Figure 4.58. An interesting result is seen when comparing Figure 4.58 to the corresponding HRR result in Figure 4.21. While the number of extracted HRR feature vectors increase as elevation angle increases, presumably due to the radar being exposed to a larger amount of target surface, the number of extracted SPLIT feature vectors decreases with increasing elevation angle. This inverse result may be explained by considering the findings of HRR elevation experiments and the nature of the SPLIT algorithm. As discussed in Section 4.1.3, the most distinct and recognizable CV target features are found below the roof line of vehicles seen best at lower elevation angles. As SPLIT conducts its image peak search, many more of the unique features visible at lower azimuths are chosen for SPLIT feature extraction, increasing the size of the training and testing data sets. Alternatively, while a greater amount of vehicle target surface may be visible at higher



elevation angles, fewer pixels are identified as SPLIT image peaks and thus many pixels are eliminated prior to feature vector extraction.

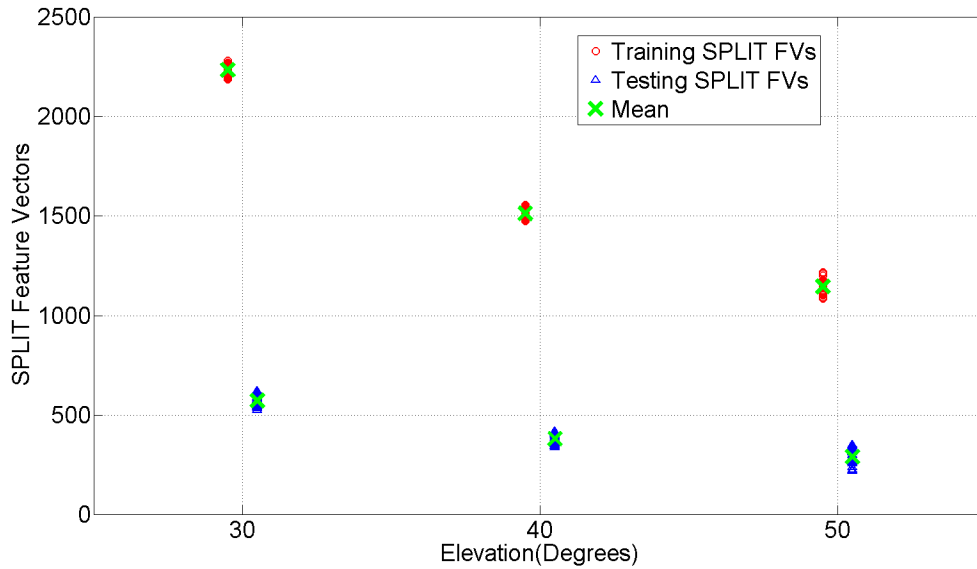


Figure 4.58: Total extracted train and test SPLIT feature vectors for elevation angle experiments at 180° azimuth.

The number of identified relevant SPLIT feature vectors and the percent of training data considered relevant are presented in Figure 4.59 and Figure 4.60, respectively. Figure 4.60 highlights 30° as the elevation that the RVM is able to compress most effectively. Probability of classification error results are shown in Figure 4.61. While 50° elevation demonstrates a slightly lower sedan test classification error, 30° elevation produces comparable sedan error and a very impressive average SUV test error of 4.26%. Even more impressive, no individual test at 30° elevation demonstrated  $P_e$  greater than 10%. Consistent with the result for HRR elevation experiments, the recommended elevation for SPLIT feature vector experiments is 30°.

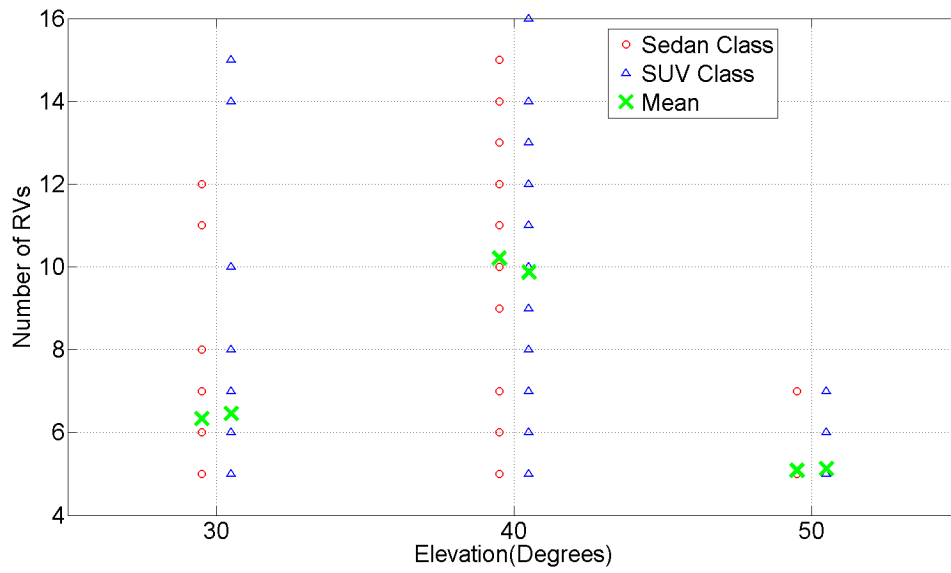


Figure 4.59: Total identified relevant SPLIT feature vectors for elevation angle experiments at 180° azimuth.

Histograms are created for elevation angle experiment comparisons of all extracted SPLIT feature vectors and relevant SPLIT feature vectors as determined by the RVM classifier. The histograms for 30° elevation are shown in Figure 4.62, 40° elevation in Figure 4.51, and 50° elevation in Figure 4.63. First comparing all extracted SPLIT feature vectors, observe that similar to the results from HRR elevation experiments, more unique target features are classified at 30° elevation, such as the increase in vertical edges/wires in Figure 4.62b when compared to Figure 4.51b and Figure 4.63b. Elevations of 40° and 50° are very similar, classifying horizontal cylinders and horizontal dihedrals above all else at the 180° azimuth rear vehicle aspect. Histogram results at 30° elevation again stand out when compared to 40° and 50° elevations for extracted SPLIT feature vectors. The consistent distinction observed at lower elevation provides increased potential separability of civilian vehicle target classes for improved SAR classification performance.

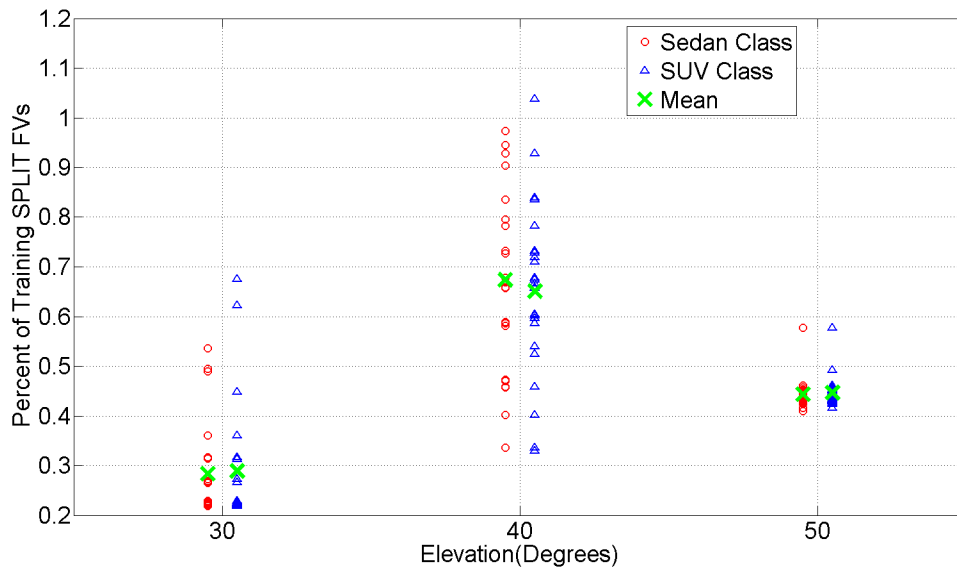


Figure 4.60: Percent of training SPLIT feature vectors deemed relevant for elevation angle experiments at 180° azimuth.

Elevation angle also played an important role in determining which canonical shapes the RVM emphasized for classification decisions. At 30° elevation, horizontal dihedrals were given increased importance while vertical edges/wires were deemphasized as shown in Figure 4.62a. While both 40° and 50° elevations found an increase in relevance for trihedral features in Figure 4.51a and Figure 4.63a, respectively, the RVM placed additional significance on sphere/plate classifications at 40° elevation and vertical edges/wires at 50° elevation.

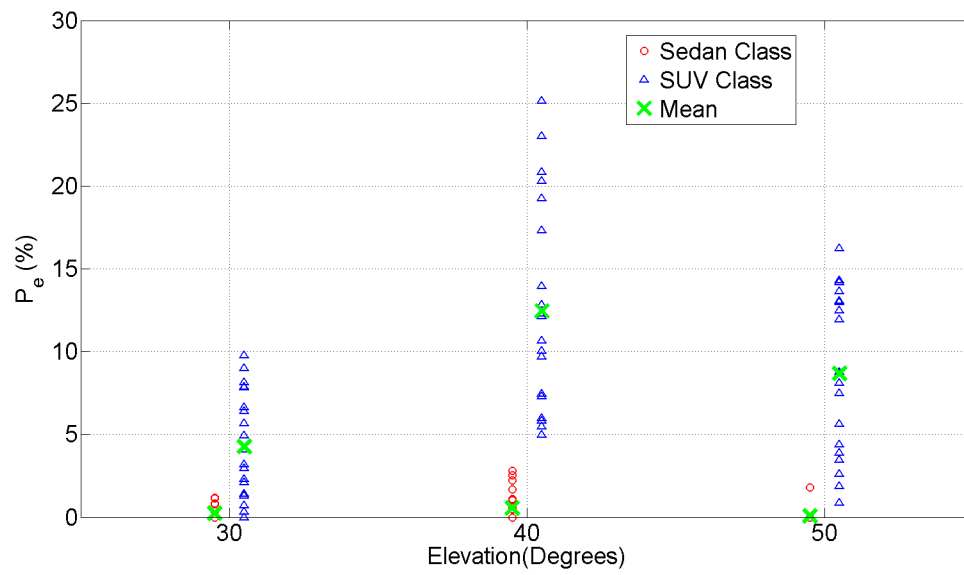
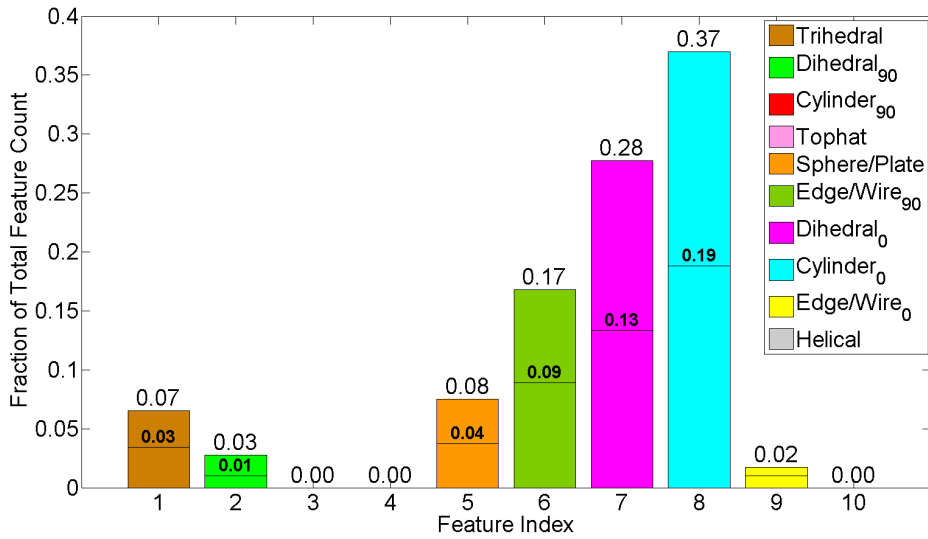
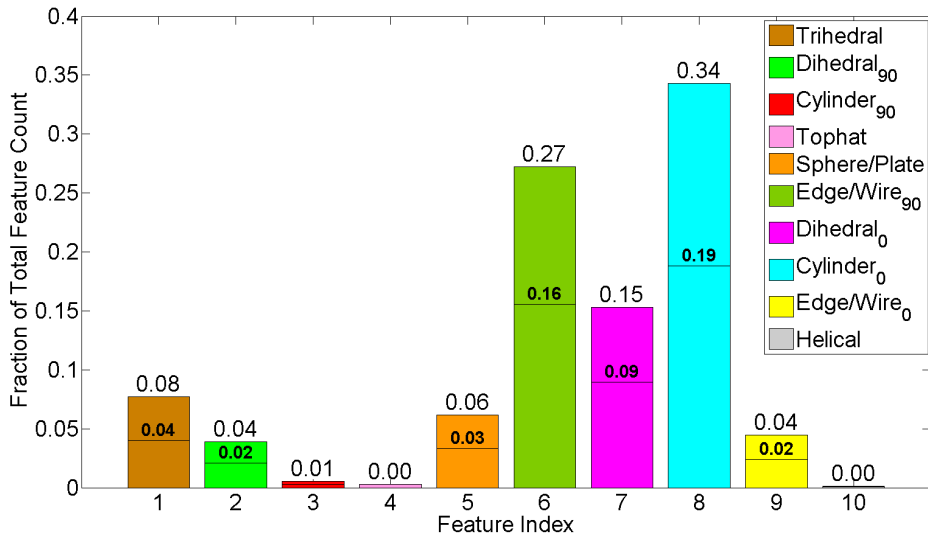


Figure 4.61: Probability of RVM classification error for extracted SPLIT feature vectors as seen throughout elevation angle experiments at 180° azimuth.

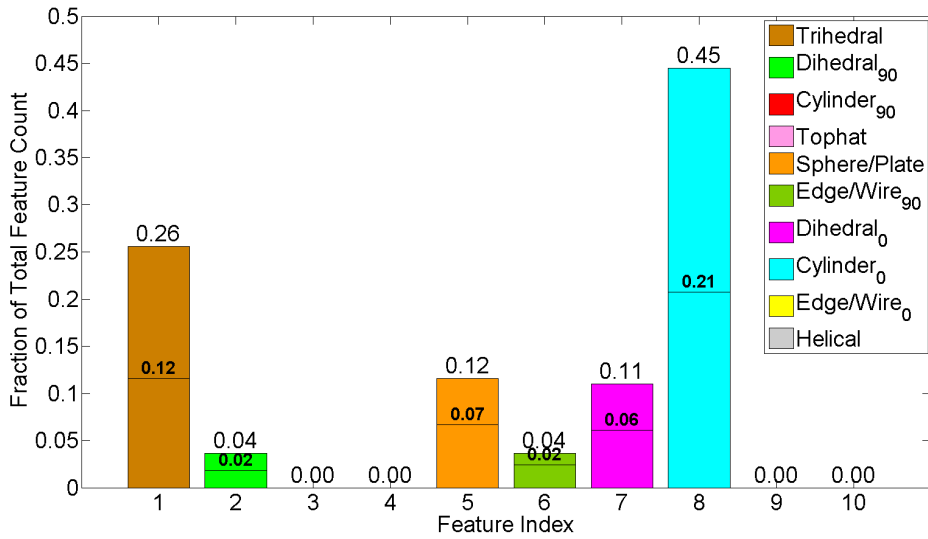


(a) Identified Relevant SPLIT Feature Vectors Only

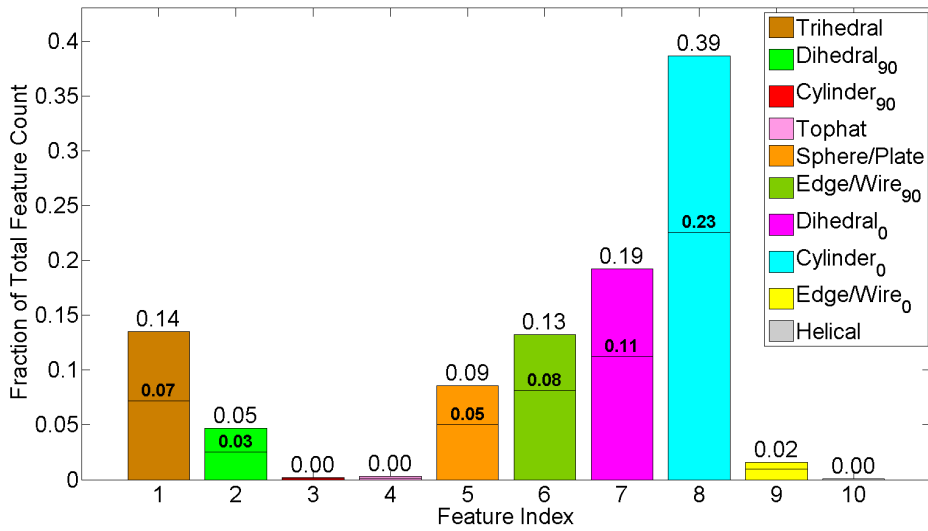


(b) All Extracted SPLIT Feature Vectors

Figure 4.62: Elevation angle experiment histograms for SPLIT FVs (El 30°, Az 180°). The dividing line illustrated on each canonical feature bar separates FVs according to class origin with sedan FVs below the line and SUV FVs above the line. The value over each dividing line indicates the fraction of only sedan FVs, and the value at the top of each feature bar indicates the fraction of all FVs classified as the specified canonical shape.



(a) Identified Relevant SPLIT Feature Vectors Only



(b) All Extracted SPLIT Feature Vectors

Figure 4.63: Elevation angle experiment histograms for SPLIT FVs (El 50°, Az 180°). The dividing line illustrated on each canonical feature bar separates FVs according to class origin with sedan FVs below the line and SUV FVs above the line. The value over each dividing line indicates the fraction of only sedan FVs, and the value at the top of each feature bar indicates the fraction of all FVs classified as the specified canonical shape.

#### 4.2.4 Bandwidth Saliency Experiments for SPLIT Feature Vectors.

The final set of extracted SPLIT feature vector experiments focused on the effects of bandwidth saliency. The same three bandwidths used for extracted HRR feature vector experiments are again utilized for extracted SPLIT feature vectors. Bandwidths include the maximum available CV domes bandwidth of 5.35 GHz, 3 GHz, and the operational AFRL Gotcha bandwidth of 640 MHz [29]. SPLIT bandwidth experiments are conducted at 135° azimuth, 40° elevation, and  $\pm 45^\circ$  aperture size. Mean results for all 24 individual experiments are shown in Table 4.11.

Table 4.11: Mean results for bandwidth experiments 1 – 24 at 135° azimuth, 40° elevation, and  $\pm 45^\circ$  aperture size.

El	# Train/Test	# RVs		% RV		MFW		AFW		$P_e$ %	
		Sedan/SUV	Sedan/SUV	Sedan/SUV	Sedan/SUV	Sedan/SUV	Sedan/SUV	Sedan/SUV	Sedan/SUV		
640MHz	416.8/102.1	6.4/6.5	1.55/1.58	17.23/15.49	7.18/6.52	1.37/21.86					
3.0GHz	1328.8/163.1	8.6/8.6	0.64/0.64	12.28/11.84	4.19/4.01	1.20/8.03					
5.35GHz	1553.1/389.9	10.0/9.6	0.64/0.62	15.90/14.69	5.52/5.02	0.58/7.46					

Training and testing feature vector sets for each bandwidth are illustrated in Figure 4.64. Unsurprisingly, the amount of extracted SPLIT feature vector data increases along with bandwidth. The number of identified RVs for each experiment also increases with bandwidth as shown in Figure 4.65. When comparing the ratio of relevant vectors to training data, however, shown in Figure 4.66, notice that the RVM represents training data classes at 3 GHz bandwidth with nearly the same RV ratio as at 5.35 GHz bandwidth. Due to the reduced computational complexity, this result creates an area of interest in regards to bandwidth saliency at 3 GHz prior to analysis of  $P_e$  results.

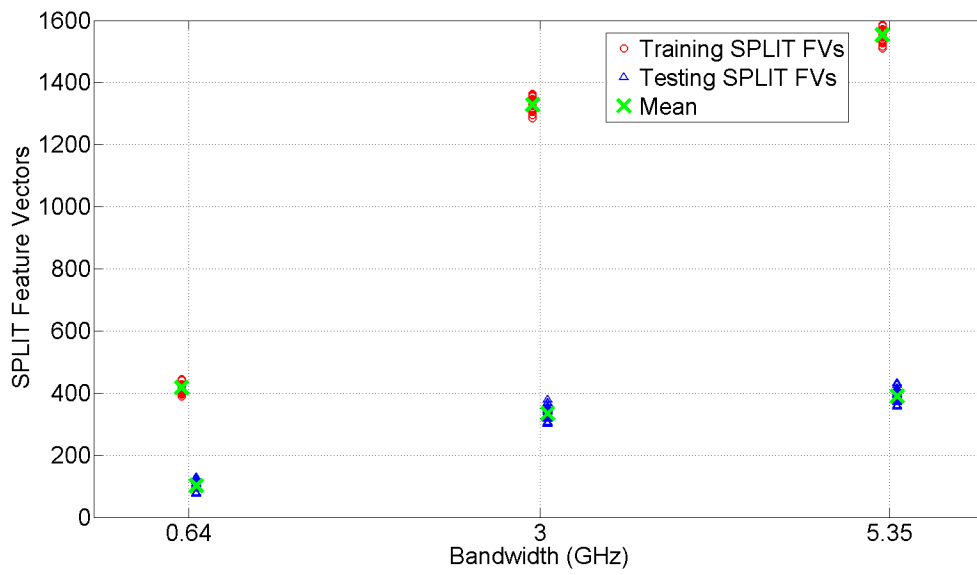


Figure 4.64: Total extracted train and test SPLIT feature vectors for bandwidth experiments at 135° azimuth.

Probability of test classification error for SPLIT feature vectors is shown in Figure 4.67. Classification errors are significantly reduced as bandwidth increases from 640 MHz to 3 GHz, especially for SUV test vehicles, but only slightly reduced from 3 GHz to 5.35 GHz. In regards to bandwidth saliency, 3 GHz is the best choice for accurate test classification performance for SPLIT feature vector experiments. It is clear that additional bandwidth beyond 640 MHz provides worthwhile improvement to test classification results, but it is not clear how much bandwidth may be reduced below 3 GHz to remain salient. Additional testing between 640 MHz and 3 GHz may reveal a more refined desired bandwidth with improved computational performance.

SPLIT feature vector histograms for varying bandwidths are presented in Figure 4.68 for 640 MHz, Figure 4.69 for 3 GHz, and Figure 4.50 for 5.35 GHz. For all extracted SPLIT feature vectors across bandwidths, an increase in vertical edge/wire canonical shape



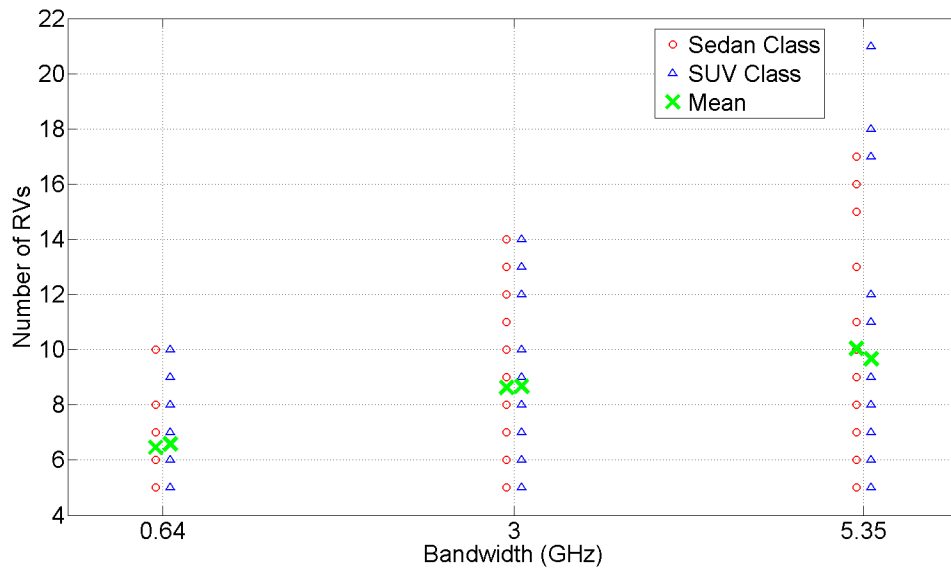


Figure 4.65: Total identified relevant SPLIT feature vectors for bandwidth experiments at 135° azimuth.

classifications is observed due to the non-specular canted azimuth of 135° chosen for the SPLIT bandwidth saliency experiments. As bandwidth is reduced from 5.35 GHz to 640 MHz, feature vector misclassifications may be observed due to the degradation in resolution of the collected SAR CV targets. At 640 MHz in Figure 4.68a, the RVM places the most relevance on vertical edges/wires and almost no classification relevance on horizontal dihedrals, a result that may be misleading toward the goal of improving SAR classification results due to the limited amount of target collection bandwidth. Much more consistent RVM feature classification results may be observed between canonical shape histograms for the two higher bandwidths, shown in Figure 4.69a and Figure 4.50a.

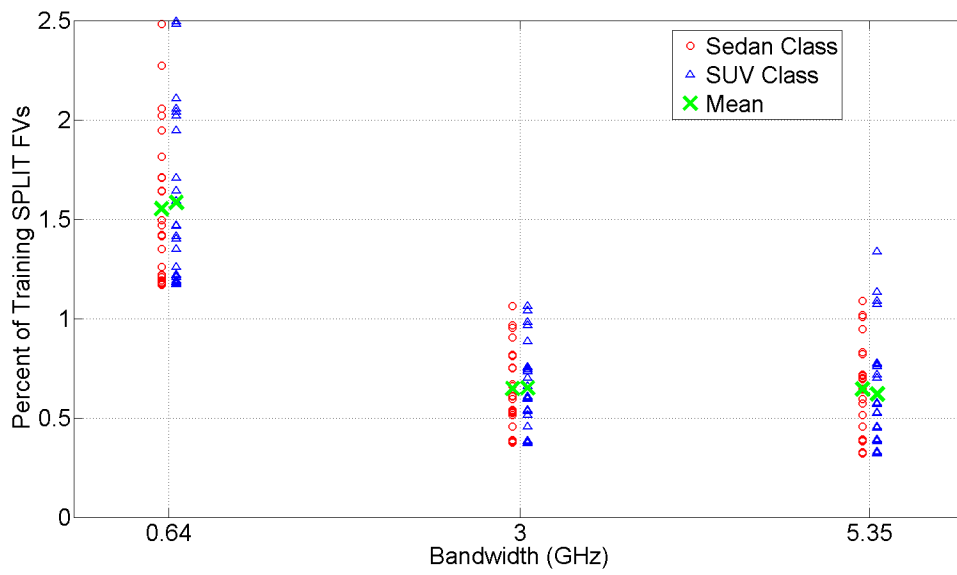


Figure 4.66: Percent of training SPLIT feature vectors deemed relevant for bandwidth experiments at  $135^\circ$  azimuth.

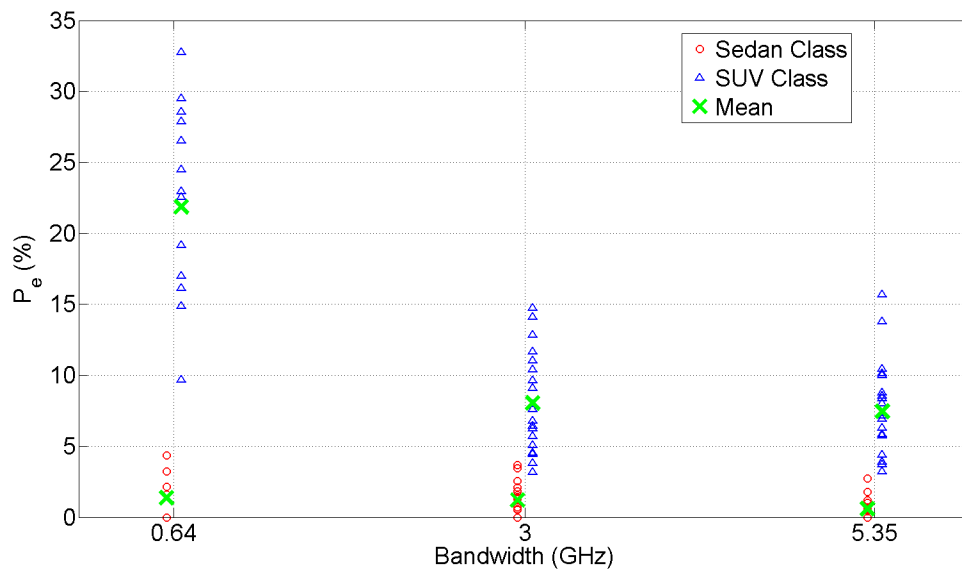
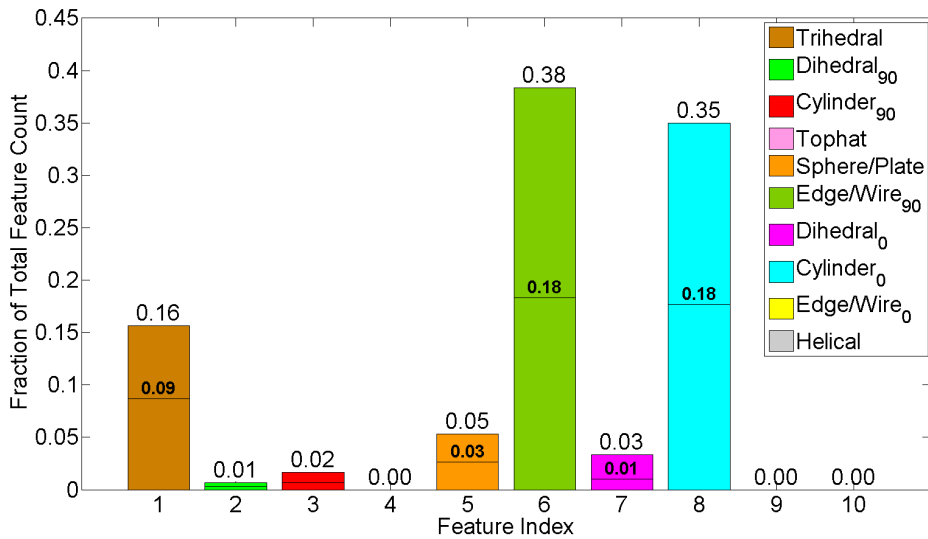
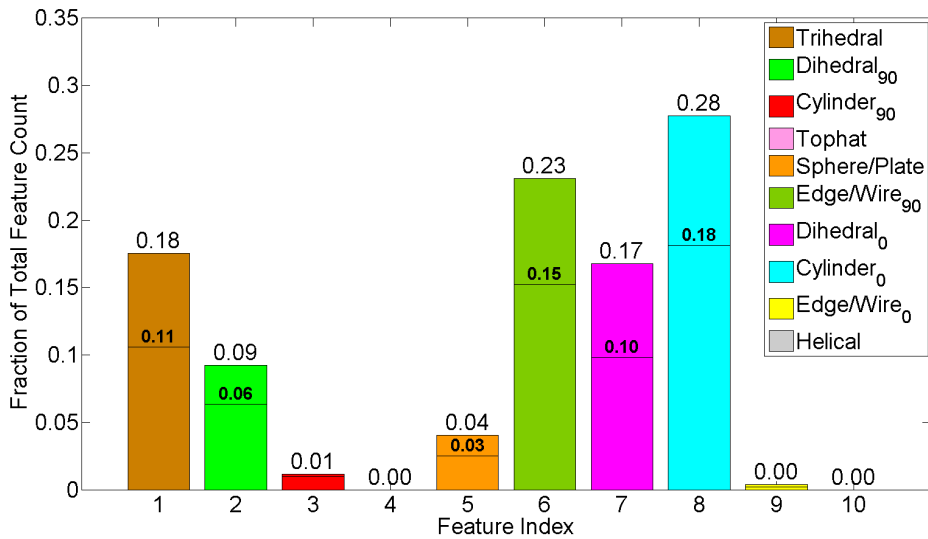


Figure 4.67: Probability of RVM classification error for extracted SPLIT feature vectors as seen throughout bandwidth experiments at  $135^\circ$  azimuth.

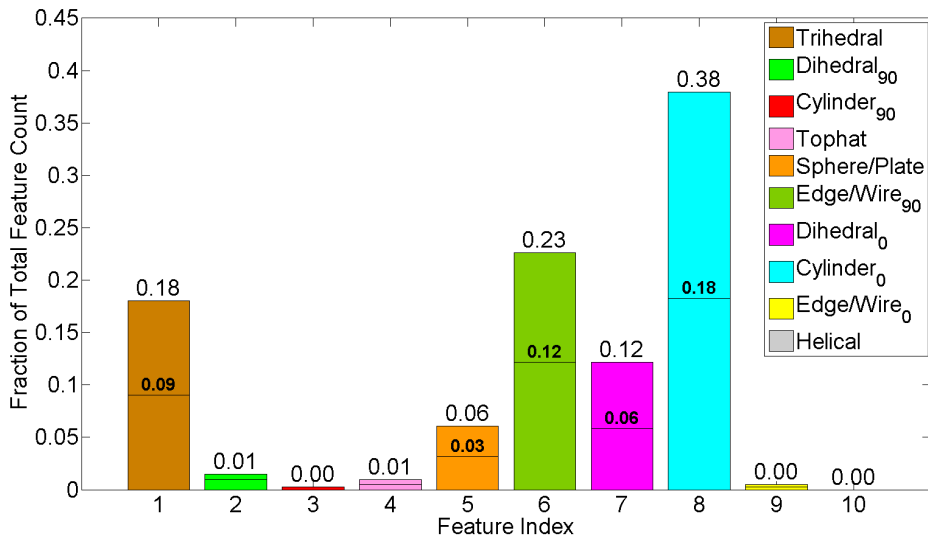


(a) Identified Relevant SPLIT Feature Vectors Only

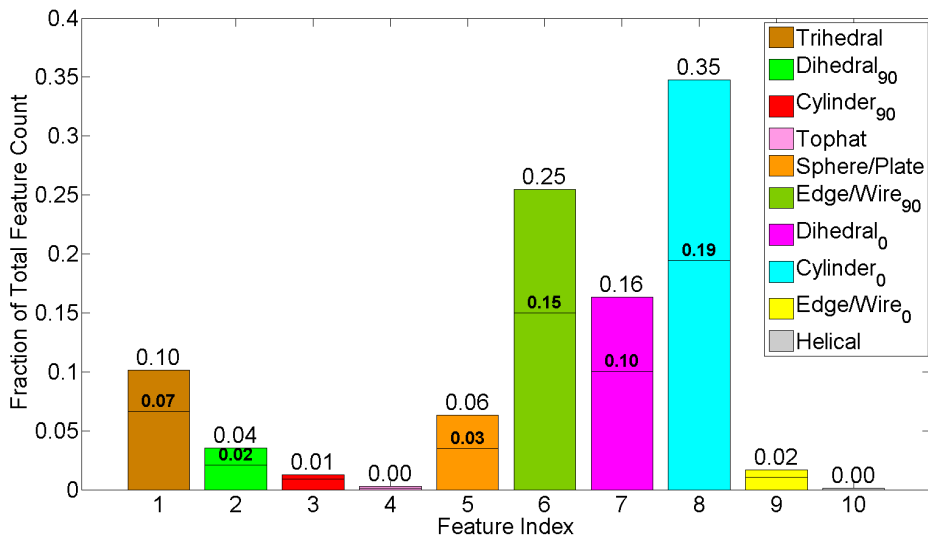


(b) All Extracted SPLIT Feature Vectors

Figure 4.68: Bandwidth experiment histograms for SPLIT FVs (BW 640 MHz, Az 135°). The dividing line illustrated on each canonical feature bar separates FVs according to class origin with sedan FVs below the line and SUV FVs above the line. The value over each dividing line indicates the fraction of only sedan FVs, and the value at the top of each feature bar indicates the fraction of all FVs classified as the specified canonical shape.



(a) Identified Relevant SPLIT Feature Vectors Only



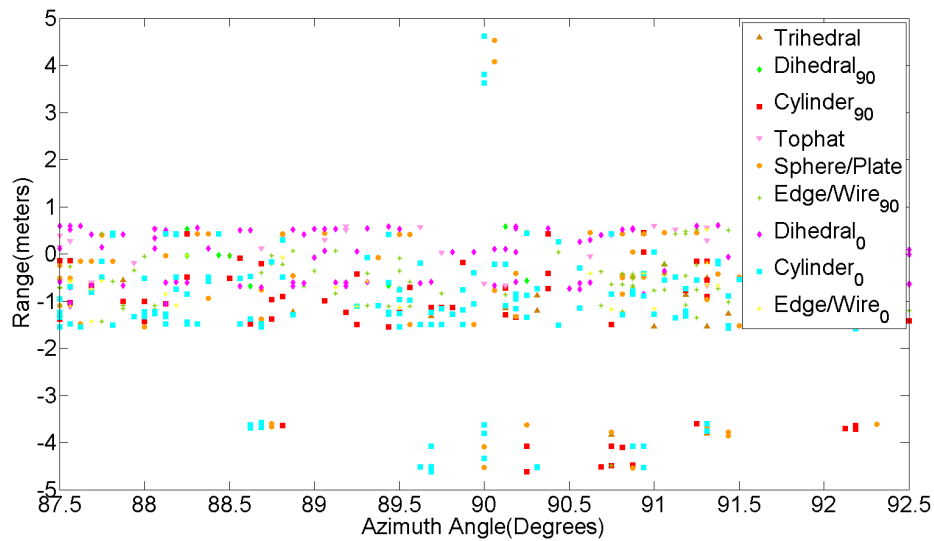
(b) All Extracted SPLIT Feature Vectors

Figure 4.69: Bandwidth experiment histograms for SPLIT FVs (BW 3 GHz, Az 135°). The dividing line illustrated on each canonical feature bar separates FVs according to class origin with sedan FVs below the line and SUV FVs above the line. The value over each dividing line indicates the fraction of only sedan FVs, and the value at the top of each feature bar indicates the fraction of all FVs classified as the specified canonical shape.

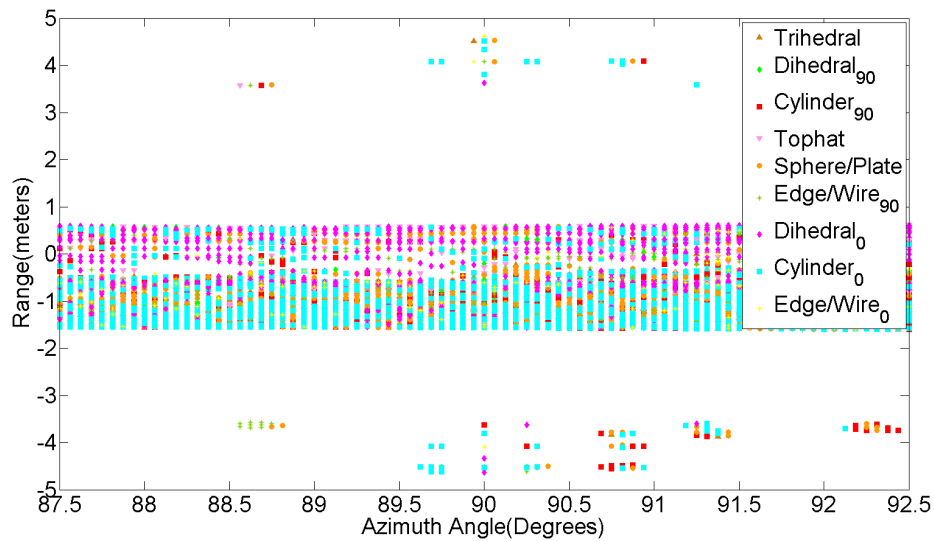
### 4.3 Salient Feature Representation

A potential application of salient feature vector representation may involve examination of feature vector locations in physical target space. Combining the location of identified relevant feature vectors with the classified canonical scatterer type may assist in highlighting the most significant portions of a SAR target contributing to effective ATR. Two examples of this application are provided below. The first example, shown in Figure 4.70, examines extracted HRR feature vectors for sedan class SAR targets at  $90^\circ$  azimuth,  $40^\circ$  elevation,  $\pm 2.5^\circ$  aperture size, and 5.35 GHz bandwidth. All extracted sedan class HRR feature vectors are illustrated in Figure 4.70b, and only the identified relevant HRR feature vectors are highlighted in Figure 4.70a. Observe in both figures that horizontal cylinder features are primarily located at closer ranges, while horizontal dihedral features are appropriately located at more distant ranges due to the increased travel distance of transmitted pulses. In regards to identified relevant HRR feature vectors, no significant groupings or canonical shape patterns are observed in Figure 4.70a. Therefore, improving SAR binary classification using salient features relies primarily on the RVM's relative dependence of canonical target features as illustrated in the histograms from Section 4.1 and Section 4.2.

A second example of salient feature representation is shown in Figure 4.71 for extracted sedan class 2D image SPLIT feature vectors at  $90^\circ$  azimuth,  $40^\circ$  elevation,  $\pm 45^\circ$  aperture size, and 5.35 GHz bandwidth. All extracted SPLIT feature vectors are illustrated in Figure 4.71b with only relevant SPLIT feature vectors in Figure 4.71a. In Figure 4.71b, the general roof line of the combined sedan class vehicles is evident and classified accurately as horizontal cylinder features. Additionally, the side of the sedan vehicles may be identified correctly as horizontal dihedral features. In regards to the RVM identified SPLIT feature vectors illustrated in Figure 4.71a, results are similar to relevant HRR feature vector locations in that no obvious canonical shape patterns or relevant feature vector groupings are evident.



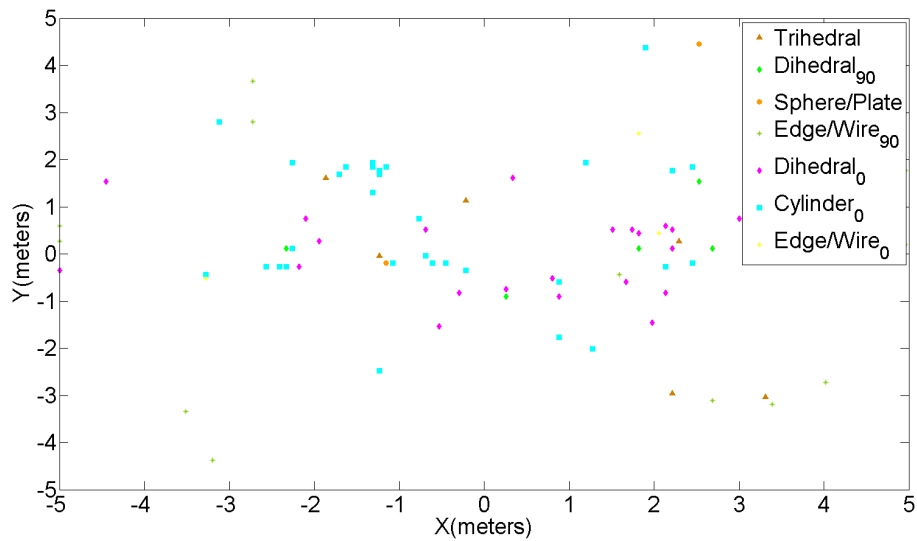
(a) Identified Relevant HRR Feature Vectors Only



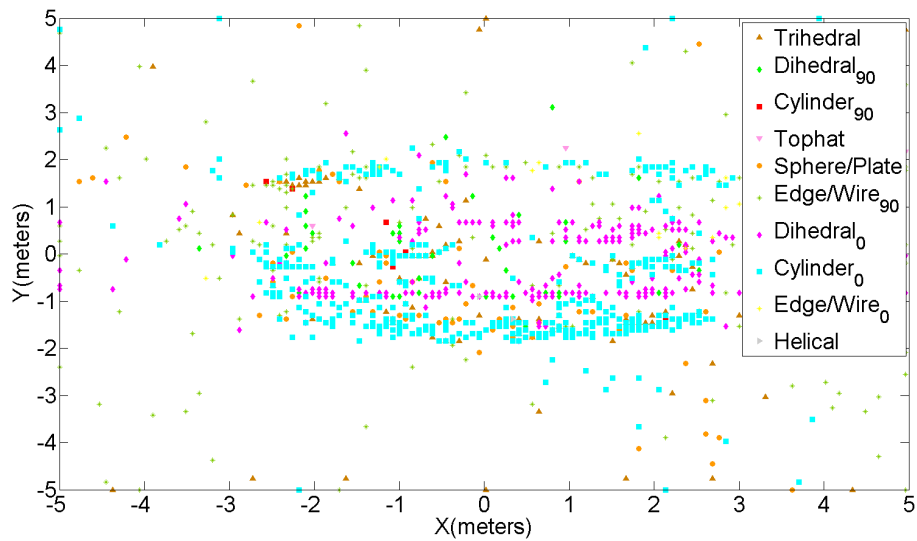
(b) All Extracted HRR Feature Vectors

Figure 4.70: HRR feature vector location representations (azimuth  $90^\circ$ , elevation  $40^\circ$ , aperture size  $\pm 2.5^\circ$ , bandwidth 5.35 GHz)

The locations of identified relevant feature vectors as illustrated in Figure 4.70a and Figure 4.71a assist in improving SAR binary classification performance by translating the



(a) Identified Relevant SPLIT Feature Vectors Only



(b) All Extracted SPLIT Feature Vectors

Figure 4.71: SPLIT feature vector location representations (azimuth  $90^\circ$ , elevation  $40^\circ$ , aperture size  $\pm 45^\circ$ , bandwidth 5.35 GHz)

relevant features to physical target space. Future work, described further in Section 6.2, should in part consider new methods of classification and salient feature representation to

research location patterns and relevant feature vector groupings to narrow the target aspect focus for improving SAR ATR.



## V. Recommendations

The recommendations summarized below are specific only to the experiments conducted, to include SAR data sets used and SAR collection parameter values selected. Therefore, the final recommendations should not be directly applied to any other target class data. One of the primary objectives of our saliency research was to demonstrate a process for determining the appropriate SAR collection parameters and target features contributing most to improving SAR ATR classification decisions. The process is described as characterizing, or investigating, the notion of salient features. A summary of the specific recommendations for both HRR and SPLIT feature vector experiments is presented below, along with recommendations of the most effective extracted feature vector for improving civilian vehicle SAR binary classification performance.

In the exploration of salience, many SAR collection parameter values were adjusted to observe any effects on the feature extraction, feature vector creation, and RVM feature classification processes. Only a select few values were chosen for each test parameter, limiting the specificity of the recommendations shown in Table 5.1. The primary reason for limiting SAR collection parameter values throughout testing is to remind the reader that this thesis is to serve as a guide for investigating and determining saliency in future operational scenarios. Demonstrating the process for defining salient feature sets here should provide a road map to fully characterizing salience in future work. The summary of recommendations is shown in Table 5.1, and a brief discussion of each SAR collection parameter and extracted feature vector is included in Section 5.1 through Section 5.5.

### 5.1 Azimuth Angle Recommendation

Recommendations for both types of extracted feature vectors agreed in terms of a desired collection parameter recommendation for azimuth angle experiments. While both

Table 5.1: Summary of Parameter Recommendations

Parameter	HRR Feature Vectors	SPLIT Feature Vectors
Azimuth Angle	112.5°	90° – 135°
Aperture Size	5°	60°
Elevation Angle	30°	30°
Bandwidth	640MHz – 3GHz	640MHz – 3GHz

sets of extracted feature vector experiments highlighted the side and rear aspects of the vehicles, specifically from 90° to 135° as the most significant aspects to effective vehicle classification, the additional azimuths tested within the HRR experiments narrowed the recommendation to 112.5°. Additional SPLIT testing may determine whether 112.5° is the most effective azimuth for SPLIT feature vectors as well, but the additional testing is not necessary for the objectives of our saliency research. Demonstrating the process of characterizing saliency so that it may be applied to other SAR phase history data sets has been met with confidence for the azimuth experimentation parameter due to the consistency of results for both types of extracted feature vectors. A general recommendation for this particular example will hopefully lead to the process being utilized for determination of a precise recommendation for use in an operational scenario.

## 5.2 Aperture Size Recommendation

Following analysis of aperture size experimental results, it appears that aperture size does not have a significant effect on SAR classification performance. In both types of feature vector experiments, all three aperture sizes demonstrated similar  $P_e$  results. Considering other factors as well resulted in the smallest aperture size of 60°(±30°) being recommended for extracted SPLIT feature vector classification. Although HRR feature vector test results were consistent with SPLIT, the large increase in extracted HRR feature vectors over narrow apertures led to a 5° aperture size recommendation.

Because the selective nature of the SPLIT algorithm eliminates many pixels prior to feature extraction, there are significantly less extracted SPLIT feature vectors than extracted HRR feature vectors over the same aperture. Therefore, a direct comparison between the two recommendations is not valid, but instead each recommendation should be considered individually depending on the type of feature vector being extracted for application of the salient feature identification process in future work.

### **5.3 Elevation Angle Recommendation**

Elevation angle saliency experiments produced a clear and consistent recommendation for both extracted feature vector types. Applying the salient feature identification process to the AFRL CV data domes [15] demonstrated that improved RVM classification performance may be achieved at the lowest elevation angle of 30°. For effective separation of sedan and SUV class vehicles, the most uniquely identifying physical target features are found on the bodies of the vehicles below the roof line, a surface area seen best with SAR data collection at lower elevation.

### **5.4 Bandwidth Recommendation**

Bandwidth saliency recommendations were somewhat consistent for both extracted feature vector types. HRR feature vector  $P_e$  results demonstrated similar classification error values across all three bandwidths. After observing salient canonical shape histograms, however, it became more clear that reducing bandwidth causes target feature misclassifications due to degraded resolution. The investigation ultimately led to a recommendation of greater than 640 MHz, or as much bandwidth as available resources will allow between 640 MHz and 3 GHz. SPLIT feature vectors told a somewhat different story.  $P_e$  results were consistent between 3 GHz and 5.35 GHz but significantly degraded at 640 MHz. Considering all other bandwidth experiment results, it became clear that additional bandwidth beyond 640 MHz provides worthwhile improvement to classification

performance, but it is not clear how much bandwidth may be reduced below 3 GHz to remain salient. Additional SPLIT feature vector testing between 640 MHz and 3 GHz may reveal a more refined desired bandwidth with improved computational performance.

## 5.5 Feature Vector Recommendation

Each type of extracted feature vector utilized throughout the saliency investigation provided its own benefits to improving classification performance. HRR feature vectors provided a more thorough view of the SAR targets, using all collected phase history data to fully investigate a specific region of the targets. In addition, the larger, often cumbersome, HRR feature vector sets are preferred by the RVM classifier as they allow more training data to be considered for effective class separation and creation of the hyperplane decision boundary. Extracted SPLIT feature vectors provide benefits as well. While SPLIT extracts less feature vectors than the HRR method over the same SAR collection parameters, the feature vectors which are extracted are more accurate representations of canonical target features due to thresholding parameters implemented throughout the extraction process. The selective nature of SPLIT feature extraction leads to reduced  $P_e$  results throughout RVM tests. Also, the reduction in extracted SPLIT feature vectors allows larger apertures to be collected for RVM classification, providing class comparison of many different target aspects with reduced computational complexity.

In short, the recommended type of extracted feature vector for improving SAR classification performance depends on the goals and resources available for the specific task at hand. For saliency characterization of SAR targets with large aperture phase history data available, extracting SPLIT feature vectors may be the best choice for both improved classification performance and reduced resource requirements. If real-world threat restrictions limit the amount of SAR target aspect coverage available for collection, the more comprehensive method of extracting HRR feature vectors may be the appropriate choice.

## **VI. Conclusions and Future Work**

### **6.1 Conclusions**

The overarching objective of our research was to investigate the notion of saliency for improving SAR binary classification performance for application to, and improvement of, SAR ATR. With that objective in mind, several goals were proposed in Section 1.3 to guide the saliency exploration. To satisfy goal #1, a methodology was developed in Section 3.1 for characterizing feature salience by extracting potentially identifying features from SAR phase history data to form feature vectors for kernel-based classification. The Bayesian-based RVM classifier [13] was selected to compare the two classes of extracted feature vectors for identification of the most relevant feature vectors contributing to classification decisions. Goal #2 was achieved by first designing a robust set of experiments in Section 3.2 to compare the sedan and SUV class vehicles of AFRL's CV data domes [15]. Then, in Chapter 4, experiments were executed to characterize saliency by uncovering the most impactful feature vectors and SAR collection parameters for improving classification performance between sedan and SUV class civilian vehicles. Finally, initial goals #3 and #4 were met through the recommendations summarized in Chapter 5 based on the experimental results and analysis detailed in Chapter 4.

### **6.2 Future Work**

The salient feature identification and analysis research provides a foundation for future work in saliency characterization for improving SAR binary classification performance. Several potential research topics are presented based on the initial exploratory results observed in the first attempt at fully investigating class saliency of the AFRL CV data domes SAR phase history data set [15].

- Extend saliency research to other SAR phase history data sets to compare the classification performance for various target classes. Additionally, demonstrate the saliency identification algorithm on real-world SAR data collections such as AFRL's Gotcha data set [29] to investigate the challenges introduced by resource limitations and noisy target collection environments.
- Explore the effects of various training data sets on RVM classification accuracy. For example, removing the Tacoma from the SUV class in our research would have improved results across SUV tests. Developing the optimal RVM class training process will lead to more accurate classification results in regards to identifying salient features.
- Extract additional features for creation of new feature vectors beyond the HRR and SPLIT feature vectors implemented in our research. Determine the most effective extracted feature vector set for improving SAR binary classification performance.
- Conduct saliency experiments using a variety of classification techniques beyond the kernel-based RVM to resolve the most operative ATR classification algorithm.
- Extend the current canonical shape classification of relevant feature vectors by developing new methods of salient feature representation in physical target space.
- Refine the nature of saliency for improving SAR binary classification performance by introducing new methods to contribute to the current SAR ATR framework.

## Bibliography

- [1] M. Pesaresi and J. A. Benediktsson, "A new approach for the morphological segmentation of high-resolution satellite imagery," *IEEE Transactions on Geoscience and Remote Sensing*, vol. 39, no. 2, pp. 309–320, 2001.
- [2] C. V. Jakowatz, D. E. Wahl, P. H. Eichel, D. C. Ghiglia, and P. A. Thompson, *Spotlight-mode synthetic aperture radar: a signal processing approach*, vol. 101. Kluwer Academic Publishers Norwell, MA, 1996.
- [3] D. C. Munson Jr, J. D. O'Brien, and W. K. Jenkins, "A tomographic formulation of spotlight-mode synthetic aperture radar," *Proceedings of the IEEE*, vol. 71, no. 8, pp. 917–925, 1983.
- [4] M. R. McClure and L. Carin, "Matching pursuits with a wave-based dictionary," *IEEE Transactions on Signal Processing*, vol. 45, no. 12, pp. 2912–2927, 1997.
- [5] K. R. Varshney, M. Çetin, J. W. Fisher, and A. S. Willsky, "Sparse representation in structured dictionaries with application to synthetic aperture radar," *IEEE Transactions on Signal Processing*, vol. 56, no. 8, pp. 3548–3561, 2008.
- [6] B. G. Hammond and J. A. Jackson, "SAR canonical feature extraction using molecule dictionaries," in *IEEE Radar Conference*, pp. 1–6, IEEE, 2013.
- [7] J. A. Jackson, *Three-dimensional feature models for synthetic aperture radar and experiments in feature extraction*. PhD thesis, The Ohio State University, Columbus, OH, 2009.
- [8] D. F. Fuller, *Phase history decomposition for efficient scatterer classification in SAR imagery*. PhD thesis, Air Force Institute of Technology, 2011.
- [9] M. A. Saville, J. A. Jackson, and D. F. Fuller, "Rethinking vehicle classification with wide-angle polarimetric SAR," *IEEE Aerospace and Electronic Systems Magazine*, vol. 29, pp. 41–49, January 2014.
- [10] C. Chen, J. S. DaPonte, and M. D. Fox, "Fractal feature analysis and classification in medical imaging," *IEEE Transactions on Medical Imaging*, vol. 8, no. 2, pp. 133–142, 1989.
- [11] C. Bahlmann, B. Haasdonk, and H. Burkhardt, "Online handwriting recognition with support vector machines—a kernel approach," in *Eighth International Workshop on Frontiers in Handwriting Recognition*, pp. 49–54, IEEE, 2002.
- [12] C. Cortes and V. Vapnik, "Support-vector networks," *Machine learning*, vol. 20, no. 3, pp. 273–297, 1995.

- [13] M. E. Tipping, “Sparse bayesian learning and the relevance vector machine,” *Journal of Machine Learning Research*, vol. 1, pp. 211–244, September 2001.
- [14] P. Runkle, J. Woodworth, and L. Bradway, “Kernel methods for saliency cueing: Application to synthetic database optimization,” pp. 1–38, May 2008.
- [15] K. E. Dungan, C. Austin, J. Nehrbass, and L. C. Potter, “Civilian vehicle radar data domes,” in *SPIE Defense, Security, and Sensing*.
- [16] E. Krogager, “New decomposition of the radar target scattering matrix,” *Electronics Letters*, vol. 26, no. 18, pp. 1525–1527, 1990.
- [17] Y. Hua and T. K. Sarkar, “Generalized pencil-of-function method for extracting poles of an EM system from its transient response,” *IEEE Transactions on Antennas and Propagation*, vol. 37, no. 2, pp. 229–234, 1989.
- [18] Y. Hua and T. K. Sarkar, “Matrix pencil method for estimating parameters of exponentially damped/undamped sinusoids in noise,” *IEEE Transactions on Acoustics, Speech and Signal Processing*, vol. 38, no. 5, pp. 814–824, 1990.
- [19] N. Cristianini and J. Shawe-Taylor, *An introduction to support vector machines and other kernel-based learning methods*. Cambridge university press, 2000.
- [20] T. Fletcher, “Relevance vector machines explained,” *Practice*, pp. 1–9, 2008.
- [21] T. Hastie, R. Tibshirani, and J. Friedman, *The elements of statistical learning*, vol. 1. Springer New York, 2001.
- [22] L. C. Potter and R. L. Moses, “Attributed scattering centers for SAR ATR,” *IEEE Transactions on Image processing*, vol. 6, no. 1, pp. 79–91, 1997.
- [23] E. Krogager, “Advances of techniques for utilizing polarimetric features of radar targets,” *NATO RTO SET Symposium on Target ID and Recognition Using RF Systems*, vol. 080-40, pp. 1–8, 2004.
- [24] K. Levenberg, “A method for the solution of certain problems in least squares,” *Quarterly of applied mathematics*, vol. 2, pp. 164–168, 1944.
- [25] T. Cover and P. Hart, “Nearest neighbor pattern classification,” *IEEE Transactions on Information Theory*, vol. 13, no. 1, pp. 21–27, 1967.
- [26] I. Jolliffe, *Principal component analysis*. Wiley Online Library, 2005.
- [27] T. Fletcher, “Support vector machines explained,” *Practice*, pp. 1–19, 2009.
- [28] K. Muller, S. Mika, G. Ratsch, K. Tsuda, and B. Scholkopf, “An introduction to kernel-based learning algorithms,” *IEEE Transactions on Neural Networks*, vol. 12, no. 2, pp. 181–201, 2001.



- [29] SDMS, “Air Force Research Lab Sensor Data Management System Gotcha volumetric SAR data set overview.” <https://www.sdms.afrl.af.mil/index.php?collection=gotcha>, January 2014.

# REPORT DOCUMENTATION PAGE

*Form Approved*  
OMB No. 0704-0188

The public reporting burden for this collection of information is estimated to average 1 hour per response, including the time for reviewing instructions, searching existing data sources, gathering and maintaining the data needed, and completing and reviewing the collection of information. Send comments regarding this burden estimate or any other aspect of this collection of information, including suggestions for reducing this burden to Department of Defense, Washington Headquarters Services, Directorate for Information Operations and Reports (0704-0188), 1215 Jefferson Davis Highway, Suite 1204, Arlington, VA 22202-4302. Respondents should be aware that notwithstanding any other provision of law, no person shall be subject to any penalty for failing to comply with a collection of information if it does not display a currently valid OMB control number. **PLEASE DO NOT RETURN YOUR FORM TO THE ABOVE ADDRESS.**

<b>1. REPORT DATE</b> (DD-MM-YYYY) 27-03-2014		<b>2. REPORT TYPE</b> Master's Thesis		<b>3. DATES COVERED</b> (From — To) Oct 2012–Mar 2014	
<b>4. TITLE AND SUBTITLE</b>  Salient Feature Identification and Analysis using Kernel-Based Classification Techniques for Synthetic Aperture Radar Automatic Target Recognition				<b>5a. CONTRACT NUMBER</b>	
				<b>5b. GRANT NUMBER</b>	
				<b>5c. PROGRAM ELEMENT NUMBER</b>	
				<b>5d. PROJECT NUMBER</b>  LRIR12RY19COR	
				<b>5e. TASK NUMBER</b>	
				<b>5f. WORK UNIT NUMBER</b>	
<b>6. AUTHOR(S)</b>  Flynn, Matthew S., Captain, USAF					
<b>7. PERFORMING ORGANIZATION NAME(S) AND ADDRESS(ES)</b> Air Force Institute of Technology Graduate School of Engineering and Management (AFIT/EN) 2950 Hobson Way WPAFB, OH 45433-7765				<b>8. PERFORMING ORGANIZATION REPORT NUMBER</b>  AFIT-ENG-14-M-30	
<b>9. SPONSORING / MONITORING AGENCY NAME(S) AND ADDRESS(ES)</b> Air Force Office of Scientific Research Dr. Michael Kendra 875 N. Randolph St., Suite 325 Arlington, VA 22203 michael.kendra@afosr.af.mil				<b>10. SPONSOR/MONITOR'S ACRONYM(S)</b>  AFOSR/RTA	
				<b>11. SPONSOR/MONITOR'S REPORT NUMBER(S)</b>	
<b>12. DISTRIBUTION / AVAILABILITY STATEMENT</b> Distribution Statement A: Approved for Public Release; Distribution Unlimited					
<b>13. SUPPLEMENTARY NOTES</b> This material is declared a work of the U.S. Government and is not subject to copyright protection in the United States.					
<b>14. ABSTRACT</b> An investigation into feature saliency for application to synthetic aperture radar (SAR) automatic target recognition (ATR) is presented. Specifically, research is focused on improving the SAR binary classification performance aspect of ATR, or the ability to accurately determine the class of a SAR target. The key to improving ATR classification performance lies in characterizing the salient target features. Salient features may be loosely defined as the most consistently impactful parts of a SAR target contributing to effective SAR ATR classification. To better understand the notion of saliency, an investigation is conducted into the nature of saliency as applied to Air Force Research Lab's (AFRL) civilian vehicle (CV) data domes simulated phase history data set. After separating vehicles into two SAR data classes, sedan and SUV, frequency and polarization features are extracted from SAR data and formed into either 1D high range resolution (HRR) or 2D spectrum parted linked image test (SPLIT) feature vectors. A series of experiments comparing vehicle classes are designed and conducted to focus specifically on the saliency effects of various SAR collection parameters including azimuth angle, aperture size, elevation angle, and bandwidth. The popular kernel-based Bayesian Relevance Vector Machine (RVM) classifier is utilized for sparse identification of relevant vectors contributing most to the creation of a hyperplane decision boundary. Analysis of experimental results ultimately leads to recommendations of the salient feature vectors and SAR collection parameters which provide the most potential impact to improving vehicle classification. Demonstrating the proposed saliency characterization algorithm with simulated civilian vehicle data provides a road map for salient feature identification and analysis of other SAR data classes in future operational scenarios. ATR practitioners may use saliency results to focus more attention on the identified salient features of a target class, improving efficiency and effectiveness of SAR ATR.					
<b>15. SUBJECT TERMS</b> SAR, ATR, HRR, SPLIT, RVM, salient feature identification, feature vector, extraction, classification					
<b>16. SECURITY CLASSIFICATION OF:</b>			<b>17. LIMITATION OF ABSTRACT</b>	<b>18. NUMBER OF PAGES</b>	<b>19a. NAME OF RESPONSIBLE PERSON</b> Dr. Julie A. Jackson (ENG)
a. REPORT	b. ABSTRACT	c. THIS PAGE			<b>19b. TELEPHONE NUMBER</b> (include area code) (937) 255-3636 x4678 Julie.Jackson@afit.edu
U	U	U	UU	153	